

POLITECNICO DI TORINO

Department of Mechanical and Aerospace Engineering

**Master Degree in Mechanical Engineering**

Thesis of Master Degree

**Dynamics of a mistuned bladed disk and  
friction damping analysis**



**Supervisors :**

prof. Christian Maria Furrone

prof. Daniele Botto

**Candidate**

Enrico Pipitone

April 2018



## Acknowledgements

I would like to express my gratitude to my supervisors, Prof. Christian Maria Furrone and Prof. Daniele Botto, for the interest and the cooperation showed during these months and for giving me the great opportunity to explore such a exciting subject. I would particularly like to thank my family. My parents, for the efforts to support my studies with dedication and love. My brothers, for the helpful presence in hard times. My grandparents for their warmth and wisdom. My aunts Margherita and Valeria for the friendship. Finally, I want to thank my friends Davide, Nino, Federica, Stefano, Carlo and my university colleague and “brother-in-arms” Giuseppe for being there throughout my university career.



# Contents

- Introduction ..... 7
- Chapter 1 : Dynamics of a Bladed Disk..... 9
  - 1.1 Nodal diameters of the disk..... 9
  - 1.2 Structure modeling and modal analysis ..... 10
  - 1.3 Cyclic symmetry analysis..... 15
- Chapter 2 : Forced Response..... 19
  - 2.1 Forced response of the bladed disk ..... 19
  - 2.2 Forced response by means of cyclic symmetry ..... 23
- Chapter 3 : Mistuning analysis ..... 25
  - 3.1 Brief history of mistuning studies ..... 25
  - 3.2 Nature of the mistuning phenomenon ..... 26
  - 3.3 Effects of mistuning on the forced response ..... 31
  - 3.4 Mistuning identification ..... 42
    - 3.4.1 Modeling of the bladed disk with joints incorporation..... 42
    - 3.4.2 FRF Decoupling Method ..... 45
    - 3.4.3 Use of FRF Decoupling for mistuning identification..... 48
- Chapter 4 : Friction-damped response analysis ..... 54
  - 4.1 Bladed disk with blade-to-ground friction dampers ..... 54
  - 4.2 Bladed disk with joint friction ..... 63
  - 4.3 Bladed disk with blade-to-blade friction..... 72
- Conclusions ..... 82
- Appendix ..... 83
  - A-1 Modeling of the bladed disk ..... 83
  - A-2 Modeling of a disk sector..... 85
  - A-3 Modeling of a sector for blade-to blade friction analysis ..... 87
  - A-4 Modeling of the bladed disk with joints incorporation..... 91
- References ..... 93



# Introduction

The thesis is devoted to the study of the dynamics of structures such as turbine bladed disks for aeronautic applications. The subject will be explored through the chapters in order to understand what are the dynamic characteristics of such structures and how they interact with the outer environment and the various excitation sources, so to evidence the critical interaction conditions that can lead to instability problems and failure. As a matter of fact, the blades, which are the most critical components of the turbine system, can vibrate in resonance conditions and this can reduce the fatigue life of the component. Then, a preliminary study of the dynamics is of primary importance since the investigation of fractures and components life in general is very difficult to be conducted once the turbine is installed for the application. The vibrations of bladed disks are strongly influenced by the working conditions of the system, such as rotational speed of the turbine rotor and nature of the excitation sources. Another issue which can remarkably affect the vibrations of the blades is represented by the problem of the *mistuning*. This term is commonly used in literature to indicate the lack of symmetry of the bladed disk due to the uncertainty on the mechanical properties of the disk structure. The mistuning phenomenon and its effect on the vibrations are widely explored in the thesis and a method of mistuning identification is provided in order to forecast the behavior of the bladed disk during the application. The final part of the thesis is dedicated to the effect of friction interactions with special devices or between the parts of the bladed disk itself, which are often purposely designed in order to add damping to the structure. This leads the study of the dynamics in the non-linear field. For this reason other analytical methods are used to analyze the vibrations as well as to evaluate the benefits in terms of damping of the vibration with respect to the situation in which only the material damping is considered. The aforementioned topics are organized in the chapters of this thesis in order to maintain continuity among them: In Chapter 1 the dynamic characteristics of a structure such as the bladed disk are explored defining the important concept of *nodal diameter* which has a primary role in the disk dynamics. Then, a modal analysis is conducted on the structure which is modeled by adopting a lumped parameters approach, so to evidence the main properties of the mode shapes of such systems. A parallel study is also performed on the system by exploiting the property of *cyclic symmetry* of the bladed disk. This important property helps the designer in the study of the whole structure by reducing a lot the complexity of the model. Chapter 2 is dedicated to study of the forced response of the structure. This brings to the definition of the external excitation force and the *Engine Order* (EO). The forced response is computed both for the full system model and by exploiting the cyclic symmetry of the disk. In Chapter 3 the *mistuning* phenomenon is studied. In particular, what is the nature of *mistuning* and what it depends on, how it affects the forced response of the blades and which are the main issues that occur. In the second part of this chapter a method of *mistuning* identification is proposed in order to quantify the amount of *mistuning* starting from the Frequency Response Function (FRF) of the tested structure. The identification makes use of the FRF Decoupling Method in order to investigate the mechanical properties of the joints, which connect the blades to the disk, representing one of the major cause of *mistuning* because of the uncertainty linked to their dynamic behavior. Chapter 4 analyzes the forced response of the bladed disk in presence of sliding friction between parts of the disk itself or with external devices. As it was mentioned before, friction behaves as a damping agent, so it contributes to reduce the response amplitude of the blades in resonance condition. In more detail, three different situations are analyzed. In the first case a *blade-to-ground damper*, which acts between the blade and an external fixed reference is incorporated in the model, in order to

simulate the action of some particular devices that can be provided in the design of the bladed disk. A second case assumes to have sliding friction in the joints connecting the blades to the disk. The last case, more restrictive than the previous cases, considers a sliding friction between adjacent blades, if the constructional design of the blades allows such a situation, as for shrouded blades.

# Chapter 1

## Dynamics of a Bladed Disk

### 1.1 Nodal diameter of a circular structure

A *bladed disk* is a turbo-machine component which consists of a disk and the blades attached onto the disk body. These structures are characterized by a cyclic symmetry. As a consequence, they show particular dynamic characteristics which play a primary role in the vibrations of such components. These characteristics can be studied, as a first approach, by assuming the bladed disk to represent a circular membrane. Of course, this is a reductive hypothesis because a bladed disk is a tridimensional structure, so it shows a dynamic behavior that is much more complex than the one showed by a membrane. However, this assumption is enough to understand the dynamic behavior from the general point of view and it represents a good starting point for the discussion.

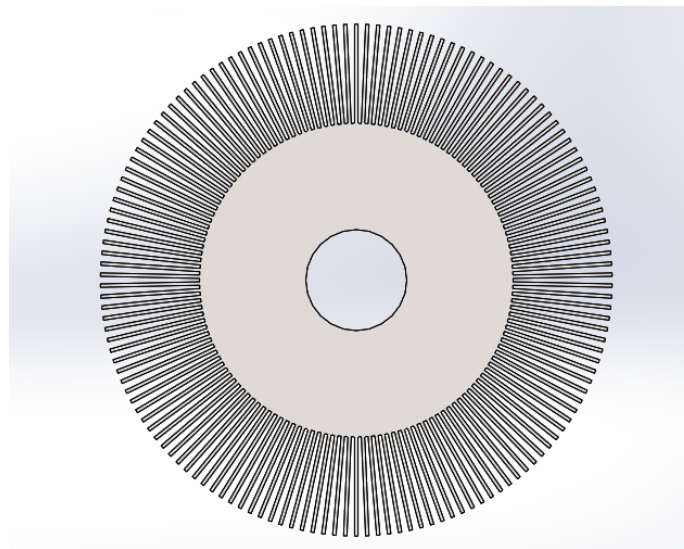


Figure 1.1. Representation of a bladed disk

The main feature of interest is represented by the so called *nodal diameter*. The nodal diameter is a locus of points called *nodes*, which doesn't move at a specific frequency. There are more than one nodal diameters and each of them corresponds to a particular value of frequency. The number of nodal diameters is strictly connected to the number of sectors in which a bladed disk can be subdivided in such a way to satisfy the property a cyclic symmetry.

For this reason a sector is identified with a blade and a correspondent slice of disk body, where the blade is attached, so to form a closed circular structure made of substructures identical with each other (figure 1.2). In this way the number of sectors  $N$  coincides with the number of blades.

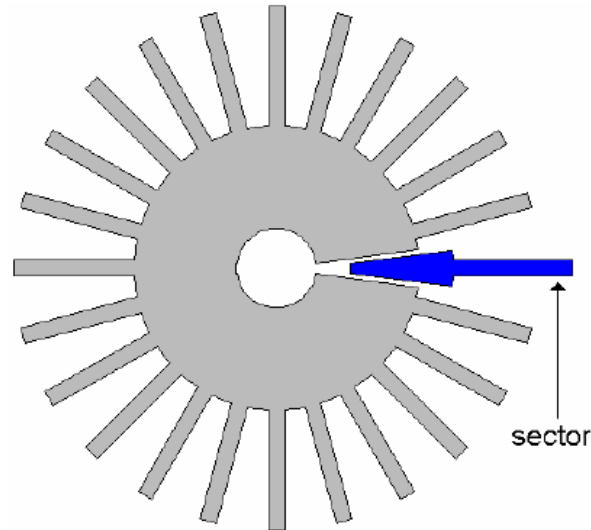


Figure 1.2. Representation of a disk sector

Once the number of sectors has been defined, a relation between the number of nodal diameters,  $n$ , and the number of sectors,  $N$ , can be defined.

- $0 \leq n \leq \frac{N}{2}$  if  $N$  is even.
- $0 \leq n \leq \frac{N-1}{2}$  if  $N$  is odd.

The nodal diameters have particular implications on the mode shapes. Before going deeply in detail of the modal analysis, a modeling method has to be adopted.

## 1.2 Modeling of the structure

The method used for the dynamic study of the bladed disk follows a lumped parameters approach. The model is constituted by two equivalent masses  $m_d$  and  $m_b$ , respectively the mass of disk sector and the mass of the blade, and three stiffness elements  $k_c$ ,  $k_d$  and  $k_b$ , where the first two stiffness elements are connected to the disk and the last one is connected to the blade. The lumped parameters are disposed in such a way to build an equivalent model of the structure (Figure 1.3). Since the number of sectors is  $N$ , as a consequence the number of degrees of freedom of the lumped parameters model is  $2N$ . Being  $\{x\}$  the physical displacement coordinates vector of dimension  $2N \times 1$ ,  $[M]$  and  $[K]$  respectively the mass matrix and stiffness matrix of dimension  $2N \times 2N$  (they are derived in Appendix 1), the equations of motion can be written in the matrix form (1.1).

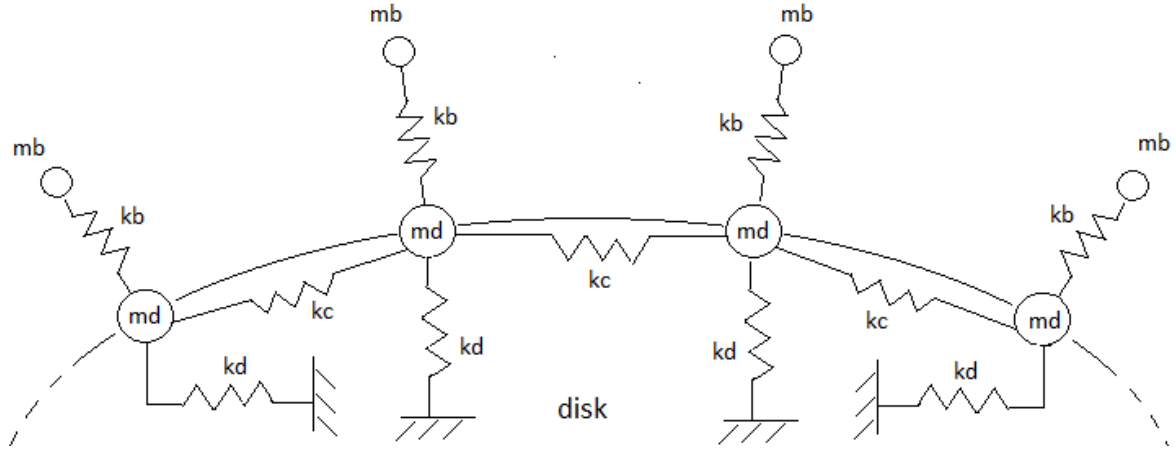


Figure 1.3. Lumped parameters model

$$[M]\{\ddot{x}\} + [K]\{x\} = \{0\} \quad (1.1a)$$

$$\{x\} = x_i \quad (1.1b)$$

where

- $i \in [1, N]$  , degrees of freedom of the disk.
- $i \in [N + 1, 2N]$  , degrees of freedom of the blades.

No external forces are applied at this stage in order to perform the modal analysis of the system. It is well known that this set of linear time-invariant differential equations admits solutions of the type (1.2), where  $\{X_0\}$  is the amplitude response vector,  $\omega$  is the rotational frequency (or simply the frequency) and  $\vartheta$  is the phase.

$$\{x\} = \{X_0\} \cos(\omega t + \vartheta) ; \quad \text{with} \quad \{X_0\} \in R^n \quad (1.2)$$

By taking the first and the second derivative in the time domain of the displacement coordinates  $\{x\}$ , respectively speed and acceleration , it is possible to substitute into in the equation (1.1a) obtaining (1.3), (the cosine is in general different from zero so it can be omitted in the equation).

$$([K] - \omega^2[M]) \{X_0\} = \{0\} \quad (1.3)$$

The non trivial solution is the case of interest of such a equation, then the characteristic equation which represents the eigenvalues problem is ready to be solved (1.4).

$$\det ([K] - \omega^2[M]) = 0 \quad (1.4)$$

The equation (1.4) allows to find the eigenvalues of the system,  $\omega_i^2$ . They correspond to the square of the natural frequencies  $\omega_i$ , where the subscript  $i$  goes from 1 to  $2N$ , and they are usually plot in the *Fre-ND* diagram. In that diagram the natural frequencies are grouped into *families* which describe the different behaviors that can be flexural rather than torsional, according to the complexity of the model, and are plotted against nodal diameter number. Now the eigenvectors  $\{\psi_i\}$ , which represent the mode shapes of the structure, can be easily computed by substituting the eigenvalues in (1.3). The eigenvectors of a cyclically symmetric system show peculiar features. They are divided into two categories, depending on the nodal diameter. The nodal diameters 0 and  $\frac{N}{2}$  are connected to the *stationary* mode shapes, by which all the sectors vibrate with the same amplitude and phase. The other nodal diameters are linked to the *rotating* mode shapes. These modes are grouped in couples for each natural frequency and they are orthogonal with each other. They can be described by harmonic functions of the type  $\cos(n\vartheta)$  or  $\sin(n\vartheta)$ , where their period depends on the nodal diameter  $n$ . The Fre-ND diagram of the system is showed in figure 1.4. Since the model consists of  $2N$  degrees of freedom, two families of natural frequency can be seen in the diagram. In figures 1.5, 1.6 and 1.7 three examples of eigenvectors are reported. In detail, figure 1.5 shows the eigenvectors associated to the nodal diameter 0 and  $\frac{N}{2}$ , while figure 1.6 and 1.7 show those associated to nodal diameters 1 and 5. Note that the rotating eigenvectors have been split into two separate plots in order to distinguish between the degrees of freedom (dofs) of the disk and the degrees of freedom of the blades.

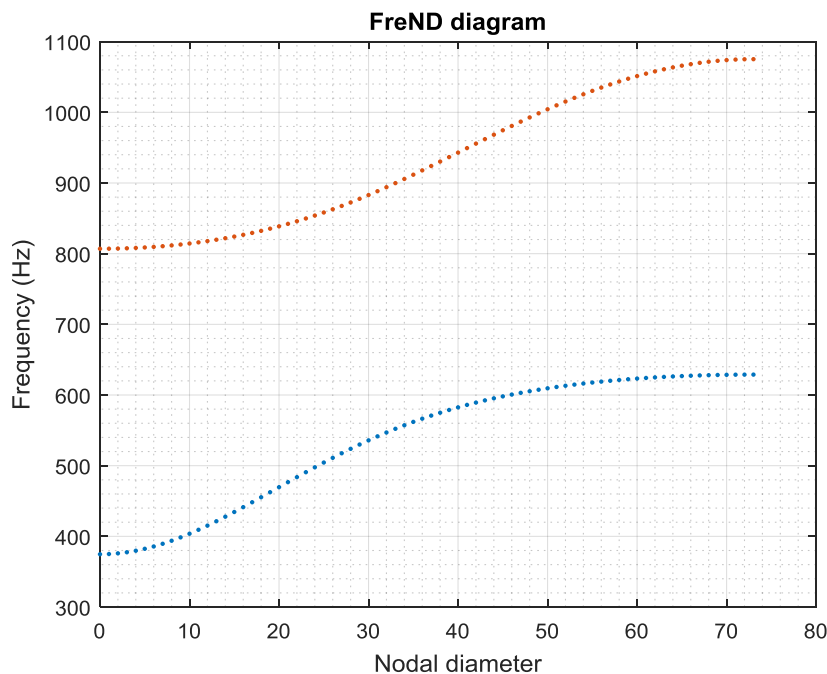


Figure 1.4. Fre-ND diagram

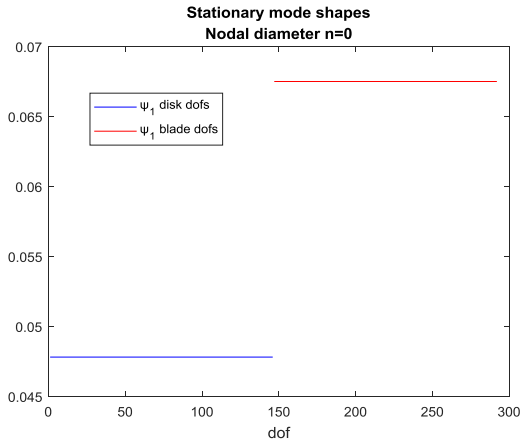


Figure 1.5a. Stationary modes,  $n=0$

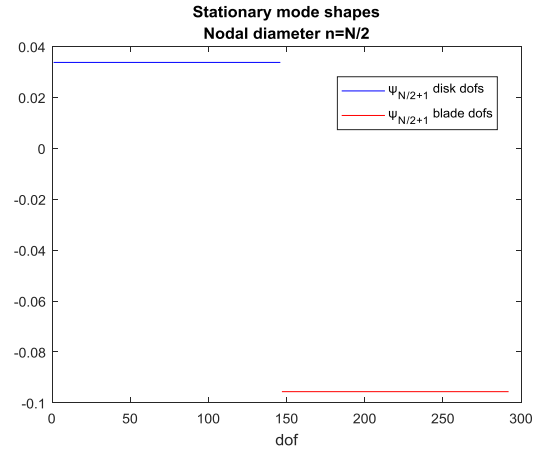


Figure 1.5b. Stationary modes,  $n=N/2$

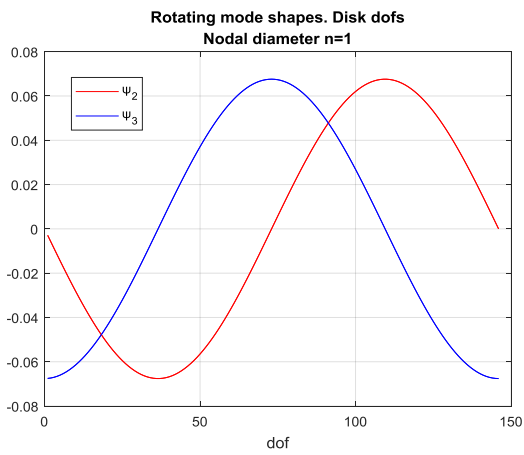


Figure 1.6a. Rotating modes,  $n=1$ , disk dofs

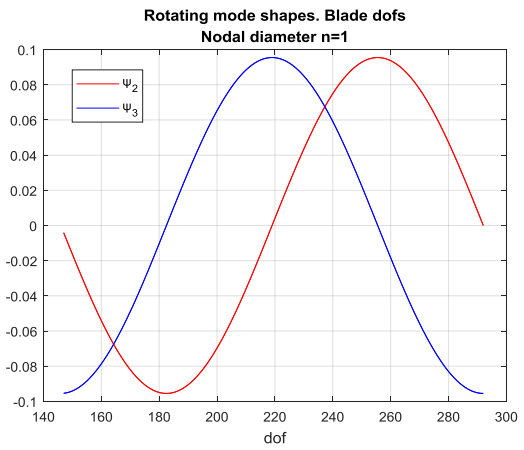


Figure 1.6b. Rotating modes,  $n=1$ , blade dofs

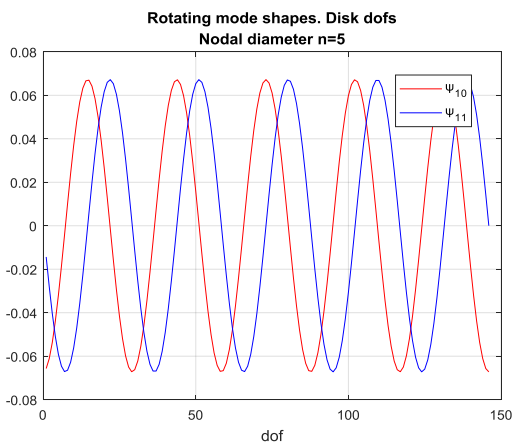


Figure 1.7a. Rotating modes,  $n=5$ , disk dofs

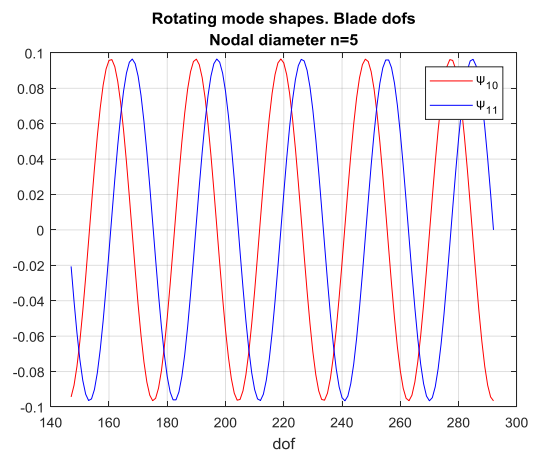


Figure 1.7b. Rotating modes,  $n=5$ , blade dofs

In order to better visualize the mode shapes, in figure 1.8, 1.9 and 1.10 some graphical representations of eigenvectors are showed in a 3D view of the disk which appears deformed according to the specific eigenvectors. These results are obtained by means of a proper CAD system (SOLIDWORKS). The three cases of eigenvectors reported in the figures coincide with the cases in figures 1.5, 1.6 and 1.7, respectively for nodal diameters 0, 1 and 5. A color scale is useful to evidence the deformation of the structure from no deformed areas (dark blue) to highly deformed areas (red).

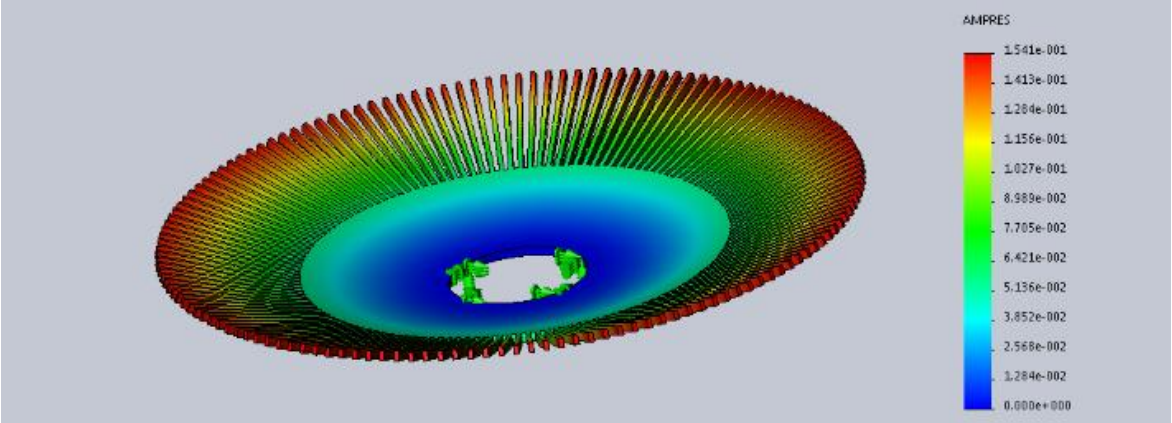


Figure 1.8. 3D view of mode shapes, nodal diameter  $n=0$ .

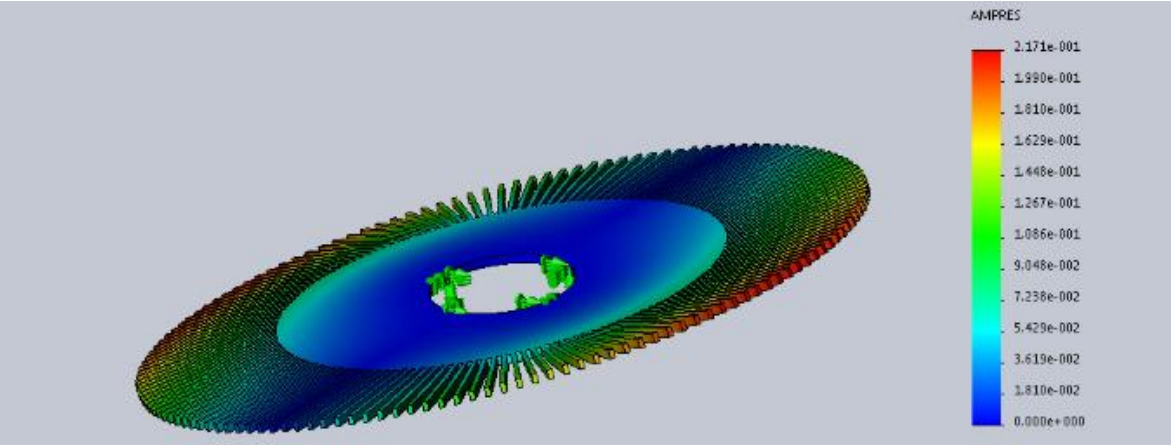


Figure 1.9. 3D view of mode shapes, nodal diameter  $n=1$ .

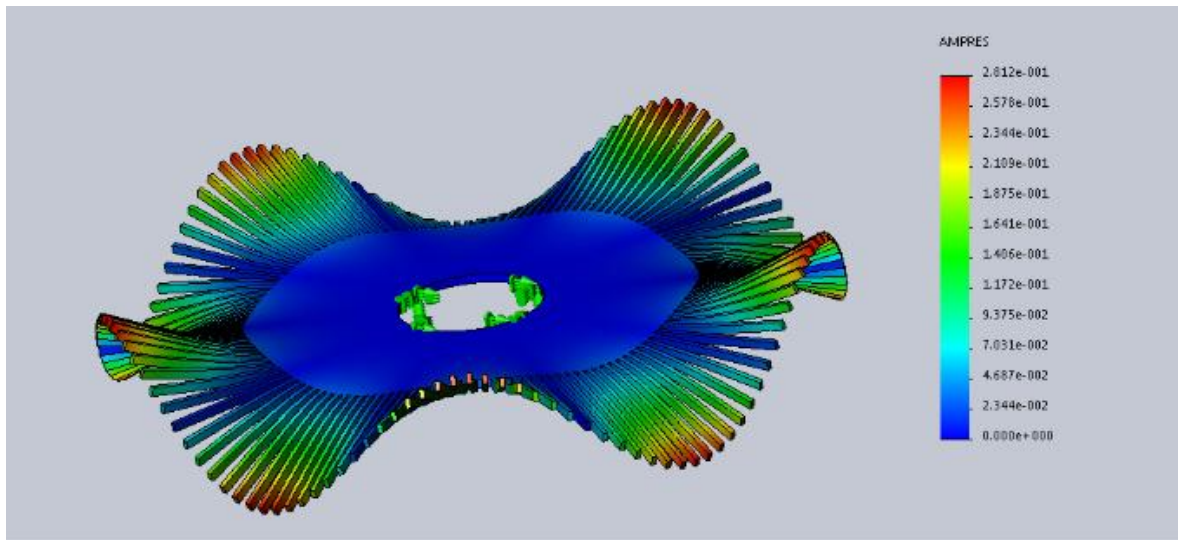


Figure 1.10. 3D view of mode shapes, nodal diameter  $n=5$ .

### 1.3 Cyclic symmetry study

A bladed disk satisfies the property of cyclic symmetry and this can be exploited for the study of the dynamics, reducing a lot the efforts to compute it. In this paragraph the subject is developed and a new model which satisfies the cyclic symmetry property is built, so to be able to study the dynamics of the system by focusing on a single sector. Then, it proceeds by considering the lumped parameters model of the sector. Among the various solution, here one is adopted and the representation of the equivalent model is showed in figure 1.11. Referring to the full model (showed in figure 1.3), a sector model is defined in order to respect the cyclic symmetry. For this reason half of the masses of the disk have been considered and only one blade is included in the sector.

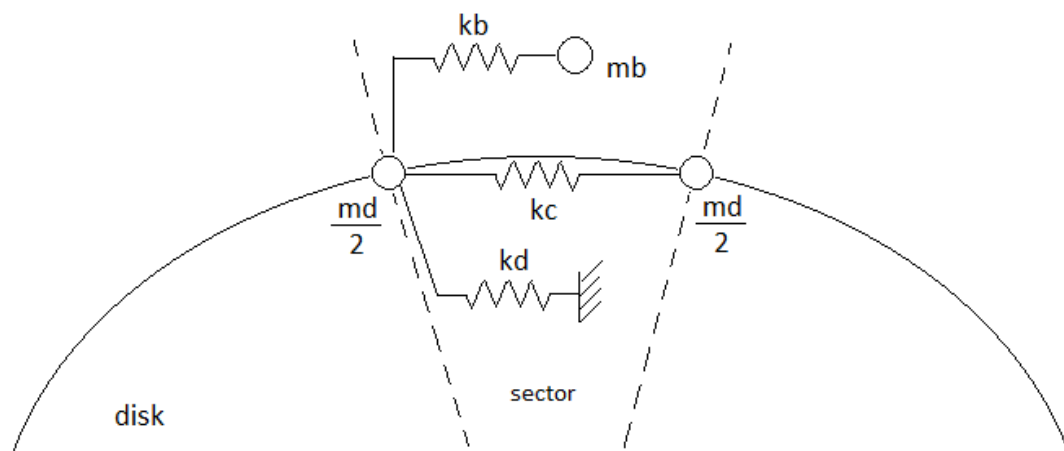


Figure 1.11. Lumped parameters model of the sector.

At this stage, the definition of a new set of physical coordinates is needed in order to write the equations of motion. Now, the model is constituted by three degrees of freedom only. It has to be noted that if the number of sector  $N$  is very large, a remarkable reduction of the problem can be obtained by means of this property. The new set of displacement coordinates is:

$$\{x\} = \{x_{d,L}, x_B, x_{d,R}\}^T \quad (1.5)$$

where

- $x_{d,L}$ , sector left hand side dof.
- $x_B$ , dof associated to the blade.
- $x_{d,R}$ , sector right hand side dof.

Once the new coordinates  $\{x\}$  have been defined, the mass matrix  $[M_s]$  and the stiffness matrix  $[K_s]$  of the system can be built (the detailed procedure to derive these matrices is reported in Appendix 2) and the new set of equations of motion in the matrix form is written in equation (1.6). For easiness in the writing process the parenthesis to identify vectors and matrices are omitted in the equations of motion.

$$M_s \ddot{x} + K_s x = 0 \quad (1.6)$$

Still no information on the other sectors are introduced in the equations, at this stage. Then, a relation between the degrees of freedom which constitute the left and the right boundaries of the sector has to be defined. As a matter of fact, the mode shapes can be expressed by means of harmonic functions and their periods depends on the nodal diameter. A proper choice, for example, is to expressed the right hand side dof as a function of the left hand side dof through the introduction of a phase  $\mu$  (1.7). The phase is the variable dependent on the nodal diameter. Through this condition the degrees of freedom of the system are reduced from three to two, since one dof is immediately defined from the other one. As a consequence, the new set of coordinates  $\{x'\}$  (1.8a) can be related the old  $\{x\}$  multiplying it by a proper transformation matrix  $[T]$ , which contains the phase information (1.8b).

$$\{x_R\} = e^{i\mu} \{x_L\} \quad (1.7)$$

$$\{x'\} = \{x_{d,L}, x_b\}^T \quad (1.8a)$$

$$\{x\} = [T] \{x'\} \quad (1.8b)$$

$$\text{where } [T] = \begin{bmatrix} 1 & 0 \\ 0 & 1 \\ e^{i\mu} & 0 \end{bmatrix}$$

Substituting (1.8b) into (1.6) and multiplying both sides of the equation by the transpose transformation matrix  $[T]^T$  a new set of equations is obtained, where the new mass matrix  $[M'_s]$  and stiffness matrix  $[K'_s]$ , with dimension  $2 \times 2$ , are functions of the phase  $\mu$ , as showed in the equations (1.9).

$$M'_s(\mu) \ddot{x}' + K'_s(\mu) x' = 0 \quad (1.9)$$

$$\text{where:} \quad M'_s(\mu) = [T]^T [M_s] [T] \quad K'_s(\mu) = [T]^T [K_s] [T]$$

The phase  $\mu$  can assume both positive and negative values of the *inter-blade phase angle*  $\varphi_n$  (1.10). For each nodal diameter, a couple of eigenvectors can be computed by performing modal analysis of the system (1.9) and they are collected in the modal matrix  $[\Psi_s(\mu)]_{2 \times 2}$  so to obtain  $\frac{N}{2} + 1$  modal matrices of this type ( if only positive values of inter-blade phase angle are considered ).

$$\mu = \pm \varphi_n = \pm \frac{2\pi}{N} n ; \quad \text{with } n = \left[ 0, \dots, \frac{N}{2} \right] \text{ and } N \text{ even number} \quad (1.10)$$

A comparison between the eigenvectors obtained by studying the full system with  $2N$  degrees of freedom and the eigenvectors obtained by means of the cyclic symmetry can be conducted if the last mentioned eigenvectors are expanded. The expansion is made by multiplying each modal matrix  $[\Psi_s(\mu)]$ , with dimension  $2 \times 2$ , by a proper expansion matrix  $[T_{\psi_s}]$  (1.11), with dimension  $2N \times 2$ , so to get the eigenvectors in the same dimension of those obtained in the full system study. For each nodal diameter a couple of expanded eigenvectors are computed, whether they are stationary or rotating modes.

$$\Psi_{exp}(\mu) = T_{\psi_s} \Psi_s(\mu) \quad (1.11)$$

$$[T_{\psi_s}] = \begin{bmatrix} e^{ik\mu} \\ \dots \\ \dots \end{bmatrix} \text{ with index } k = 0, \dots, N - 1$$

The eigenvectors contained in the expanded modal matrix  $[\Psi_{exp}]$  are complex. It is experimentally verified that they have a phase angle with respect to the full study eigenvectors and they differs in amplitude of a factor equal to  $\sqrt{N}$ . In figure 1.12a and figure 1.12b a 3D view of the eigenvectors (nodal diameters 1 and 5) put into comparison describes better such a concept.

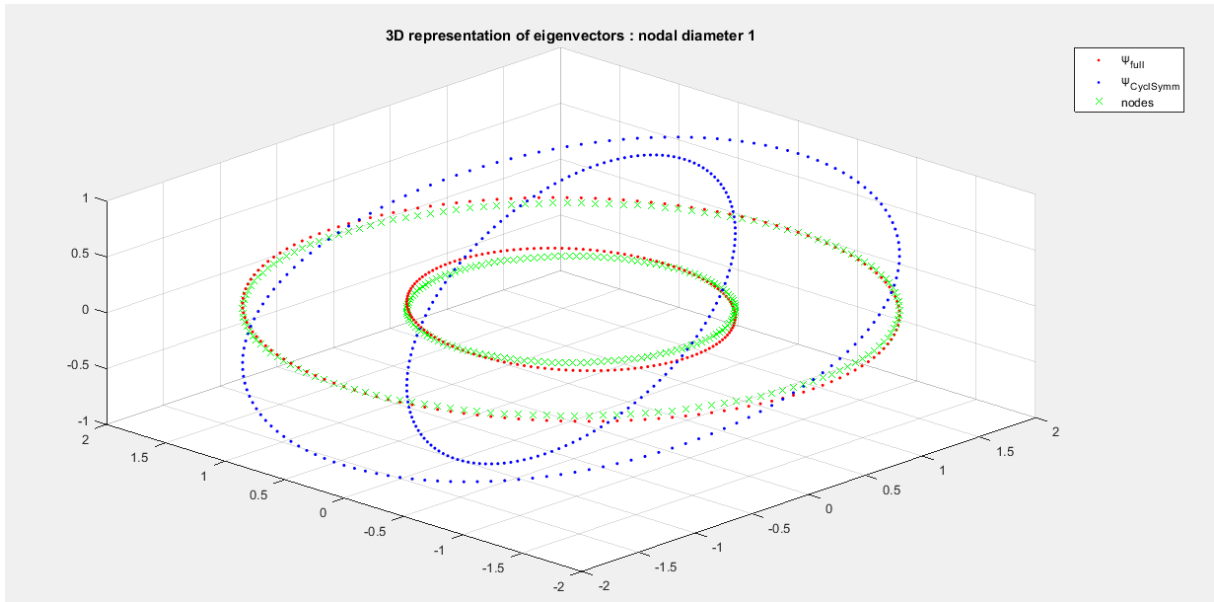


Figure 1.12a. Comparison between full study eigenvectors and expanded eigenvectors, nodal diameter 1.

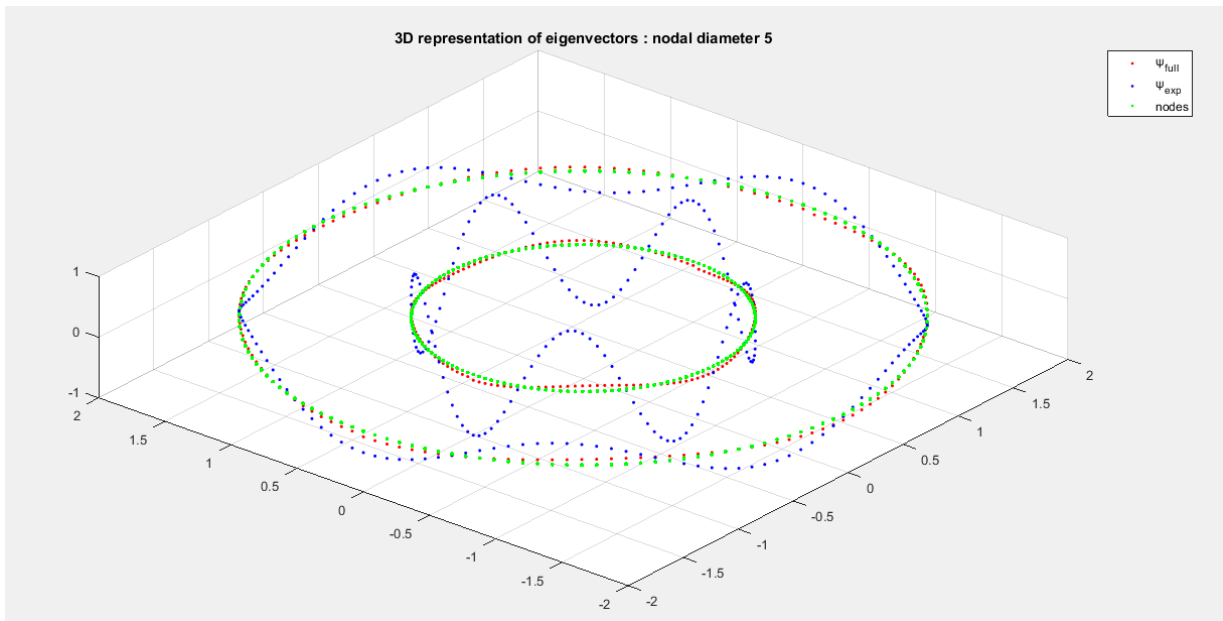


Figure 1.12b. Comparison between full study eigenvectors and expanded eigenvectors, nodal diameter 5

# Chapter 2

## Forced Response

### 2.1 Forced response of the bladed disk

In turbo-machine system, the blades represent usually the most critical components. It is observed from investigations that failures occur because of fatigue. This suggests that the blades vibrate at their resonance frequency with high vibration amplitude and this reduces the component life. Since the resonance conditions are not always avoidable, it is worth to make efforts to study the forced response and resonance of the blades deeply in detail. The external excitation, for a turbo-machine bladed disk in exam, is given by the interaction between the exhaust gases coming from the combustor of the engine. The gas fluxes reach the turbine stage through nozzles which are disposed circumferentially in the direction of the blades. The fact that the turbine rotates makes the excitation force a rotating force in the turbine reference frame (figure 2.1). The excitation frequencies for which resonance occurs are multiple of the rotational speed of the disk. In literature, this concept is described by a quantity called *Engine Order* (EO) (2.1). The Engine Order expresses the ratio between the excitation frequency and the rotational frequency of the disk. The excitation force can be assumed to be an harmonic force. This is not definitely true because the interaction between the gas fluxes and the blades is more impulsive but a Fourier series study can be operated so to deal with harmonic functions.

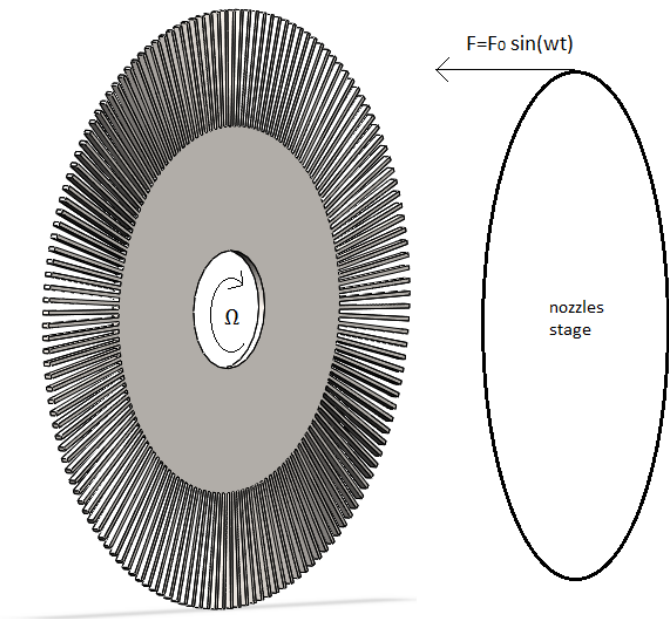


Figure 2.1. Representation of the excitation force.

$$EO = \frac{\omega}{\Omega} \quad (2.1)$$

where  $\omega$  is the excitation frequency and  $\Omega$  is the rotational frequency of the disk.

$$EO = n \quad (2.2a)$$

$$EO = N \pm n \quad (2.2b)$$

The Engine Order, defined in this way, is meant to excite in resonance condition a mode associated to a specific nodal diameter. The equations (2.2) describe the relation between EO and nodal diameter  $n$ . So, a mode with nodal diameter  $n$  can be excited by an EO having the same value but also by an EO equal to  $N \pm n$ . The cause for this last relation (2.2b) is linked with the *aliasing* phenomenon. This phenomenon is very well known in various engineering fields. In this particular case, the rotation of the bladed disk, considering that the blades do not constitute a continuum in space but they are equally spaced along the circumference of the disk, causes a sampling effect of the harmonic force. When the EO is higher than  $\frac{N}{2}$  the sampling of the forcing signal is not “correct”. It means that the disk is not able to see such a excitation force but it sees a force with a lower excitation frequency. Then, each blade undergoes the same excitation force in terms of amplitude but with a phase lag which depends on the position of the blade. The excitation force vector  $\{F\}$  acting on the blades, in the rotating reference frame, fixed to the disk, can be written (equation 2.3) as an harmonic function with excitation frequency  $\omega$  and amplitude  $\{\overline{F}_0\}$ . The vector  $\{\overline{F}_0\}$  is a complex vector (2.4), because it introduces into the expression the inter-blade phase angle together with the information of the position of the blade.

$$\{F\} = \{\overline{F}_0\}e^{i\omega t} \quad (2.3)$$

$$\{\overline{F}_0\} = \{F_0\}e^{i\varphi m} \quad (2.4)$$

where

- $\{F_0\}$ , amplitude vector of the forcing function ( $F_0 \in \mathbb{R}$ ).
- $\varphi$ , inter-blade phase angle ( $\varphi = \frac{2\pi}{N}n = \frac{2\pi}{N}EO$ ).
- $m$ , position number of the blade ( $m = 1, \dots, N$ ).

In order to evaluate the forced response of the system a damping matrix has to be considered in the equations of motion system (2.5). For simplicity damping is assumed to be a proportional viscous damping. This assumption allows to build the damping matrix by fixing a value of modal damping ratio  $\zeta_r$  for each mode. Since the modal masses and the modal stiffness are known from the modal analysis, a modal damping matrix can be derived. As a consequence, the damping matrix  $[C]$  can be computed by pre-multiplying the modal damping matrix  $[c_r]$  by the inverse of the transpose modal matrix,  $([\Psi]^T)^{-1}$ , and post-multiplying  $[c_r]$  by the inverse of the modal matrix  $[\Psi]^{-1}$ , (2.6).

$$[M]\{\ddot{x}\} + [C]\{\dot{x}\} + [K]\{x\} = \{F\} \quad (2.5)$$

$$[C] = ([\Psi]^T)^{-1}[c_r][\Psi]^{-1} \quad (2.6a)$$

$$[c_r] = \text{diag}(2\zeta_r\sqrt{k_r m_r}) \quad (2.6b)$$

The differential equations system admits solutions of the type (2.7). Substituting (2.7) into (2.5) and taking the first and the second derivative of (2.7) it is possible to derive the expression of the response amplitude  $\{X_0\}$  in the frequency domain as the product of the inverse of the dynamic stiffness matrix  $[K_{dyn}]^{-1}$  and the force vector  $\{\bar{F}_0\}$  (2.8).

$$\{x\} = \{X_0\}e^{i\omega t} \quad \text{with} \quad X_0 \in \mathbb{C} \quad (2.7)$$

$$\{X_0\} = [K_{dyn}]^{-1}\{\bar{F}_0\} \quad (2.8a)$$

$$[K_{dyn}] = [K] - \omega^2[M] + i\omega[C] \quad (2.8b)$$

Two main facts emerge from the computation of the forced response. The resonance frequency changes as the EO changes and also the amplitude changes with EO. The trend of the resonance frequencies can be observed in the Campbell diagram. This diagrams collects the resonance frequencies as functions of the rotational speed of the disk and the EO. The figure 2.2 and the figure 2.3 show respectively the Campbell diagram and the forced response of the blades for different values of EO. This results have been obtained by considering a unitary amplitude external force (force applied to the blades dofs only), a modal damping ratio of 0.1% for a bladed disk with 146 blades. In the Campbell diagram the aliasing phenomenon can be clearly highlighted, in fact, as the EO gets higher than  $\frac{N}{2}$  ( E80, E90, E100) the resonance frequencies start to decrease.

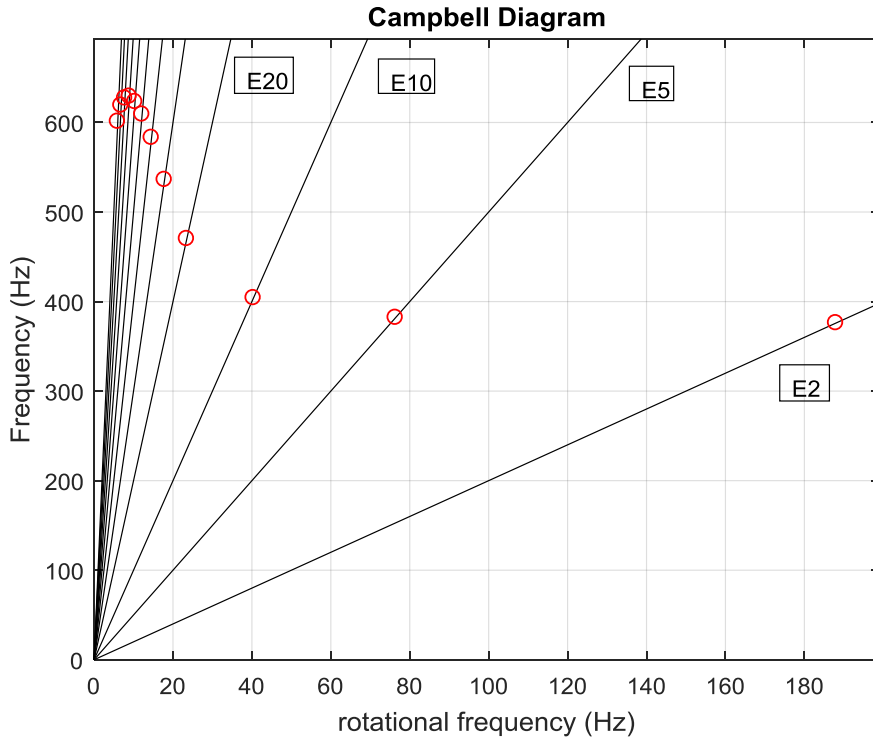


Figure 2.2a. Campbell diagram.

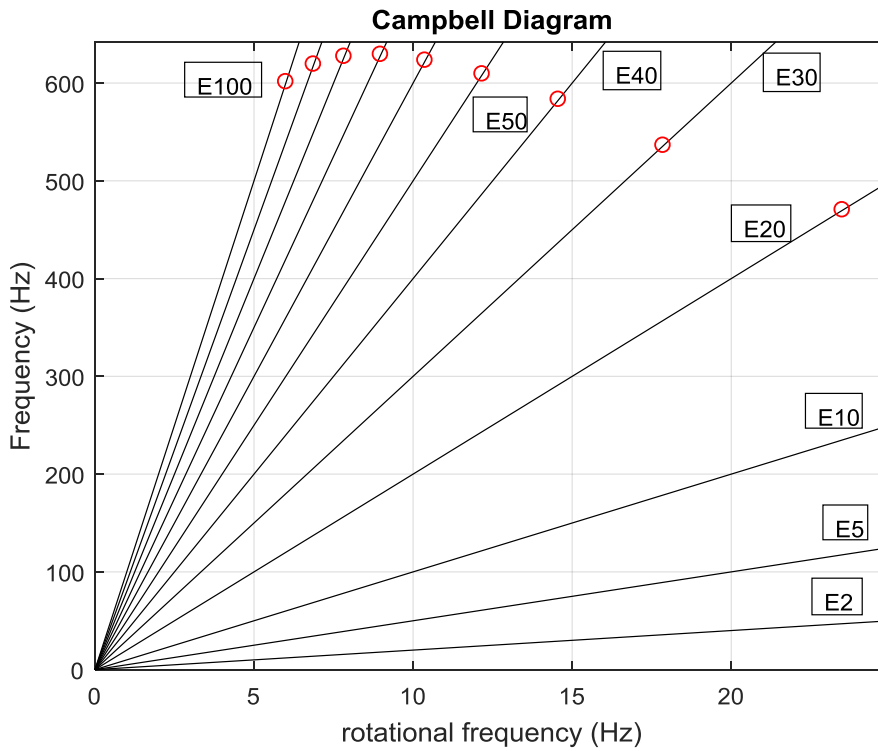


Figure 2.2b. Enlargement of the Campbell diagram in the high EO zone.

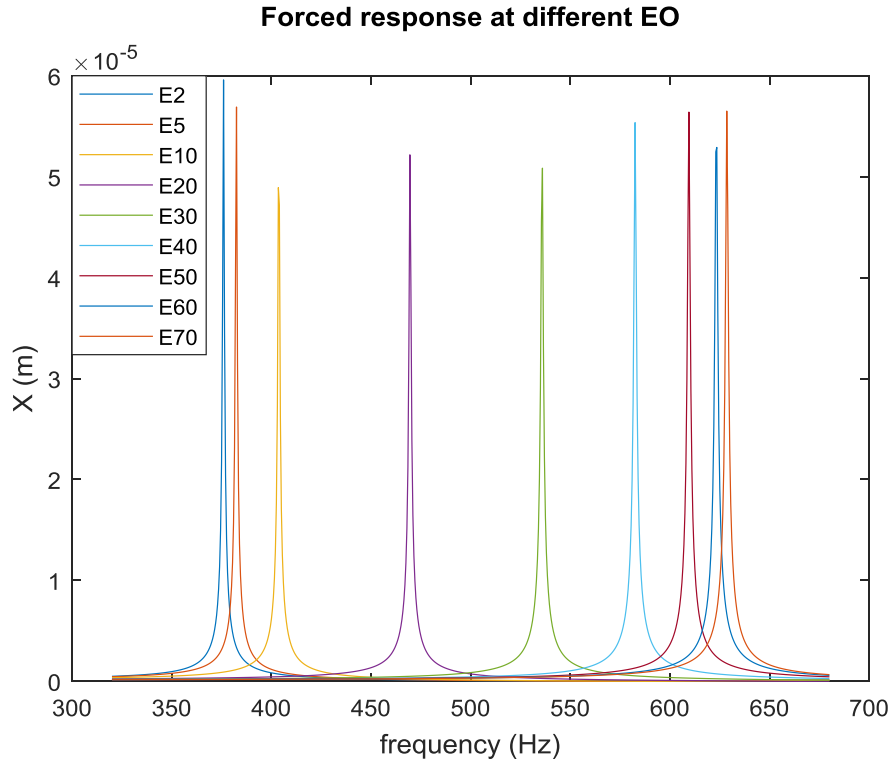


Figure 2.3. Forced response of the blade at different EO.

## 2.2 Forced response by means of cyclic symmetry

The forced response of the system can be also computed by exploiting the cyclic symmetry property. As it was already explained in Chapter 1, the method allows to reduce remarkably the number of degrees of freedom. The choice of the sector model leads to a system having three degrees of freedom only. The excitation force, as in the full system analysis, is applied to the degree of freedom of the blade. The EO enters the equations by means of the phase  $\mu$ , through which the continuity relation between the left hand side dof and the right end side dof is established. By recalling the equation of motion in cyclic symmetry (1.9), a damping matrix, obtained in the same way of the damping matrix in the full system analysis, is introduced into the equation (2.9).

$$M'_s(\mu) \ddot{x}' + C'_s(\mu) \dot{x}' + K'_s(\mu) x' = \{F_{0_s}\} e^{i\omega t} \quad (2.9)$$

Being  $\{x'\} = \{x_{a,L}, x_b\}^T$ , the amplitude force vector is  $\{F_{0_s}\} = \{0, F_0\}^T$ . The forced response can be computed through the inversion of the dynamic stiffness matrix, as in the case of the full system study. In figure 2.4 the forced response of the blade computed in the full-system model and the one computed by means of the cyclic symmetry are put in comparison. They can be perfectly overlapped.

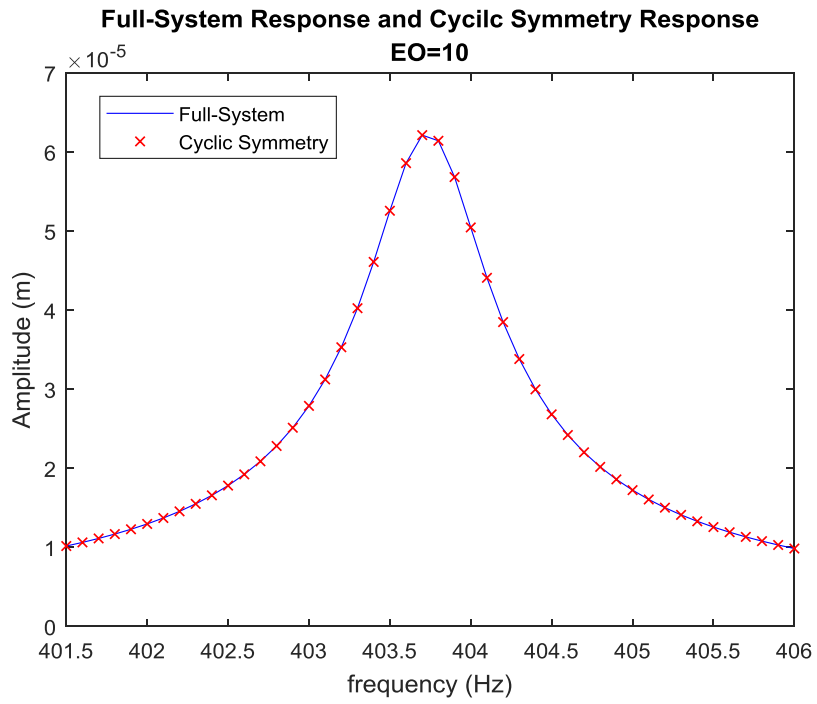


Figure 2.4. Full-System and Cyclic Symmetry Response put in comparison (EO=10).

# Chapter 3

## Mistuning analysis

The mistuning phenomenon affects largely the vibrations of a bladed disk and it makes the design more difficult, since it is not easy to control or predict a priori and it can lead to very different vibration responses in terms of amplitude and resonance frequency. It is based on the fact that the bladed disk is not perfectly symmetric due to uncertainties in the mechanical properties of parts which constitute the whole structure. The aim of this chapter is to analyze the mistuning phenomenon by studying the causes that generate it and deriving the responses associated to a *mistuned* bladed disk.

### 3.1 Brief history of mistuning studies

The mistuning study began in the 1960s when researches like Tobias and Arnolds [1] , Whitehead [2] and Ewins [3] started to analyze, in their works, the physics of the mistuning phenomenon and they laid the foundations for the next studies. They tried to study the vibration of a mistuned bladed disk by giving solutions to avoid the negative effect of such a phenomenon. It is possible to distinguish between two groups of studies: a first group is based on the structural analysis through the study of the forced response of a mistuned bladed disk, among which [1],[2] and [3]; the second group (among the first studies can be cited [4],[5] and [6] ) focused the attention on the aerodynamics aspects for turbo-machine applications, which lead to instability problems like flutter. Despite these efforts in the understanding of the subject, through methodologies which got increasingly sophisticated, the main problems linked to mistuning remained unsolved until the 1990s when different approaches had been adopted in order to better understand the mistuning phenomenon. In fact, new approaches were followed in the early studies which involve the use of lumped parameters model with few degrees of freedom. Also statistical methods have been adopted. After 1990s, contemporary studies led to the definition of a new method called “*Reduced Order Models*” (ROMs) which is based on a realistic finite element model. Among the several researches which were conducted on ROMs, those by Petrov et al. [7] , Yang and Griffin [8] and Feiner and Griffin [9] are cited as representative of the study field. Other contemporary studies, like Griffin[10], Wang [11] and Petrov and Ewins [12], provide modeling with incorporated friction dampers to reduce as much as possible the amplitude vibration in resonance conditions.

### 3.2 Nature of the mistuning phenomenon

The term “mistuning” refers to the hypothesis that the bladed disk is not perfectly symmetric. This situation is due to the fact that there are tolerances on the geometry and the design in general of the bladed disk which affect the production process of the parts and cause the lack of cyclic symmetry of the structure. The mistuning can be also generated by a different behavior of the blades, which are jointed to the disk, and the uncertainty linked to the joints can influence the stiffness of the blades, then the behavior of the whole structure. Here, the attempt is to generate a condition of mistuning, to be applied to the lumped parameters model in exam, and compute the forced response of the blades. Of course, this can be applied only to the full system because of the lack of symmetry of the structure. The cause of mistuning is not known in general. However, here such a condition has to be generated by properly modifying the mechanical properties that are available in the model. This can be done by acting on the masses of the blades  $m_b$  or on the stiffness of blades  $k_b$ . Then, a normal distribution of errors around the nominal value of the property has to be generated, with a known standard deviation and mean value equal to zero. Since the mistuning problem is connected with random errors, it is a good choice to create more than one set of random errors and study all of them separately. Here, five different sets or *pattern* of mistuning have been considered. The figures 3.1 and 3.2 show the probability density function of the first pattern, respectively applied to the masses  $m_b$  (nominal value  $m_{b,nom} = 0.5 \text{ kg}$ ) and to the stiffness  $k_b$  (nominal value  $k_{b,nom} = 9.5 \text{ E6 N/m}$ ).

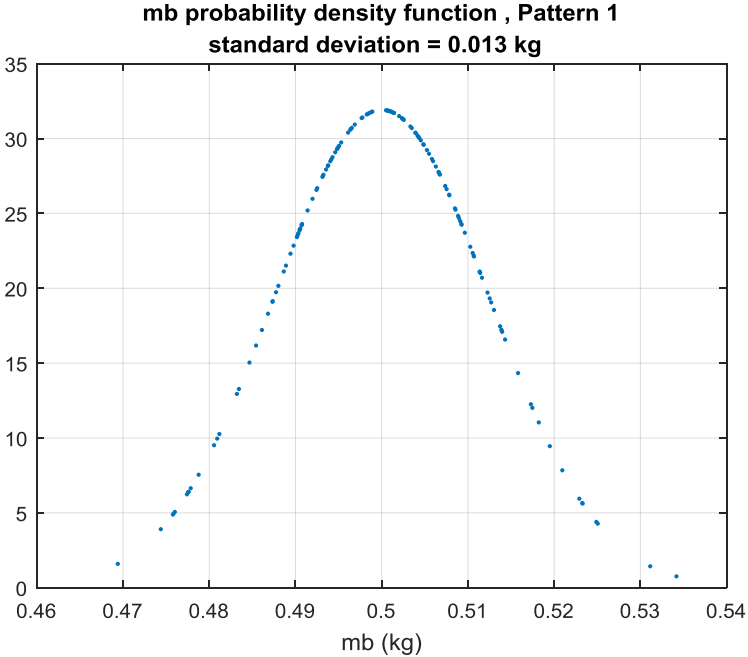


Figure 3.1. Probability density function of the pattern 1 on the masses  $m_b$ .

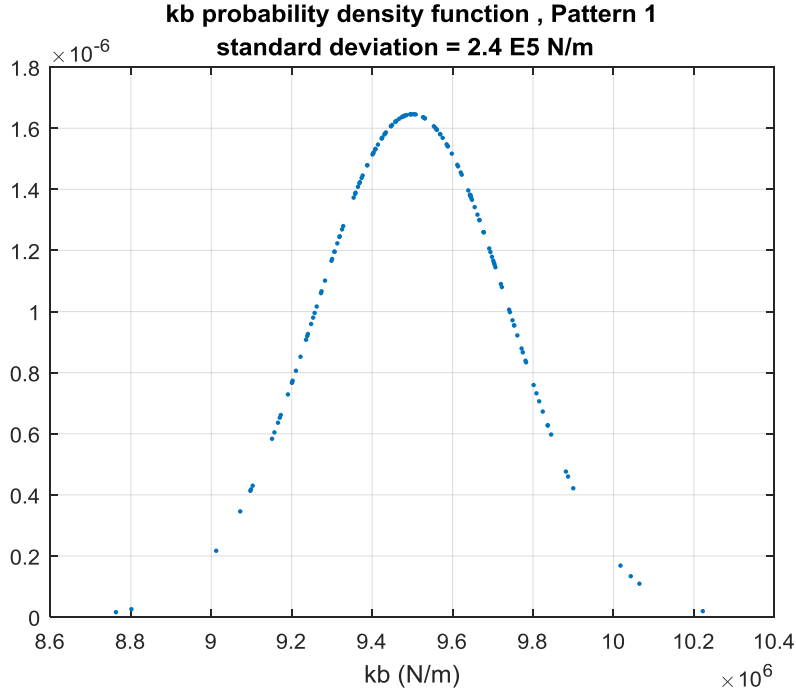


Figure 3.2. Probability density function of the pattern 1 on the stiffness  $k_b$ .

In order to understand well how mistuning affects the forced response of the system it is necessary to consider different level of mistuning. Here the blade masses are supposed to be mistuned, maintaining the stiffness at the nominal value. Then, a good choice is to act on each pattern by amplifying the mistuning level. This results into an amplification of the standard deviation of a specific pattern. Practically, this is done by considering a set of mistuning amplification coefficient  $a_p$  which multiplies the error between the  $i$ -th blade mass  $m_{b,i}$  of the mistuned bladed disk, according to a certain pattern of mistuning, and the nominal value of that mass in the tuned bladed disk case,  $m_{b,nom}$ . This is expressed in the equations (3.1).

$$m_{b,i}^p = m_{b,nom} + a_p \Delta m_{b,i} \quad (3.1a)$$

$$\Delta m_{b,i} = m_{b,i} - m_{b,nom} \quad (3.1b)$$

So, the masses of the blades  $m_{b,i}^p$  are derived by the application of the amplification coefficient  $a_p$  to the error between the  $i$ -th mass of a specific pattern and the nominal value. Since the procedure does not modify the original pattern but it only amplifies the magnitude of mistuning, the parameter which gives the information of this magnitude is the standard deviation  $\sigma^p$  which is derived by the multiplication of the standard deviation of the mistuning pattern  $\sigma_0$  times the amplification coefficient (3.2). This is possible since the amplification of mistuning does not modify the mean value of the pattern which is kept equal to the nominal value  $m_{b,nom}$ .

$$\sigma^p = a_p \sigma_0 \quad (3.2)$$

The forced response is computed for different mistuning magnitudes characterized by different standard deviations, once a specific pattern has been applied. The standard deviations applied to the system are reported in table 3.1, while the figures 3.3 show the  $N$  blade masses of pattern 1 computed for each value of standard deviation.

Standard deviation $\sigma_p$ (kg)								
$a_p$	0,01	0,1	0,5	1	2	3	5	10
$\sigma_p$ (kg)	0,00013	0,0013	0,0065	0,013	0,026	0,039	0,065	0,13

Table 3.1. Standard deviations of the blade mass

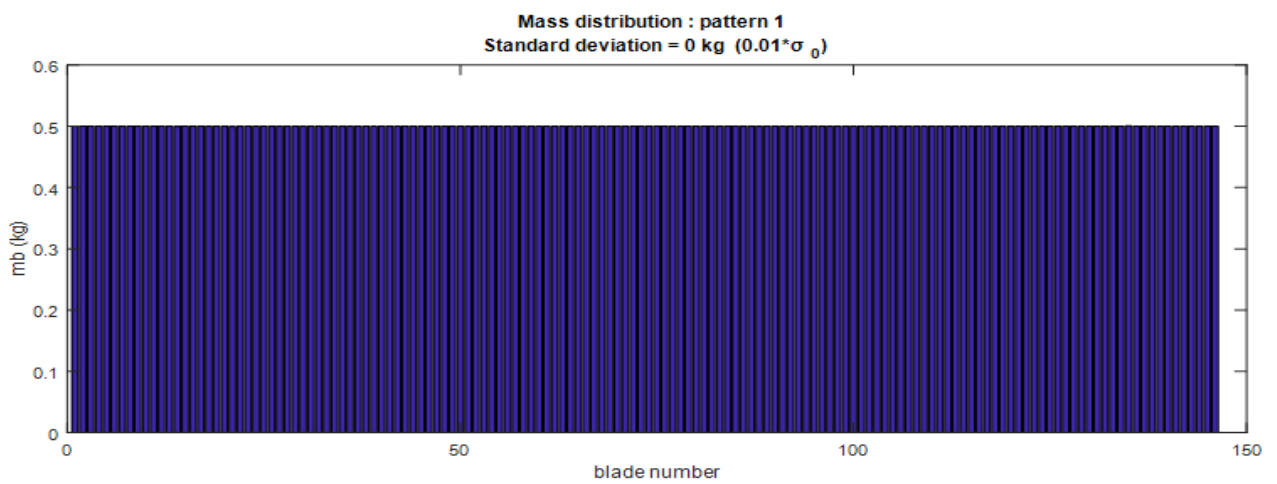


Figure 3.3a. Mass distribution for  $a_p = 0.01$ .

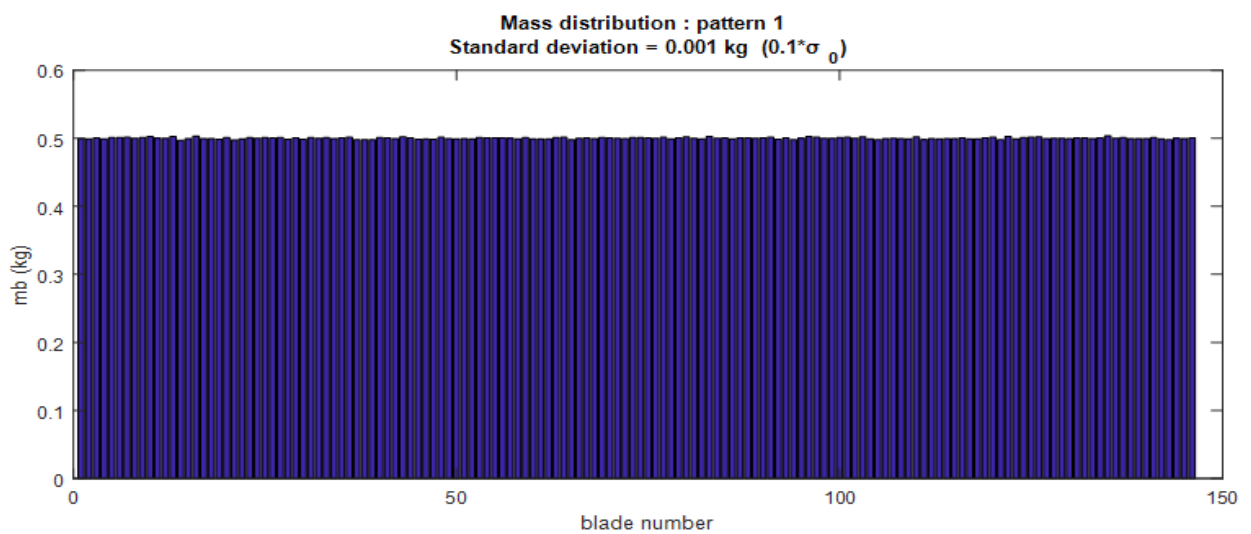


Figure 3.3b. Mass distribution for  $a_p = 0.1$ .

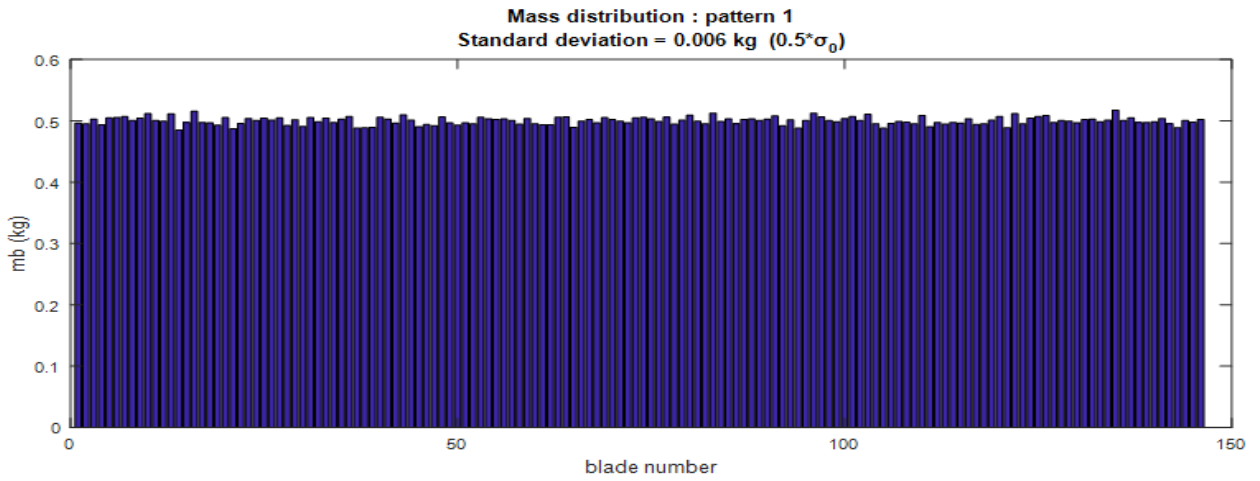


Figure 3.3c. Mass distribution for  $a_p = 0.5$ .

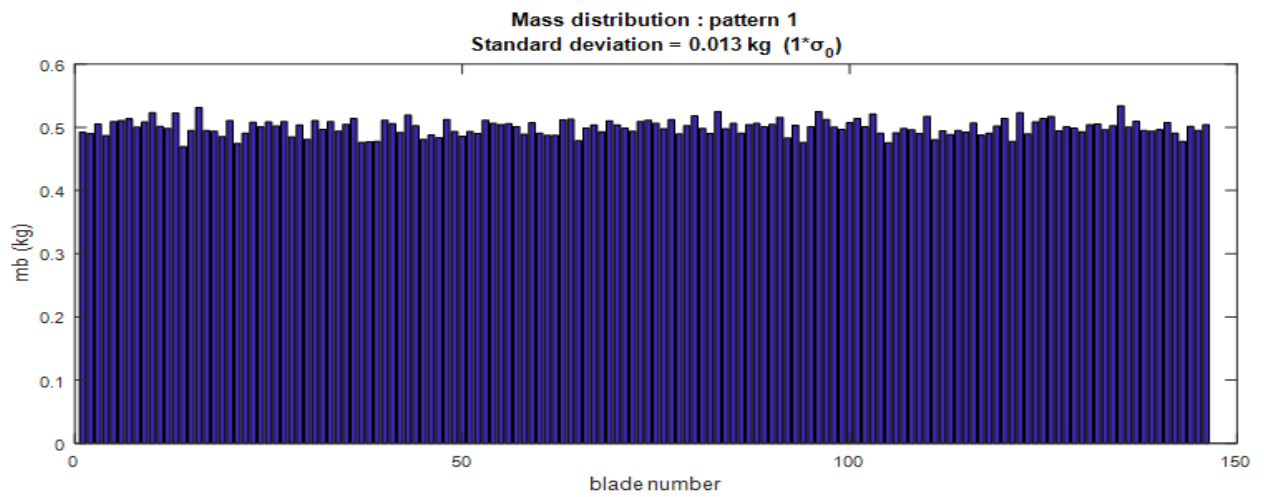


Figure 3.3d. Mass distribution for  $a_p = 1$ .

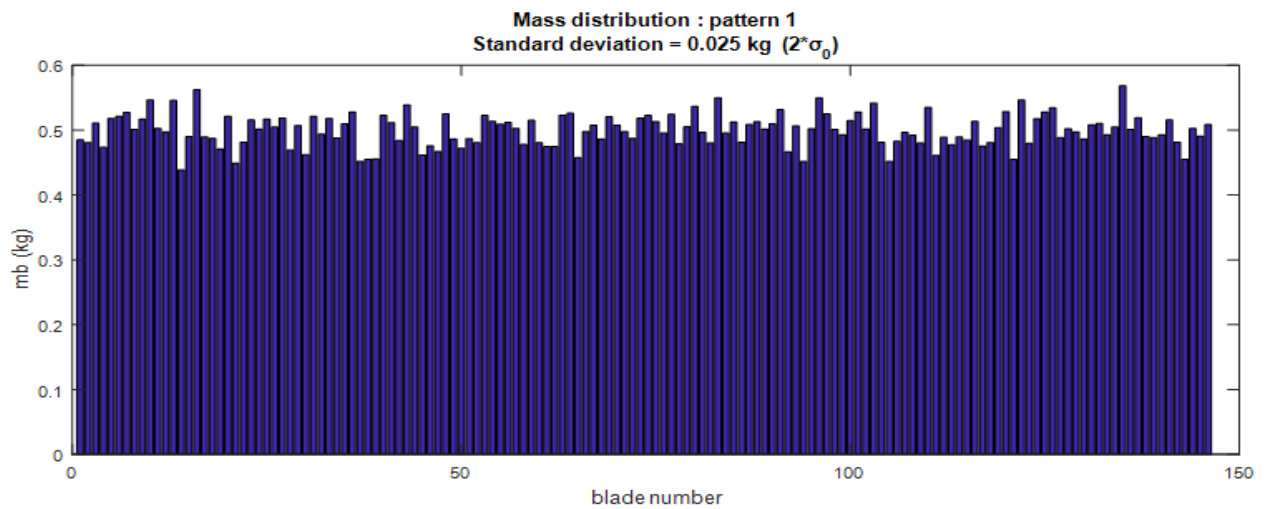


Figure 3.3e. Mass distribution for  $a_p = 2$

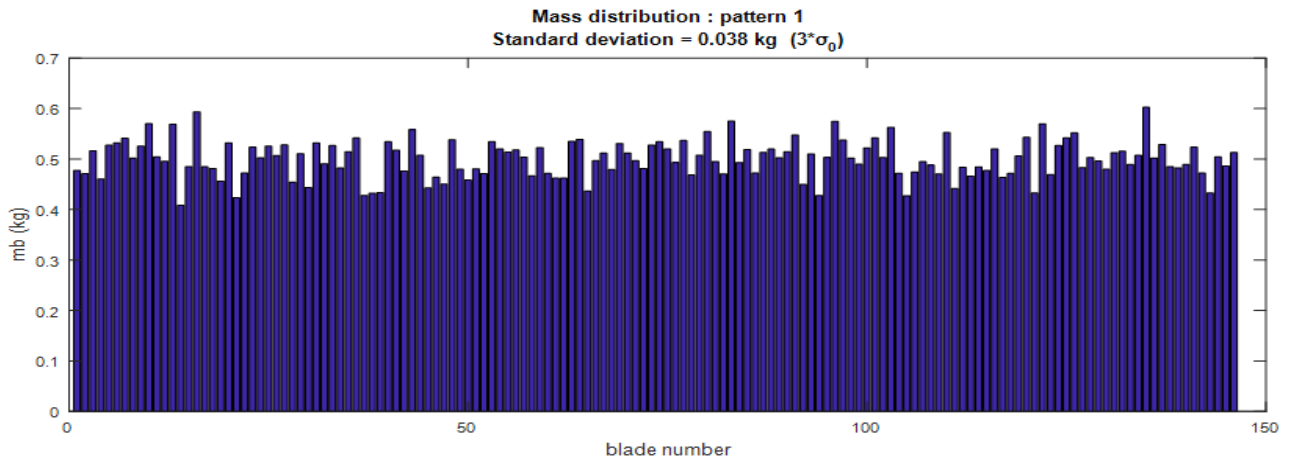


Figure 3.3f. Mass distribution for  $a_p = 3$ .

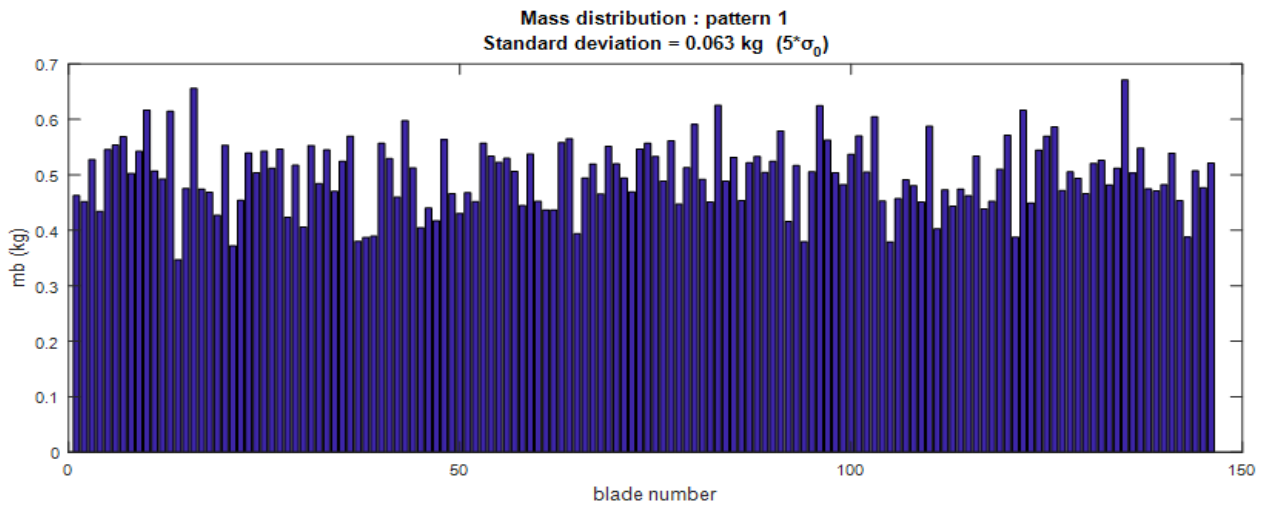


Figure 3.3g. Mass distribution for  $a_p = 5$ .

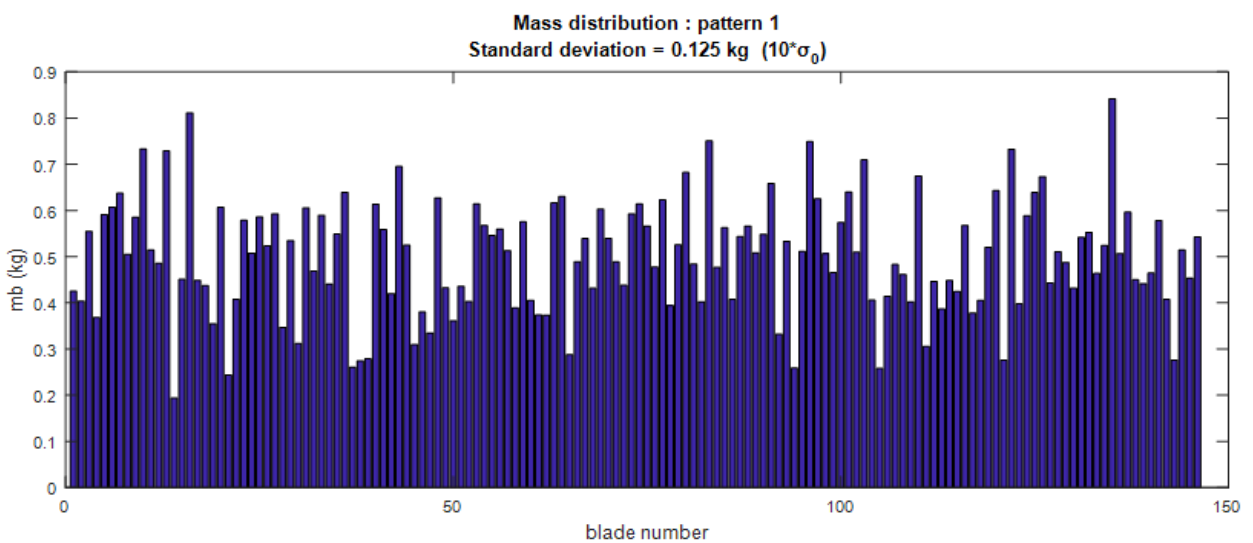


Figure 3.3h. Mass distribution for  $a_p = 10$ .

### 3.3 Effects of mistuning on the forced response

Once the masses have been defined for each level of mistuning, they can be applied to the models in order to build the new mass and stiffness matrix of the mistuned bladed disk,  $M_{mis}$  and  $K_{mis}$ , and the forced response can be computed. The most significant result of the forced response is that the blades do not vibrate in the same way, differently from the case of a tuned bladed disk. Some blades can vibrate with an amplitude which is considerably higher with respect to the tuned case. This represents a very critical issue at the design stage because mistuning is something that cannot be known a priori but it affects a lot the response. The aim of the computation is to understand the behavior of the mistuned structure and to explore the response of all the blades at different levels of mistuning. In figures 3.4 are reported some example of blade responses derived for different amplification coefficients ( $a_p$  going from 0.01 to 3). The responses are computed by assuming a unitary amplitude of the external force and EO equal to 5. From these figures it is easy to see that the mistuning level influences remarkably the forced response in different ways from one blade to another one. Some of them undergo a large increase in the amplitude (figure 3.4d) when the amount of the mistuning increases. Others do not show any considerable change (figure 3.4a) or can also decrease in amplitude, showing sometimes two peaks in the neighborhood of the resonance frequency of the tuned case. This last situation suggests that, for some blades, mistuning can also behaves as a dynamic absorber. Since each blade response is different from the others, it is useful to plot into a unique diagram the maximum amplitudes of all the responses against amplification coefficient. For a more intuitive diagram is convenient to provide the *magnification factor* of the blades, which expresses the normalized maximum amplitude with respect to the tuned case. Figures 3.5 show the trend of the magnification factors of all the blades as functions of the amplification coefficients, for different patterns (EO =5).

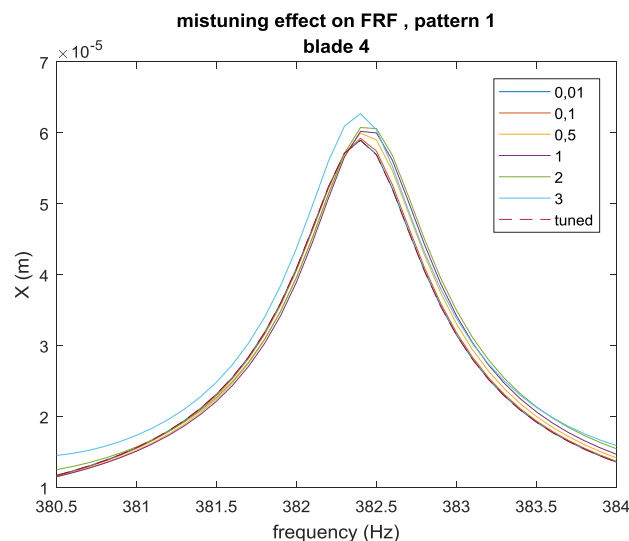


Figure 3.4a. Forced response of blade 4 by varying  $a_p$ .

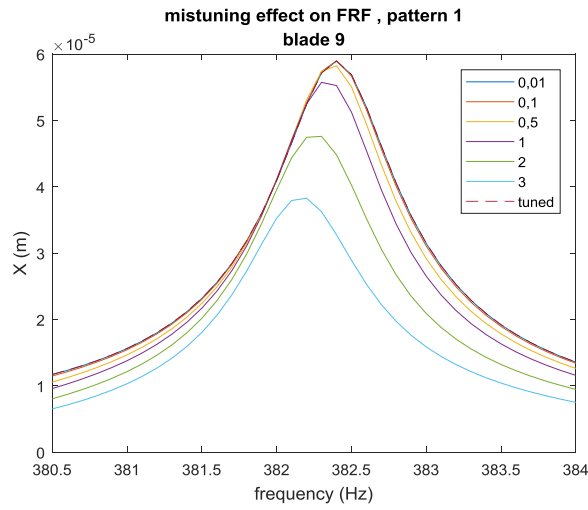


Figure 3.4b. Forced response of blade 9 by varying  $a_p$ .

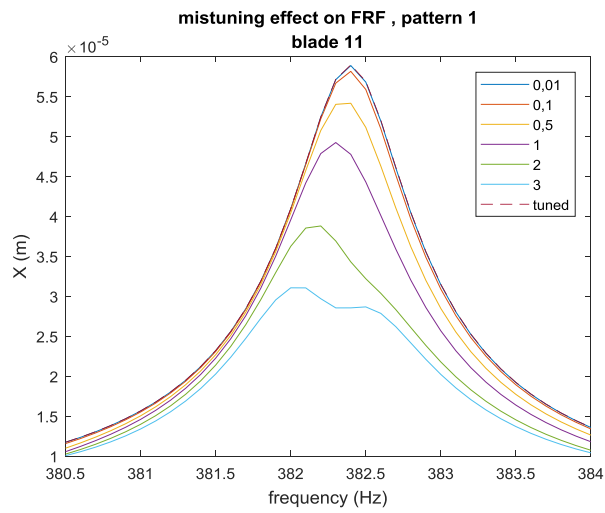


Figure 3.4c. Forced response of blade 11 by varying  $a_p$ .

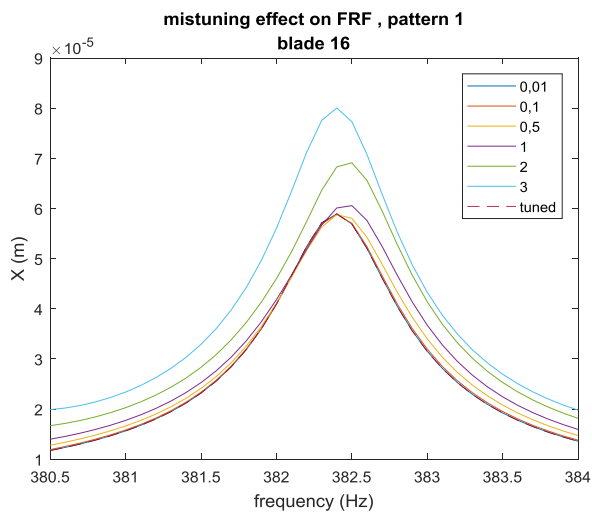


Figure 3.4d. Forced response of blade 16 by varying  $a_p$ .

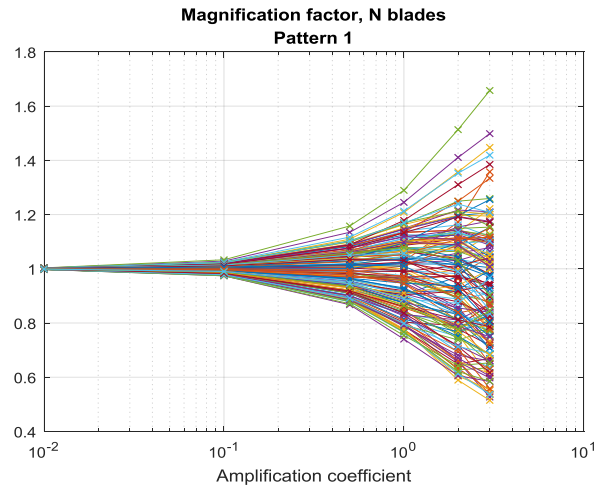


Figure 3.5a. Magnification factors against  $a_p$  ( pattern 1 ).

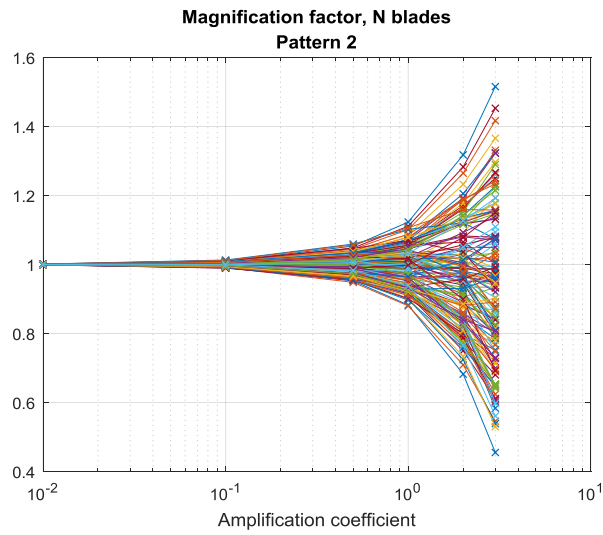


Figure 3.5b. Magnification factors against  $a_p$  ( pattern 2 ).

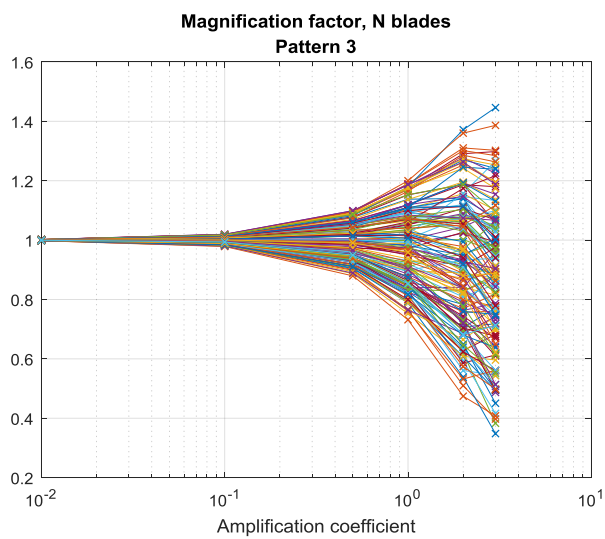


Figure 3.5c. Magnification factors against  $a_p$  ( pattern 3 ).

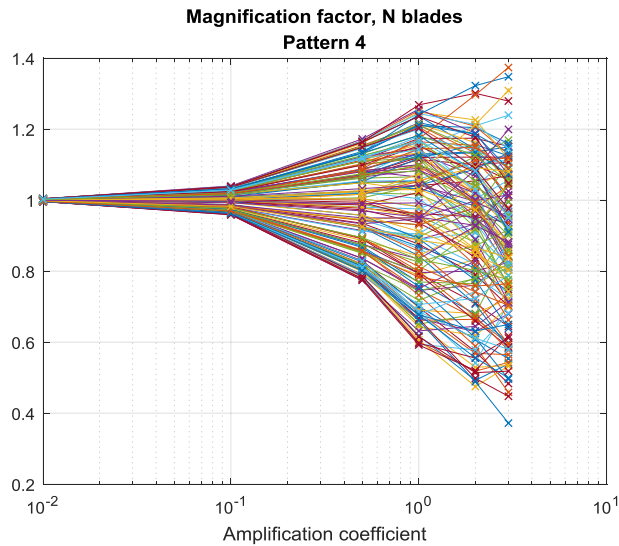


Figure 3.5d. Magnification factors against  $a_p$  ( pattern 4 ).

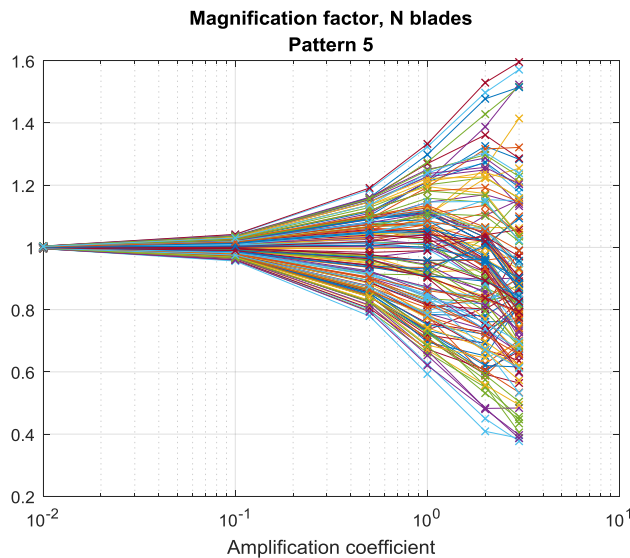


Figure 3.5e. Magnification factors against  $a_p$  ( pattern 5 ).

From figures 3.5 different trends of the magnification factor can be noted. For very low amplification coefficients (0.1, 0.01) the mistuned disk behaves as if it was tuned (magnification factor = 1). As the amount of mistuning increases, some of the magnification factors get very high value, others reach a maximum and then decrease. In the figures 3.6 the magnification factors of each blade are compared with the mass distribution, according to a specific pattern and amplification coefficient. It is interesting to note that, even for a small perturbation in the mass, two adjacent blades can have completely different responses. So, the mistuning phenomenon has not to be connected to the mechanical properties of each single blade, separately, but to the fact that such a perturbation, interacting with EO of the external force, cause the energy to converge toward specific disk portions. By looking at figures 3.6a-3.6f, the envelope of the magnification factors describes a wave trend, whose period is strictly connected to the EO of the force and wave amplitude which increases with the amount

of mistuning. This “ordinate” distribution of the magnification factors cannot be correlated in any way to the “random” mass distribution by only looking at the figure. One issue connected to such analysis can occur when the amplification coefficient which is provided to mass distribution is too high (figure 3.6g and 3.6h). In that case the response is affected a lot by the large deformation that is given to the system. The mechanical properties of each blade have an influence on the response of the blade itself which is no more negligible and it tends to hide the mistuning effect. A large mass makes the blade less stiff, as a consequence it vibrates more with respect to other masses. This situation demonstrates that mistuning doesn't affects the vibration of each blade separately but the way in which the energy is distributed among the various portions of the bladed disk.

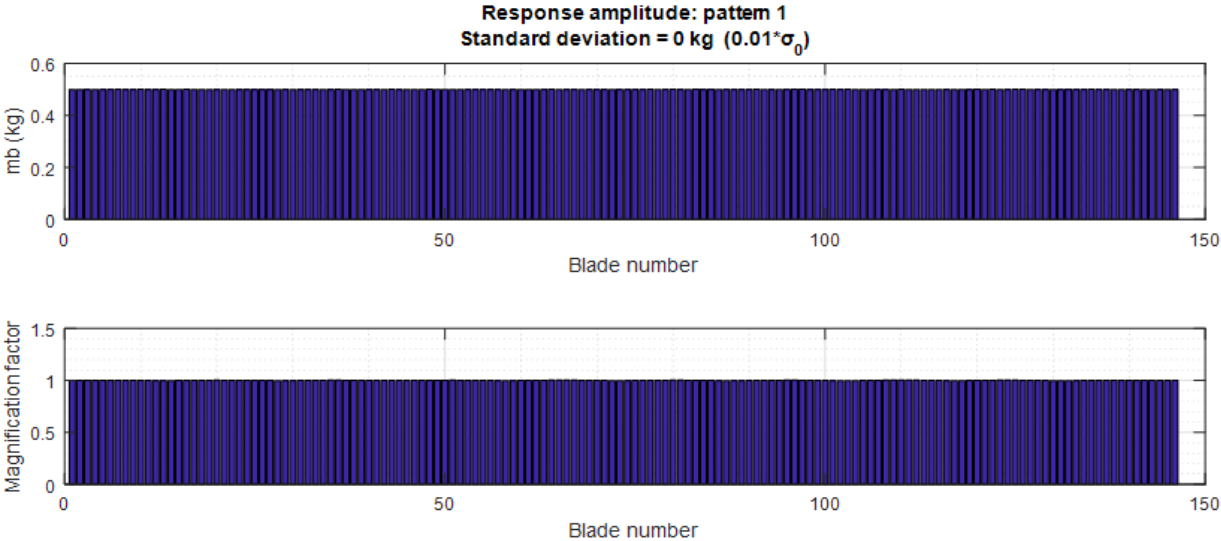


Figure 3.6a. Magnification factors and mass distribution ( $a_p = 0.01$ ).

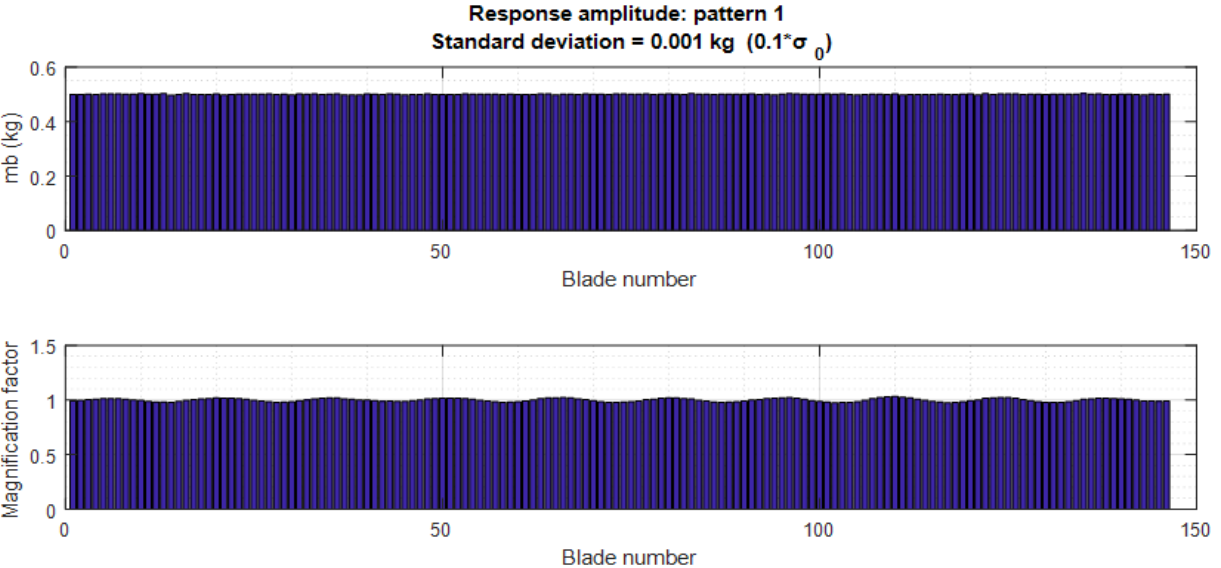


Figure 3.6b. Magnification factors and mass distribution ( $a_p = 0.1$ ).

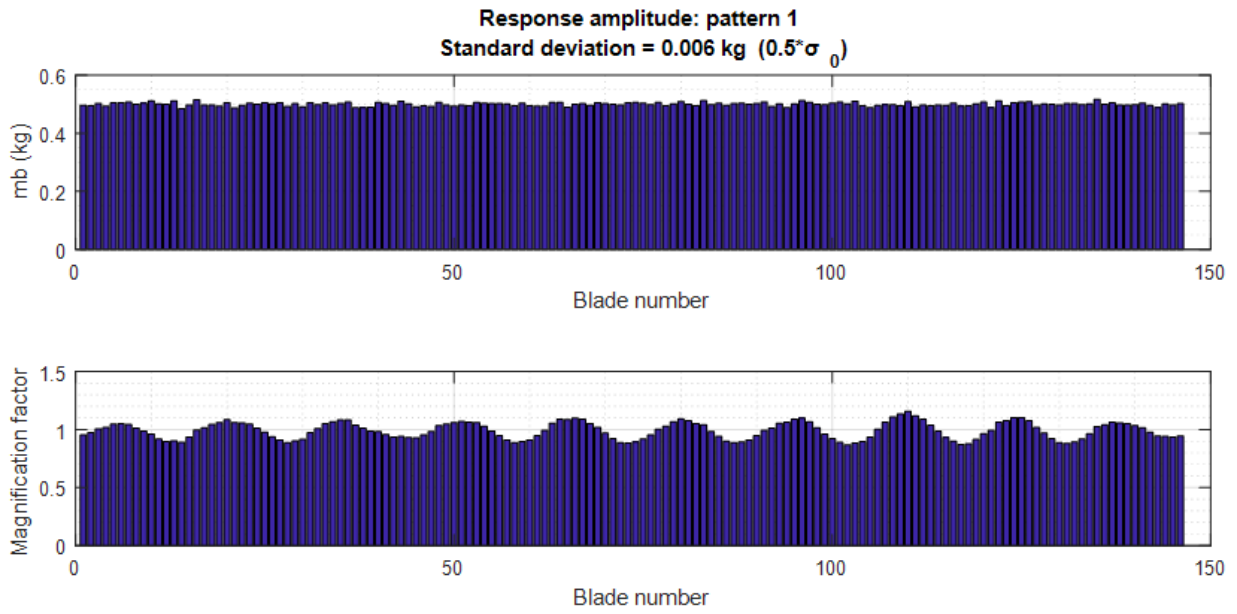


Figure 3.6c. Magnification factors and mass distribution ( $a_p = 0.5$ ).

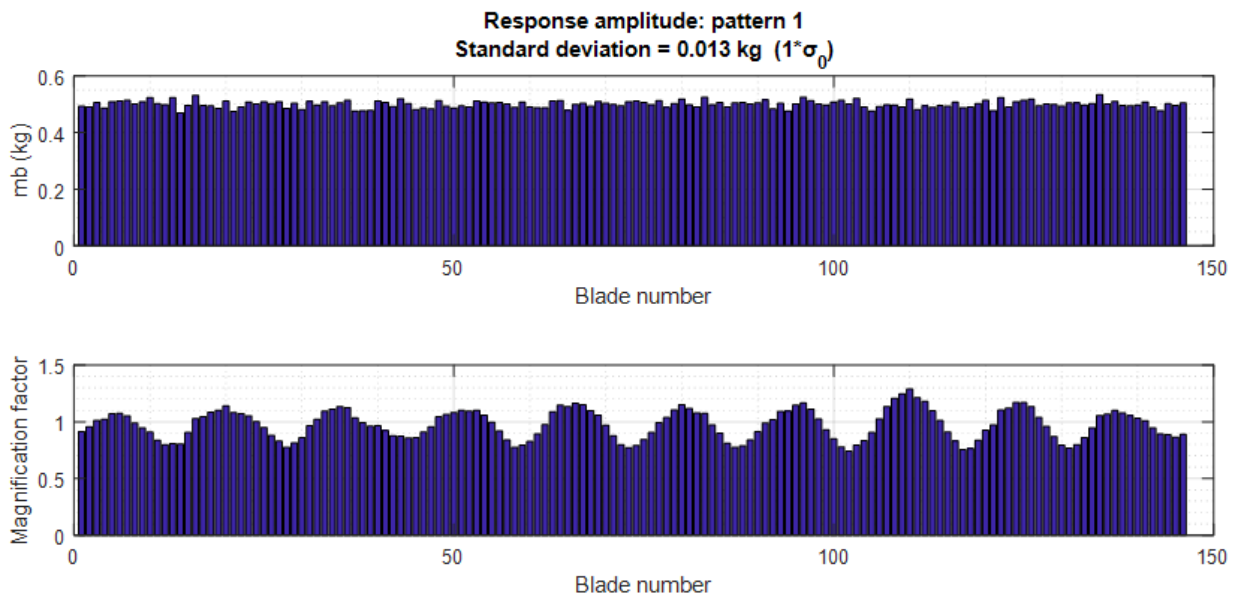


Figure 3.6d. Magnification factors and mass distribution ( $a_p = 1$ ).

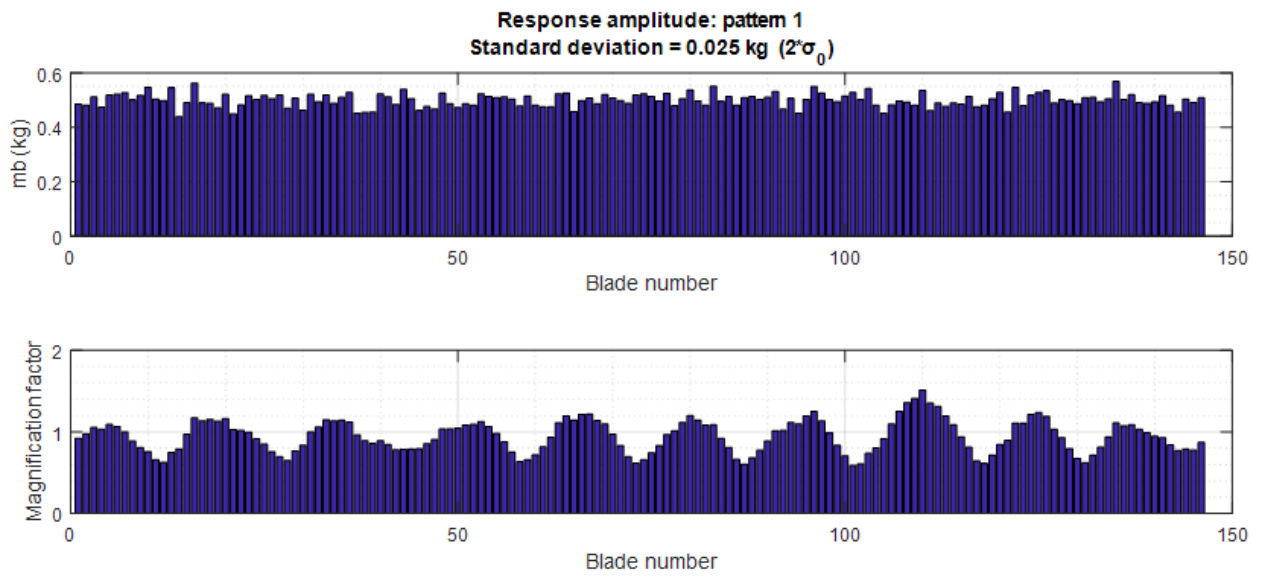


Figure 3.6e. Magnification factors and mass distribution ( $a_p = 2$ ).

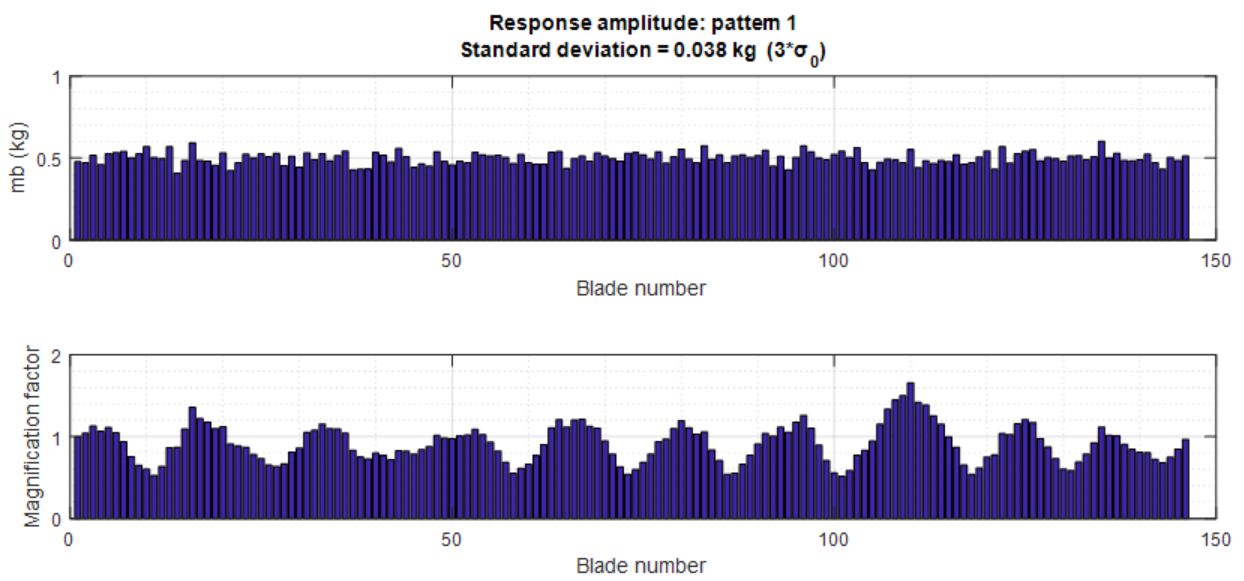


Figure 3.6f. Magnification factors and mass distribution ( $a_p = 3$ ).

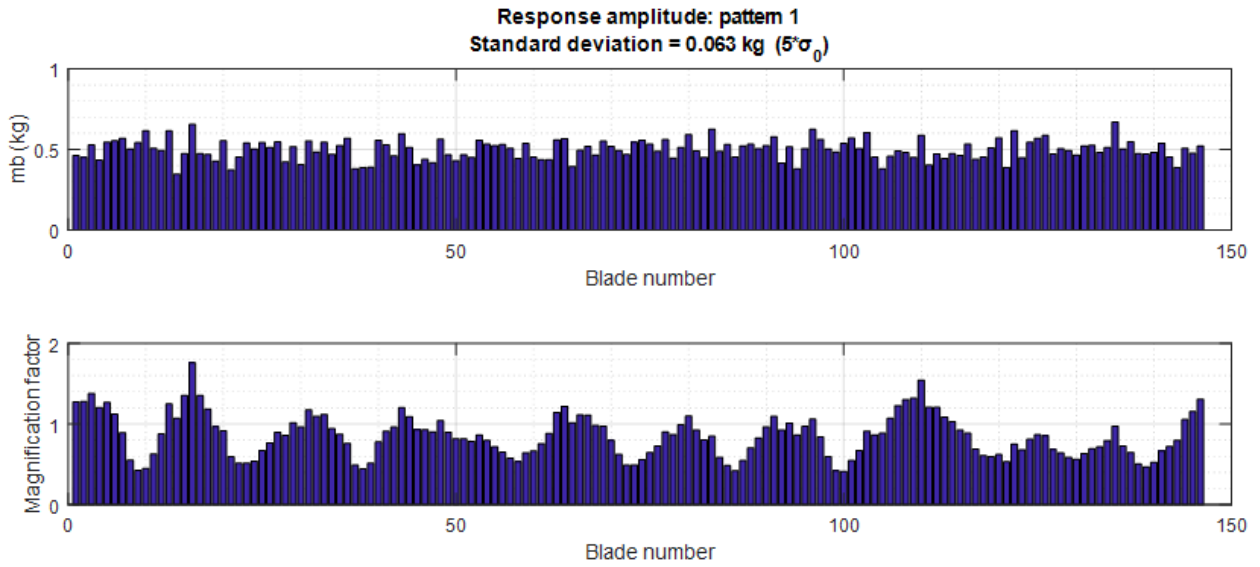


Figure 3.6g. Magnification factors and mass distribution ( $a_p = 5$ ).

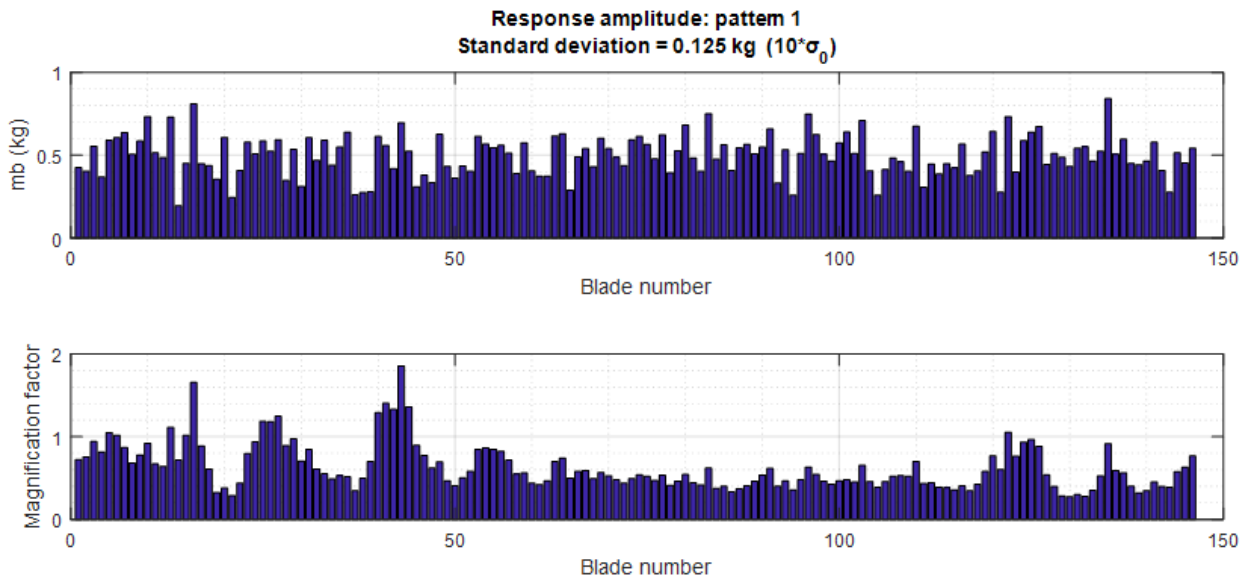


Figure 3.6h. Magnification factors and mass distribution ( $a_p = 10$ ).

A worse situation occurs when the Engine Order is very high. As a matter of fact, a certain amount of mistuning, even if it is small, leads to very different and unpredictable response from one blade to the other. The reason for that is suggested by the Fre-ND Diagram in figure 1.4 (chapter 1). The natural frequencies trend has a decreasing slope as the nodal diameter increases. This means that in a certain frequency range, more than one nodal diameter are excited. The combined contribution of “mistuned” modes causes the response to be unpredictable and leads to responses amplitude that can be very high, for some blades. Examples of forced response with high EO ( EO=60 ), under mistuning conditions, are

reported in the following figures (3.7). It is easy to note that, even for small amplification coefficients, the response amplitudes reach very high value, with respect to the amplitudes computed for an EO equal to 5 (figures 3.6). By increasing the amplification factor, the wavy form of the magnification factors envelope, which is observed for low EO, disappears, giving a more “disordered” trend with very different magnification factors from one blade to another one.

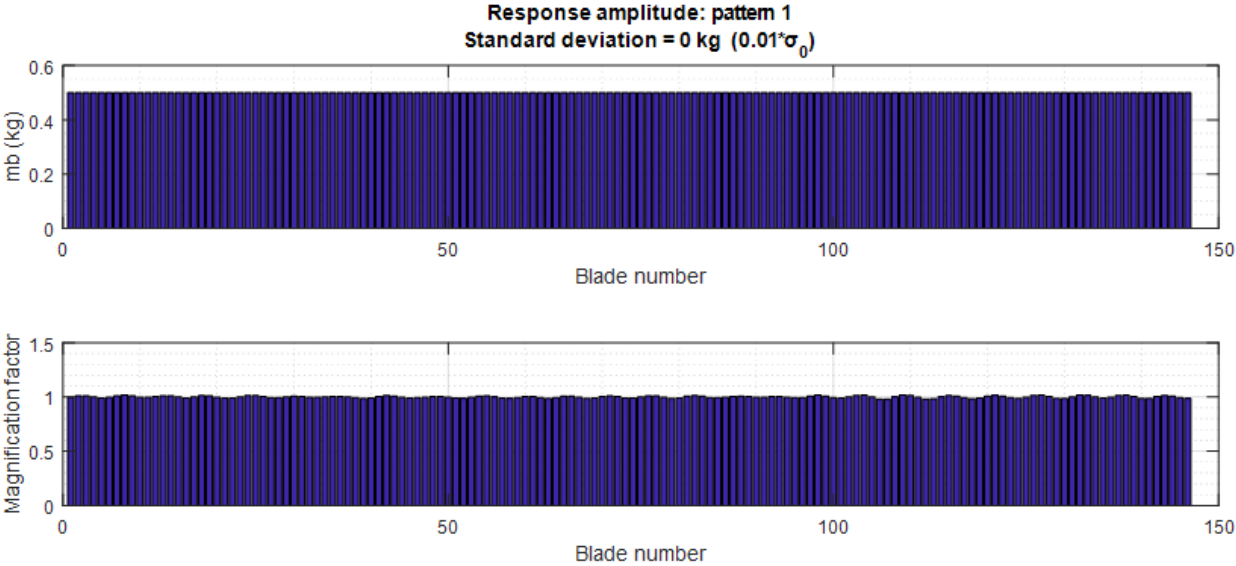


Figure 3.7a. Magnification factors and mass distribution ( $a_p = 0.01$  ; EO = 60).

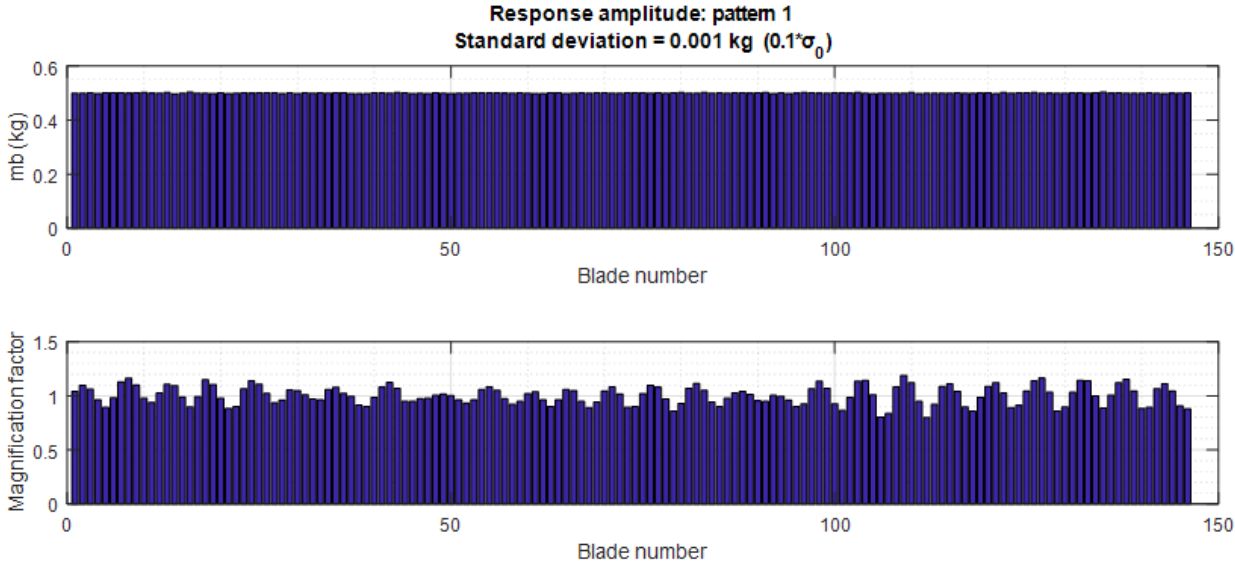


Figure 3.7b. Magnification factors and mass distribution ( $a_p = 0.1$  ; EO = 60).

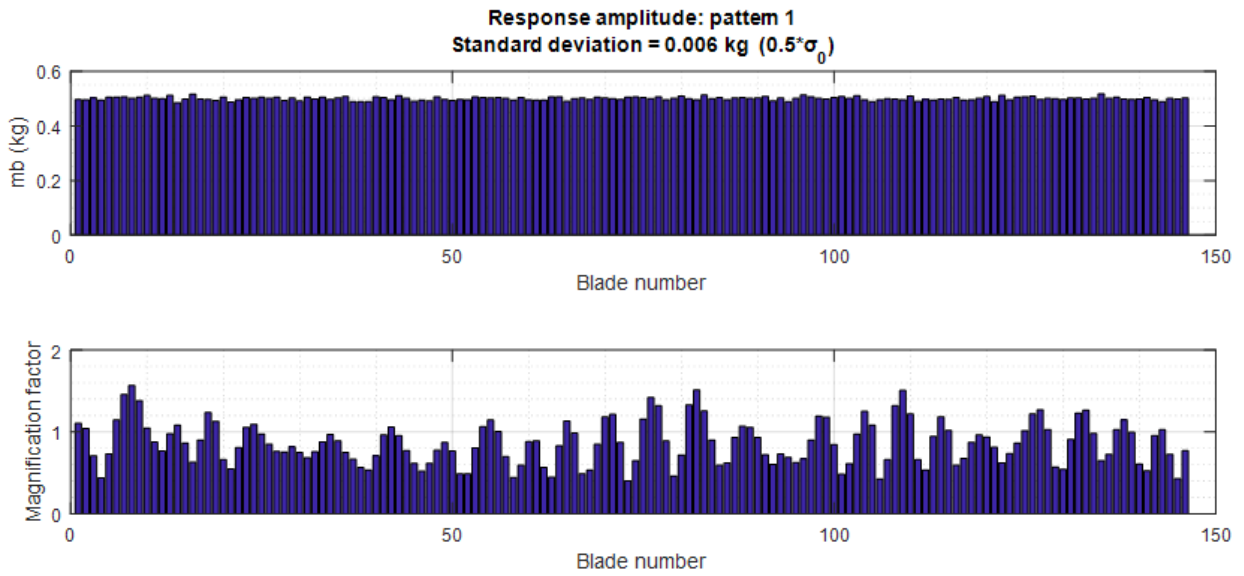


Figure 3.7c. Magnification factors and mass distribution ( $a_p = 0.5$  ; EO = 60).

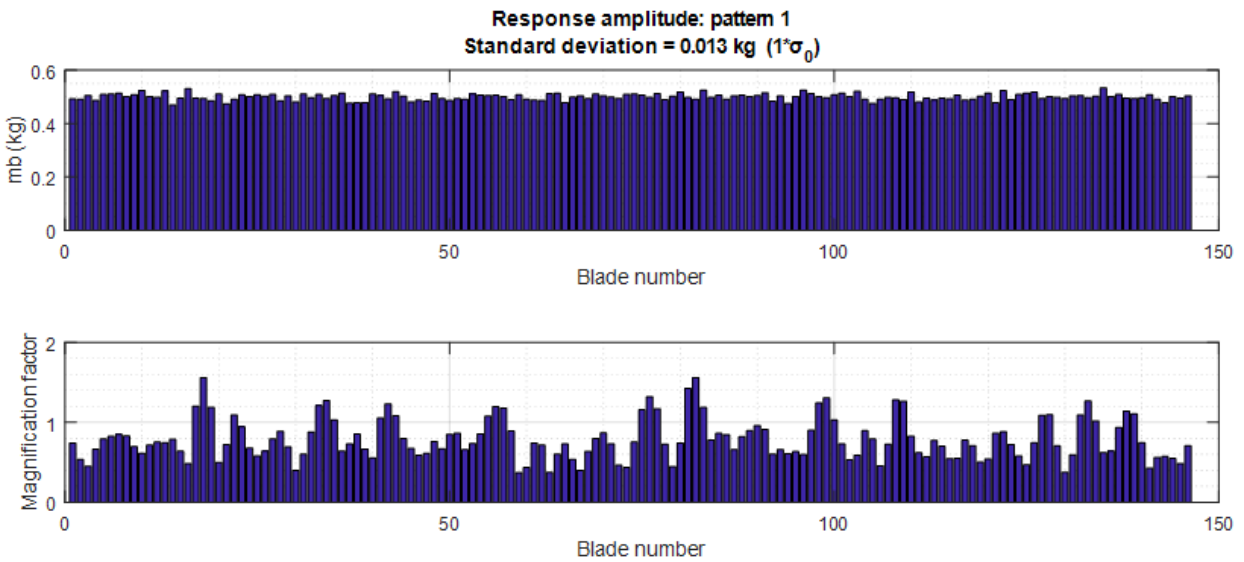


Figure 3.7d. Magnification factors and mass distribution ( $a_p = 1$  ; EO = 60).

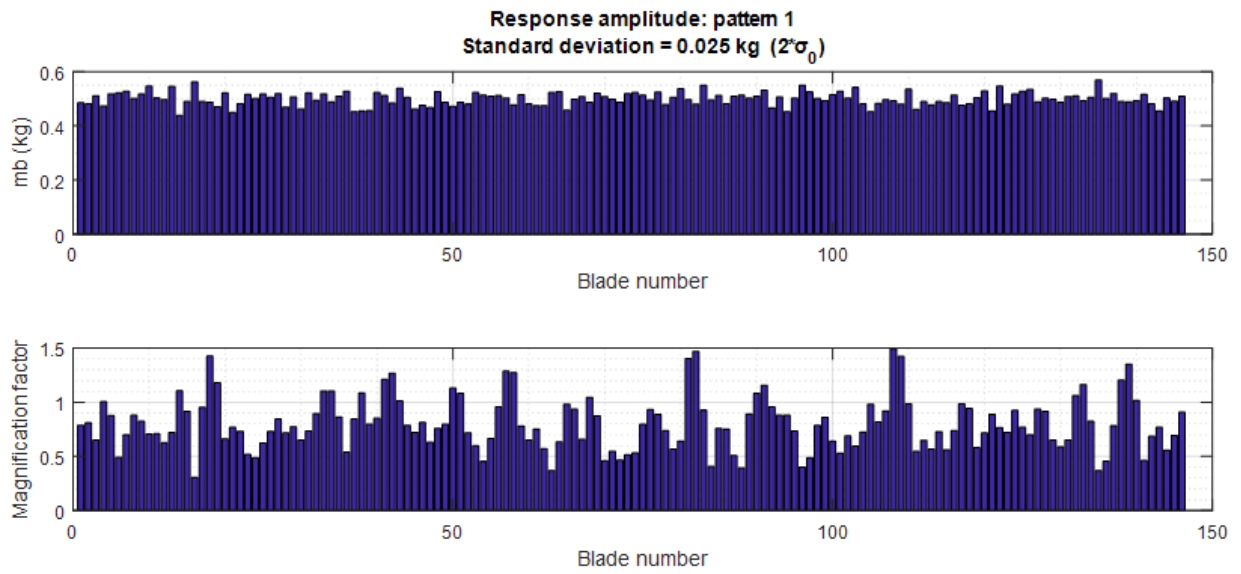


Figure 3.7e. Magnification factors and mass distribution ( $a_p = 2$  ; EO = 60).

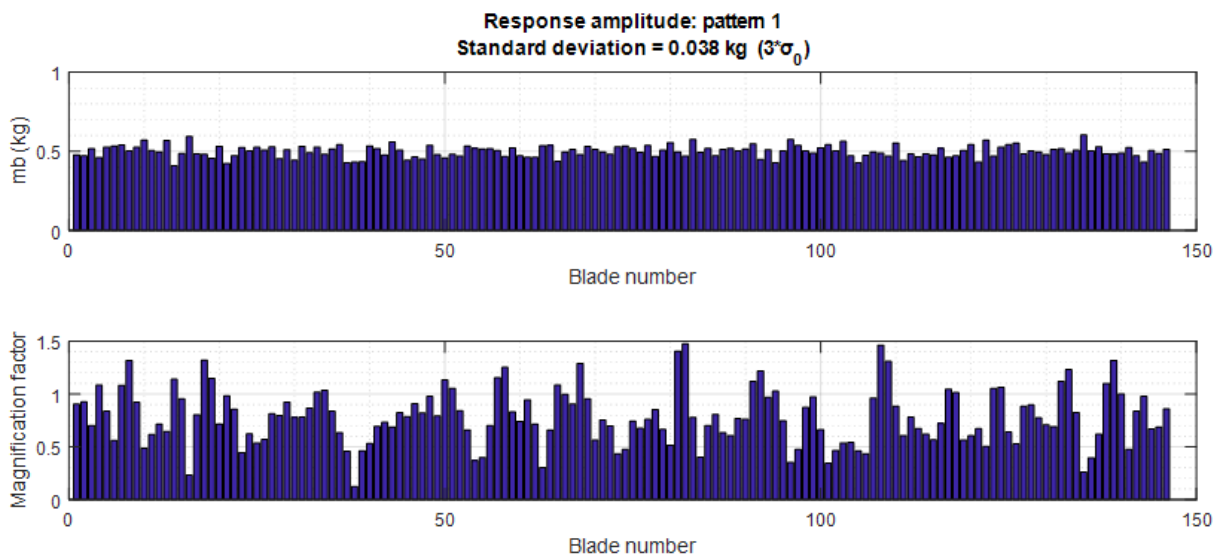


Figure 3.7f. Magnification factors and mass distribution ( $a_p = 3$  ; EO = 60).

## 3.4 Mistuning identification

### 3.4.1 Modeling of the bladed disk with joints incorporation

The identification of mistuning has a primary role in the study of a bladed disk dynamics. As a matter of fact, mistuning cannot be controlled a priori because it is linked to the non symmetry of the structure which can be induced by several factors. One of the major causes of mistuning is represented by the joints of the blades. They can affect drastically the behavior of the whole structure during the application because of the uncertainty linked to the assembly operations. Here, joint elements, constituted by a stiffness and a damper, are introduced into the lumped parameters model of the bladed disk, between the blades degrees of freedom and the corresponding disk degrees of freedom. The aim of the study is to induce mistuning by providing a set of joint stiffness affected by a random error with known standard deviation and to provide a method of identification of the amount of mistuning, starting from the FRF of the mistuned disk. In order to compute the study, the FRF Decoupling Method is adopted. This method is based on the use of substructures (without joints) , whose FRF are known or easy to be computed, and the FRF of the assembled structure which is known from testing. The method allows the study of the mechanical properties of the joints connecting the substructures with each other. The need to develop such methods is due to the fact that a modeling of the joint is difficult to be done because of its complexity. Many FRF Decoupling methods are proposed in literature [13-17]. Before going through the FRF Decoupling, a new model of the bladed disk has to be built, in order to introduce the joint elements. A representation of the model is showed in figure 3.8. The joint element is described by the stiffness  $k_j$  and damping  $c_j$ . In order to properly identify the joint elements another degree of freedom is added to the blade model, with respect to the model previously used (figure 1.3). The other mechanical properties of mass and stiffness which describe the disk and the blade are maintained the same of those used before, in the model of the bladed disk without joints, and they are  $m_d$ ,  $m_b$ ,  $k_d$ ,  $k_c$  and  $k_b$ . Since the blade is now modeled with two degrees of freedom, the mass  $m_b$  (used in the previous model) is divided by two and the two halves are associated to the degrees of freedom of blade. Here the damping matrix is derived by introducing viscous damper between the degrees of freedom together with the stiffness elements, unlike the 2N dof model used before where the damping matrix is derived through the modal matrix by setting a modal damping ratio to the modes. They are respectively  $c_d$ ,  $c_c$  and  $c_b$ .

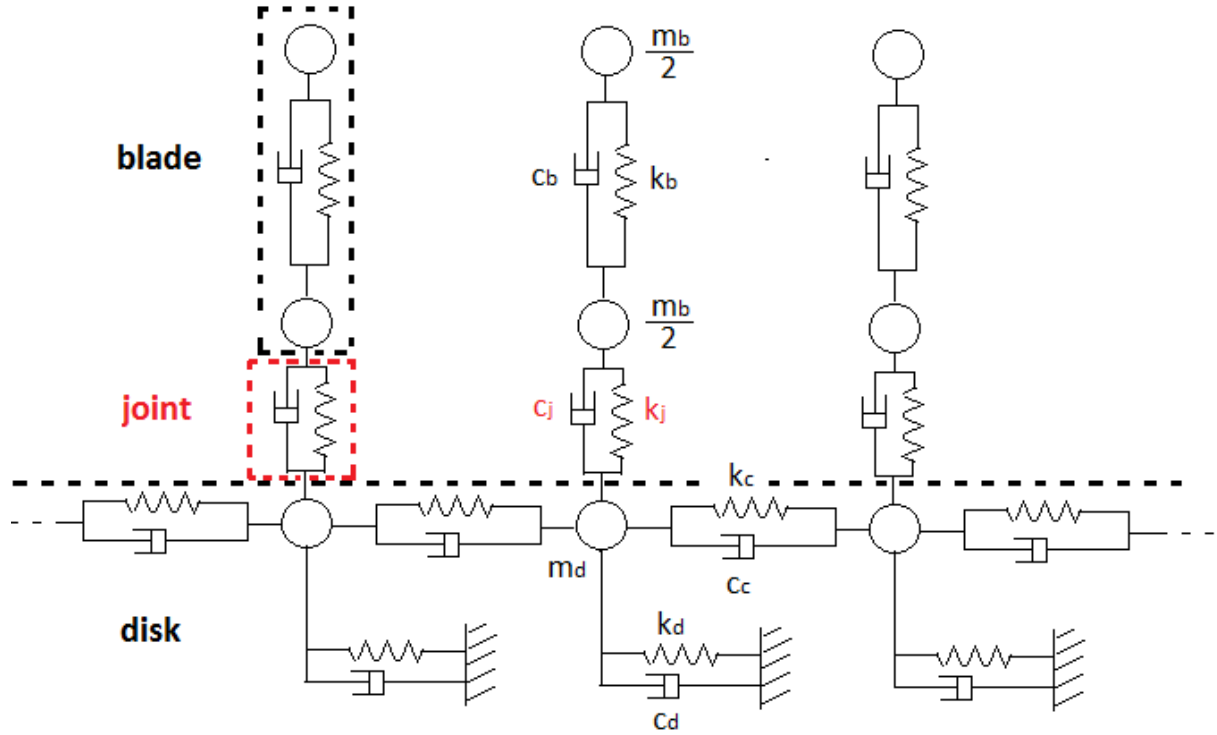


Figure 3.8. Model of the bladed disk with joints.

Then, the new model is constituted by  $3N$  degrees of freedom, where the first  $N$  degrees of freedom describe the disk while the other  $2N$  degrees of freedom describe the  $N$  blades, which are modeled with two degrees of freedom. The general equation of motion in matrix form is written in equation (3.3). The mass, damping and stiffness matrices, of dimension  $3N \times 3N$ , are derived from the free body diagram analysis (Appendix 4), while the set of coordinates  $\{x\}$  is a  $3N \times 1$  vector where the degrees of freedom are organized in the order showed by equation (3.4).

$$[M]\{\ddot{x}\} + [C]\{\dot{x}\} + [K]\{x\} = \{F\} \quad (3.3)$$

$$\{x\} = \left\{ \{x_{disk}\}_{N \times 1}, \{x_{blade\ root}\}_{N \times 1}, \{x_{blade\ tip}\}_{N \times 1} \right\}^T \quad (3.4)$$

By considering the bladed disk to be tuned, at this stage, with joints having all the same stiffness and damping characteristic  $k_j$  and  $c_j$ , the FRF  $[H]$  of the whole structure, expressed as a receptance, can be computed from the inversion of the dynamic stiffness matrix (3.5), once a frequency range is set.

$$[H] = [K_{dyn}]^{-1} = [K - \omega^2 M + i\omega C]^{-1} \quad (3.5)$$

Now, mistuning is applied to the joint stiffness  $k_j$ . So a pattern of mistuned stiffness is generated from a normal distribution with known standard deviation  $\sigma_0$  and mean value equal to the nominal stiffness  $k_{j,n}$  ( $k_{j,n} = 5E7$  N/m, in the numerical example). The probability density function of such a distribution is showed in figure 3.9. Then, a set of amplification coefficients  $a_p$  can be applied to the pattern in order to amplify the amount of mistuning. The set of amplification coefficients is reported on the table 3.2.

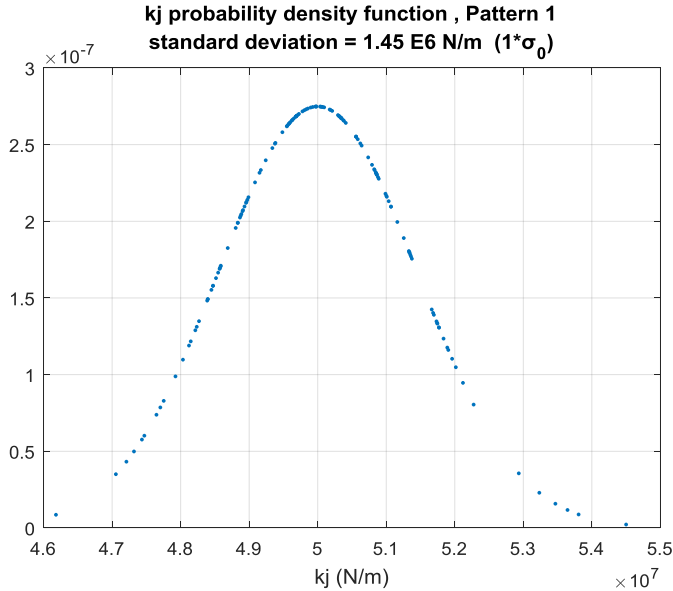


Figure 3.9. Probability density function of  $k_j$ .

Standard deviation $\sigma_p$ (N/m)			
$a_p$	1	2	4
$\sigma_p$ (N/m)	1,45E+06	2,90E+06	5,80E+06

Table 3.2. Standard deviations of the amplified mistuning pattern.

For each amplification coefficient  $a_p$ , a set of  $N$  stiffness  $k_j$  can be derived from the starting pattern. As a consequence, a number  $p$  of stiffness matrices  $[K_{mis}]$  can be built. By maintaining the same mass matrix and damping matrix of the tuned case, it is possible to get the receptance matrix  $[H_{mis}]$  of the whole structure, per each amplification coefficient applied to the pattern, by inverting the dynamic stiffness matrix. The receptance matrix is needed to apply the FRF Decoupling Method. It has to be noted that these FRFs, which are now computed numerically by building a model of the whole structure, represent the FRFs that are acquired experimentally by testing the whole structure which bring, in a real case, the unknown quantities of the equivalent stiffness and damping of the joints.

### 3.4.2 FRF Decoupling Method

The FRF Decoupling Method is an FRF-based method which was developed to face the problems linked to the identification of the mechanical properties of a coupling connecting two or more substructures. The need for developing such a method is given by the fact that a modeling of a joint cannot be easy to be done. Usually joints or interfaces in general have complex configurations and geometries so to make the modeling very difficult. Then, a reverse method which makes use of experimental data has to be studied in order to get the equivalent mechanical properties connected to a joint. In this paragraph the FRF Decoupling Method is described. The method assumes to have an assembly which is constituted by two substructures A and B. The FRF of the two substructures (without joints),  $[H_A]$  and  $[H_B]$  are considered as known. Then, the assembly (with joints) is tested and the FRF  $[H_c]$  is derived experimentally. The degrees of freedom of each substructure are divided into two groups in order to distinguish between the degrees of freedom which are at the interface with the joint from the others. The dofs of substructure A that are at the interface are named “j” while the others are named “a”. The dofs of substructure B that belong to the interface are named “k” while the other dofs are named “b” (see figure 3.10).

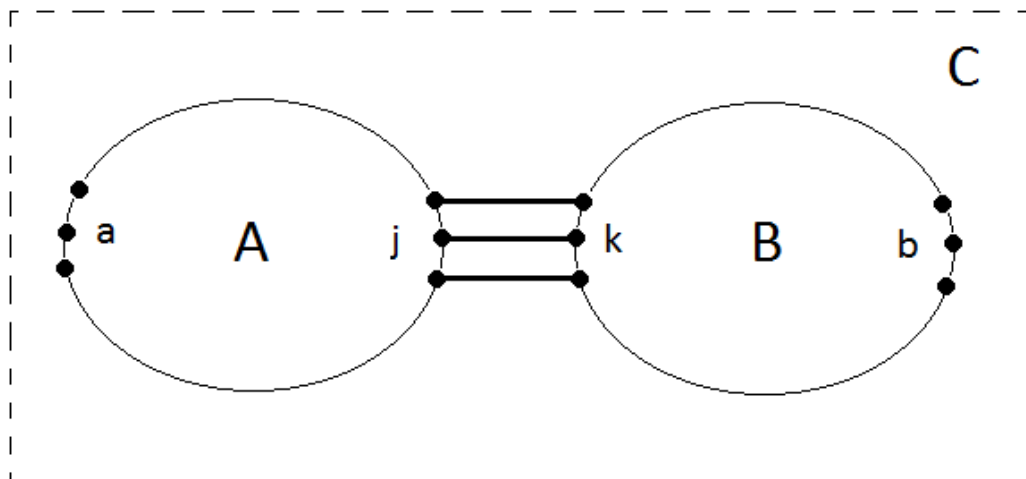


Figure 3.10, Scheme of substructures in the FRF Decoupling Method.

The displacement coordinates of the two substructures are respectively  $\{x_A\}$ , and  $\{x_B\}$  (3.6). They can be expressed as the product between the receptance matrix and the forcing function vector applied to each substructure (3.7).

$$\{x_A\} = \{ \{x_a\}, \{x_j\} \}^T \quad (3.6a)$$

$$\{x_B\} = \{ \{x_k\}, \{x_b\} \}^T \quad (3.6b)$$

$$\{x_A\} = [H_A]\{f_A\} = \begin{bmatrix} [H_{aa}] & [H_{aj}] \\ [H_{ja}] & [H_{jj}] \end{bmatrix} \begin{Bmatrix} \{f_a\} \\ \{f_j\} \end{Bmatrix} \quad (3.7a)$$

$$\{x_B\} = [H_A]\{f_A\} = \begin{bmatrix} [H_{kk}] & [H_{kb}] \\ [H_{bk}] & [H_{bb}] \end{bmatrix} \begin{Bmatrix} \{f_k\} \\ \{f_b\} \end{Bmatrix} \quad (3.7b)$$

From the equations (3.7) the displacements can be written in an explicit form by computing the product between the receptance matrix and the forcing vector (3.8).

$$\{x_a\} = [H_{aa}]\{f_a\} + [H_{aj}]\{f_j\} \quad (3.8a)$$

$$\{x_j\} = [H_{ja}]\{f_a\} + [H_{jj}]\{f_j\} \quad (3.8b)$$

$$\{x_k\} = [H_{kk}]\{f_k\} + [H_{kb}]\{f_b\} \quad (3.8c)$$

$$\{x_b\} = [H_{bk}]\{f_k\} + [H_{bb}]\{f_b\} \quad (3.8d)$$

Once the displacements have been derived, the equilibrium equations at the joint, which is considered as an elastic coupling, have to be written. In order to have the equilibrium, the sum of the external forces applied to the joint has to be equal to zero (3.9).

$$\{f_j\} + \{f_k\} = \{0\} \quad (3.9)$$

As a consequence, the force  $\{f_k\} = -\{f_j\}$  is equal to the elastic force of the coupling which is given by introducing the coupling matrix  $[Z_c]$  which describes its mechanical properties and represents the unknown of the method (3.10). This matrix is complex because of the damping force contribution which enters the equilibrium equation. By substituting the expressions of  $\{x_j\}$  and  $\{x_k\}$ , respectively (3.8b) and (3.8c), into the equation (3.10) one obtains the equation (3.11).

$$[Z_c](\{x_j\} - \{x_k\}) = \{f_k\} \quad (3.10)$$

$$[H_{ja}]\{f_a\} - ([H_{jj}] + [H_{kk}])\{f_k\} + [H_{kb}]\{f_b\} = [Z_c]^{-1}\{f_k\} \quad (3.11)$$

An analogue discussion is made on the structure considered as a whole (structure C). In that case the coupling is not considered as an external object. It is incorporated into the structure, so no distinction is made on the dofs “j” and “k”. In the whole structure configuration the degrees of freedom which are considered (and that can be tested) are the dofs “a” and dofs “b”. From this consideration it is possible to write the displacement coordinates of the dofs taken into account as the product of a receptance matrix of the whole structure and the forcing vector (3.12), like in the substructure configuration.

$$\{x_c\} = \begin{Bmatrix} \{x_a\} \\ \{x_b\} \end{Bmatrix} = [H_c]\{f_c\} = \begin{bmatrix} [H_{aa}^c] & [H_{ab}^c] \\ [H_{ba}^c] & [H_{bb}^c] \end{bmatrix} \begin{Bmatrix} \{f_a\} \\ \{f_b\} \end{Bmatrix} \quad (3.12)$$

The matrix equation (3.12) can be developed in order to obtain the equations for the two sets of coordinate  $\{x_a\}$  and  $\{x_b\}$  (3.13).

$$\{x_a\} = [H_{aa}^c]\{f_a\} + [H_{ab}^c]\{f_b\} \quad (3.13a)$$

$$\{x_b\} = [H_{ba}^c]\{f_a\} + [H_{bb}^c]\{f_b\} \quad (3.13b)$$

Now, the equations derived from the two studies ( one related to the two substructures A and B connected by the coupling and the other study considering the whole structure C ) can be combined in order to express the coupling matrix as a function of the other terms. In particular it is possible to combine the equations (3.13a) and (3.13b) with equation (3.11) which brings the unknown  $[Z_c]$ , in order to obtain the expressions of the sub-matrices which constitute the receptance matrix of the whole structure C (3.14).

$$[H_{aa}^c] = [H_{aa}] - [H_{aj}] \left( [H_{jj}] + [H_{kk}] + [Z_c]^{-1} \right)^{-1} [H_{ja}] \quad (3.14a)$$

$$[H_{bb}^c] = [H_{bb}] - [H_{bk}] \left( [H_{jj}] + [H_{kk}] + [Z_c]^{-1} \right)^{-1} [H_{kb}] \quad (3.14b)$$

$$[H_{ab}^c] = [H_{aj}] \left( [H_{jj}] + [H_{kk}] + [Z_c]^{-1} \right)^{-1} [H_{kb}] \quad (3.14c)$$

$$[H_{ba}^c] = [H_{bk}] \left( [H_{jj}] + [H_{kk}] + [Z_c]^{-1} \right)^{-1} [H_{ja}] \quad (3.14d)$$

This set of equations can be further developed in order to obtain the expression of the matrix  $[Z_c]$  as a function of the other terms (3.15).

$$[Z_c] = \left[ [H_{ja}] \left( [H_{aa}] - [H_{aa}^c] \right)^{-1} [H_{aj}] - [H_{jj}] - [H_{kk}] \right]^{-1} \quad (3.15a)$$

$$[Z_c] = \left[ [H_{kb}] \left( [H_{bb}] - [H_{bb}^c] \right)^{-1} [H_{bk}] - [H_{jj}] - [H_{kk}] \right]^{-1} \quad (3.15b)$$

$$[Z_c] = \left[ [H_{ja}] [H_{ba}^c]^{-1} [H_{bk}] - [H_{jj}] - [H_{kk}] \right]^{-1} \quad (3.15c)$$

$$[Z_c] = \left[ [H_{kb}] [H_{ab}^c]^{-1} [H_{aj}] - [H_{jj}] - [H_{kk}] \right]^{-1} \quad (3.15d)$$

The equations (3.15) are equivalent with each other. One can decide to use an equation rather than another one. It depends on the type of receptance matrix which has been derived from testing on the structure C ( $[H_{aa}^C]$ ,  $[H_{bb}^C]$ ,  $[H_{ba}^C]$  or  $[H_{ab}^C]$ ). The receptance matrices which refer to the substructures A and B are meant to be known. The elements of the coupling matrix  $[Z_c]$  are complex. By modeling the joint element with a stiffness and a damper in parallel it is possible to give a physical meaning to the elements of that matrix. In more detail, the element of the coupling matrix,  $z_{jk}$  is given by the equation (3.16), where  $k_{jk}$  is a stiffness quantity and  $c_{jk}$  is a viscous damping quantity.

$$z_{jk} = k_{jk} + i \omega c_{jk} \quad (3.16)$$

### 3.4.3 Use of FRF Decoupling for mistuning identification

The aim of the study is to apply the FRF Decoupling Method to analyze the mechanical characteristics of the joints of the bladed disk and to evaluate the amount of mistuning connected to these characteristics. Then, in the following discussion the FRF Decoupling method is adapted to the case of study and it is used to derive the characteristics of the joints in different mistuning conditions. The substructures in which the bladed disk can be divided are the disk and the N blades coupled with the disk. This leads to have N joints to be identified at the same time. So, the FRF Decoupling Method, as it was described in the previous paragraph, has to be adapted to the multiple-joints configuration represented by the bladed disk. In order to do this, one has to write the equilibrium equations by following the same procedure used for the case of single-joint configuration. The degrees of freedom which are now involved are the ones reported in equation (3.4). These coordinates will be called with other subscripts in order to maintain a coherence with the nomenclature used in the theory description of the FRF Decoupling Method ( previous paragraph ). In particular, the coordinates  $\{x_{disk}\}_{N \times 1}$ , which constitute the disk and are connected to the joints, are associated with the coordinates  $\{x_j\}$  (used in the theory of the method). The coordinates  $\{x_{blade\ root}\}_{N \times 1}$ , which represents the interface dofs of the blades with the joints, are identified with the coordinates  $\{x_k\}$  of the method. The coordinates  $\{x_{blade\ tip}\}_{N \times 1}$ , corresponding to the dofs of the blades where the excitation forces are applied and where the FRF is computed, are associated with the coordinates  $\{x_b\}$  of the method. By referring to the model in figure 3.8, one can imagine to cut at the two interfaces of each joint, obtaining the substructures of the disk and of the N blades. The cut leads to the definition of a force  $S$  at the interfaces of the disk and the blades with the joint elements, for the equilibrium of the forces. This is represented in figure 3.11. Then, the expression of the displacement coordinates  $\{x_j\}$ ,  $\{x_k\}$  and  $\{x_b\}$  are written in terms of receptance times force contributions summation (3.17, 3.18, 3.21).

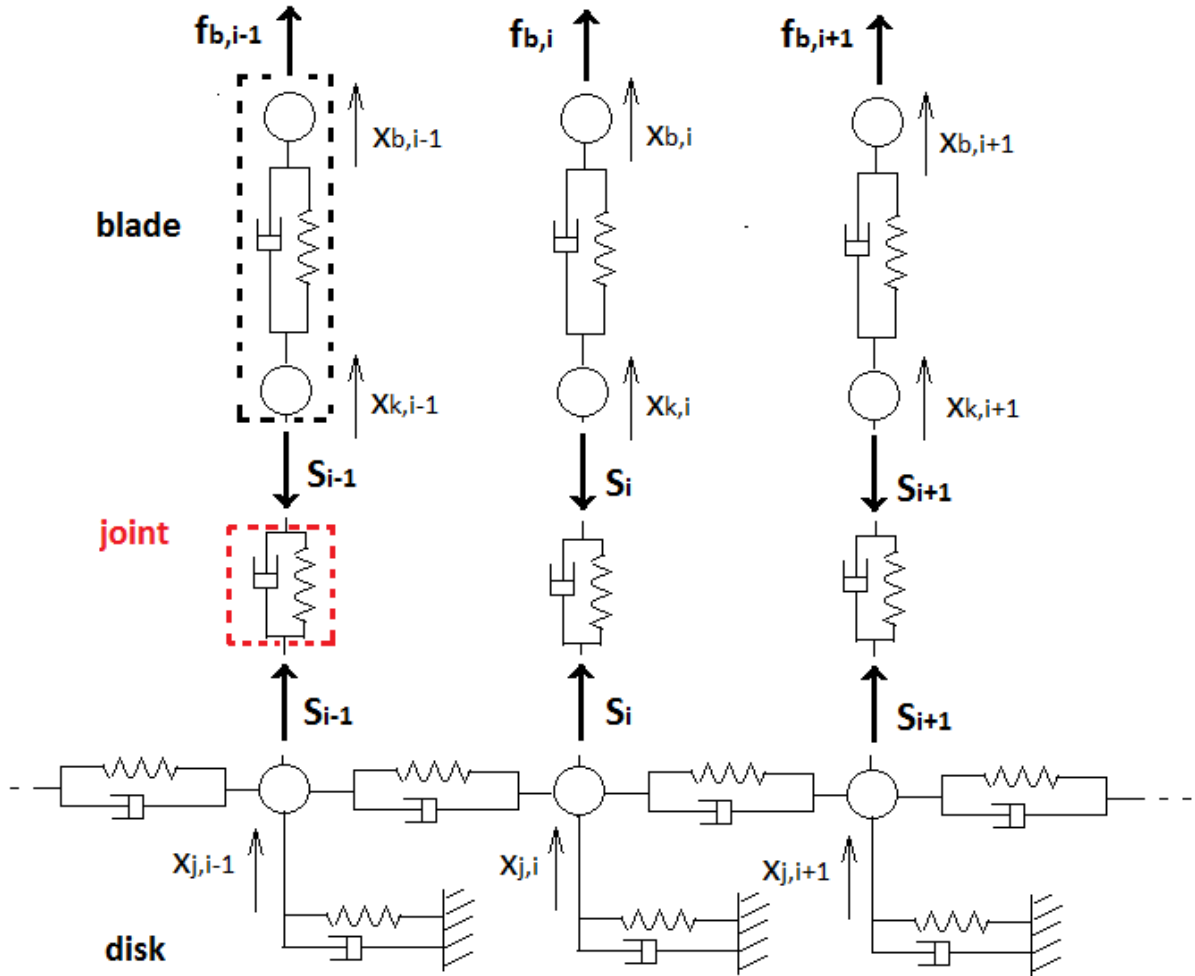


Figure 3.11. Sub-structuring of the bladed disk with joints.

Displacement coordinates  $\{x_j\}$ ,  $(i = 1, \dots, N)$  :

$$\begin{cases} x_{j,1} = H_{11}^{disk} S_1 + \dots + H_{1i}^{disk} S_i + \dots + H_{1N}^{disk} S_N \\ \vdots \\ x_{j,i} = H_{i1}^{disk} S_1 + \dots + H_{ii}^{disk} S_i + \dots + H_{iN}^{disk} S_N \\ \vdots \\ x_{j,N} = H_{N1}^{disk} S_1 + \dots + H_{Ni}^{disk} S_i + \dots + H_{NN}^{disk} S_N \end{cases} \quad (3.17a)$$

Expressing the system of equations in a matrix form one obtains that the coordinates vector  $\{x_j\}$  is equal to the receptance matrix of the substructure “disk”,  $[H_{jj}]$ , times the vector of forces  $\{S\}$  (3.17b).

$$\{x_j\} = [H_{jj}]\{S\} \quad (3.17b)$$

Displacement coordinates  $\{x_k\}$ , ( $i = 1, \dots, N$ ) :

$$\begin{cases} x_{k1} = H_{12}^{blade\ 1} f_{b1} - H_{11}^{blade\ 1} S_1 \\ \vdots \\ x_{ki} = H_{12}^{blade\ i} f_{bi} - H_{11}^{blade\ i} S_i \\ \vdots \\ x_{kN} = H_{12}^{blade\ N} f_{bN} - H_{11}^{blade\ N} S_N \end{cases} \quad (3.18a)$$

where  $[H^{blade\ i}]$  is the receptance of the substructure “blade” (3.18b) with degrees of freedom  $\{x_k, x_b\}^T$ . Each blade has an its own receptance matrix which can be different from that of another blade. However, in this specific example, the blades are considered to be all equal, with known receptance matrix, and it is assumed to mistune the joints stiffness only. The system (3.18a) written in matrix form becomes (3.18c), where the matrices which multiply the force vectors  $\{f_b\}$  and  $\{S\}$  are diagonal ( since equations are all independent with each other ) and correspond to the matrices  $[H_{kb}]$  and  $[H_{kk}]$  of the method.

$$[H^{blade\ i}] = \begin{bmatrix} H_{11}^{blade} & H_{12}^{blade} \\ H_{21}^{blade} & H_{22}^{blade} \end{bmatrix} \quad \forall i \quad (3.18b)$$

$$\{x_k\} = \begin{bmatrix} \ddots & 0 & 0 \\ 0 & H_{12}^{blade} & 0 \\ 0 & 0 & \ddots \end{bmatrix} \{f_b\} - \begin{bmatrix} \ddots & 0 & 0 \\ 0 & H_{11}^{blade} & 0 \\ 0 & 0 & \ddots \end{bmatrix} \{S\} = [H_{kb}]\{f_b\} - [H_{kk}]\{S\} \quad (3.18c)$$

At this stage, the equilibrium of the forces at the joint elements can be studied. By referring to equation (3.10), the force  $S_i$  (correspondent to the  $i$ -th blade) is connected to the difference between the displacements of the joint interfaces through the coupling (complex) stiffness  $Z_i$ . By writing the same equation for all the  $N$  joints, one obtains (3.19), where  $[Z_c]$  is a diagonal matrix.

$$[Z_c](\{x_j\} - \{x_k\}) = \begin{bmatrix} \ddots & 0 & 0 \\ 0 & Z_i & 0 \\ 0 & 0 & \ddots \end{bmatrix} (\{x_j\} - \{x_k\}) = \{S\} \quad (3.19)$$

By substituting (3.17b) and (3.18c) into (3.19) it follows:

$$[H_{kb}]\{f_b\} = ([H_{jj}] + [H_{kk}] + [Z_c]^{-1})\{S\} \quad (3.20)$$

Finally, the coordinates  $\{x_b\}$  has to be defined (3.21a). As for the coordinates  $\{x_k\}$ , the equations are all independent with each other, so the equation in matrix form is expressed by diagonal matrices (3.21b). These matrices correspond to the  $[H_{bb}]$  and  $[H_{bk}]$  of the method.

$$\begin{cases} x_{b1} = H_{22}^{blade} f_{b1} - H_{21}^{blade} S_1 \\ \vdots \\ x_{bi} = H_{22}^{blade} f_{bi} - H_{21}^{blade} S_i \\ \vdots \\ x_{bN} = H_{22}^{blade} f_{bN} - H_{21}^{blade} S_N \end{cases} \quad (3.21a)$$

$$\{x_b\} = \begin{bmatrix} \ddots & 0 & 0 \\ 0 & H_{22}^{blade} & 0 \\ 0 & 0 & \ddots \end{bmatrix} \{f_b\} - \begin{bmatrix} \ddots & 0 & 0 \\ 0 & H_{21}^{blade} & 0 \\ 0 & 0 & \ddots \end{bmatrix} \{S\} = [H_{bb}]\{f_b\} - [H_{bk}]\{S\} \quad (3.21b)$$

By substituting equation (3.20) into (3.21b) one obtains:

$$\{x_b\} = \left[ [H_{bb}] - [H_{bk}] \left( [H_{jj}] + [H_{kk}] + [Z_c]^{-1} \right)^{-1} \right] \{f_b\} \quad (3.22)$$

Since  $\{x_b\}$  is the response of the blades in the measuring points and  $\{f_b\}$  is the forcing function vector, the transfer matrix of the equation (3.22) is exactly the receptance sub-matrix  $[H_{bb}^C]$  (3.12) of the whole structure, related to  $\{x_b\}$ , and it is built from testing. Then, it follows:

$$[H_{bb}^C] = [H_{bb}] - [H_{bk}] \left( [H_{jj}] + [H_{kk}] + [Z_c]^{-1} \right)^{-1} \quad (3.23)$$

From this equation, which has the same form of the one obtained in the previous paragraph where the single-joint configuration was analyzed (3.14b), it is possible to derive the coupling matrix  $[Z_c]$  (3.24), which contains the complex “stiffness” of the joints in its diagonal.

$$[Z_c] = \left[ [H_{kb}] \left( [H_{bb}] - [H_{bb}^C] \right)^{-1} [H_{bk}] - [H_{jj}] - [H_{kk}] \right]^{-1} \quad (3.24)$$

where  $[H_{kb}]$ ,  $[H_{bb}]$ ,  $[H_{bk}]$  and  $[H_{kk}]$  are diagonal matrices and they are constituted by elements of the receptance matrix of the blade,  $[H_{jj}]$  is the receptance matrix of the disk while  $[H_{bb}^C]$  is the experimental receptance matrix (FRF) which is derived from testing. The FRF Decoupling method was used for the specific case of study, where a pattern of mistuned  $k_j$  was assigned to the N joints of the bladed disk and it was then amplified by using amplification coefficients equal to 2 and 4 (paragraph 3.4.1). The results coming from the application of the method are very accurate and they allows to state with a great precision the mechanical properties of the joint elements. In the numerical example, starting from a nominal value of  $k_{j,n} = 5E7 \text{ N/m}$ , a mistuned set of  $k_j$  was derived, per each amplification coefficient adopted. The results are showed in figures 3.12. From the figures it is clear that the method is very accurate since the two plotted sets of stiffness (the real one and the one derived by means of the FRF method) can be perfectly overlapped.

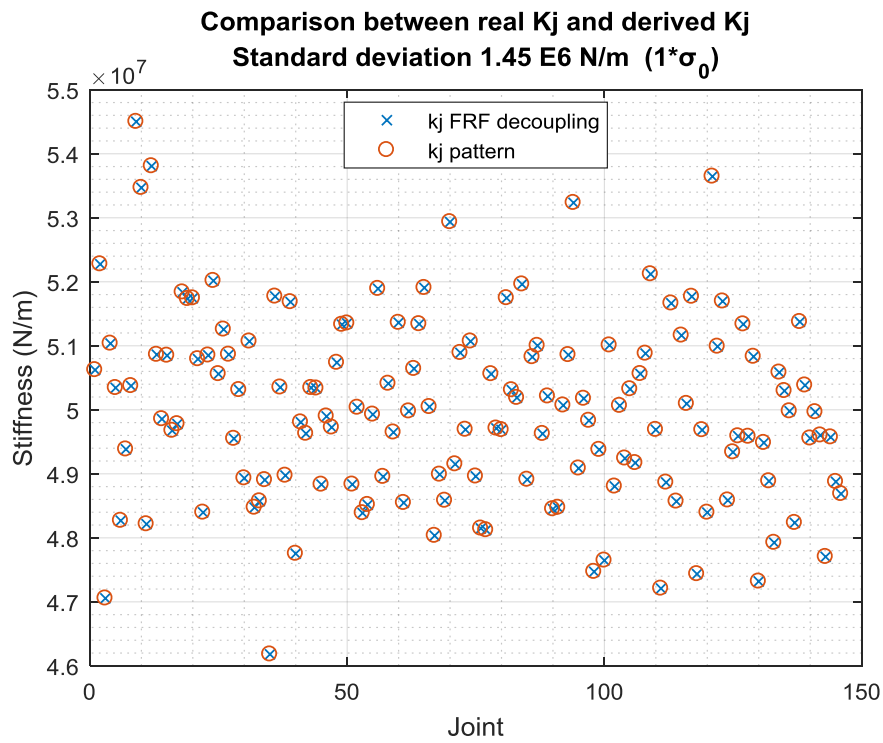


Figure 3.12a. Comparison between real  $k_j$  and derived  $k_j$ :  $a_p = 1$ .

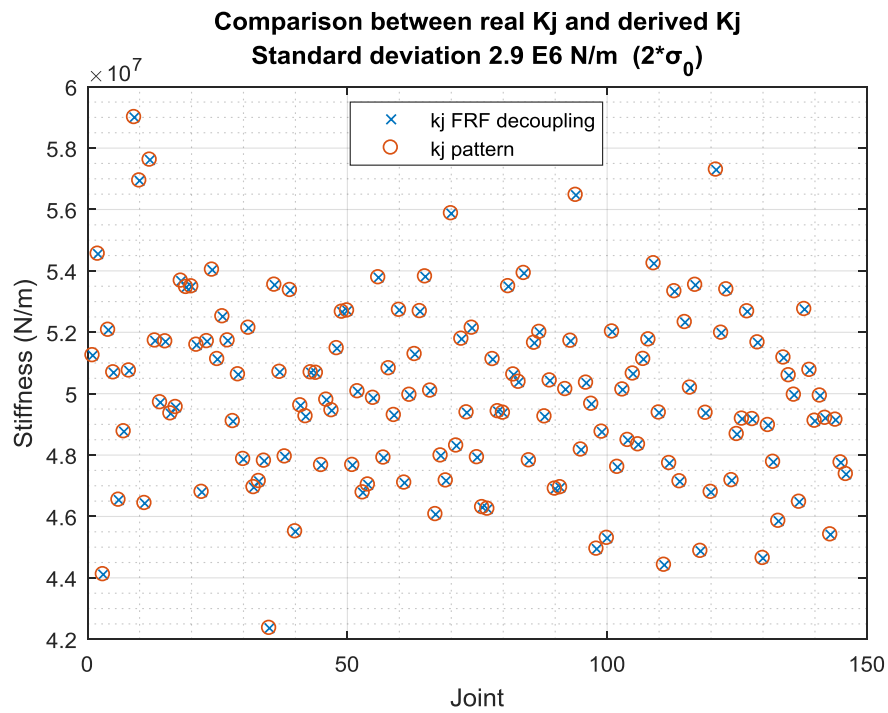


Figure 3.12a. Comparison between real  $k_j$  and derived  $k_j$ :  $a_p = 2$ .

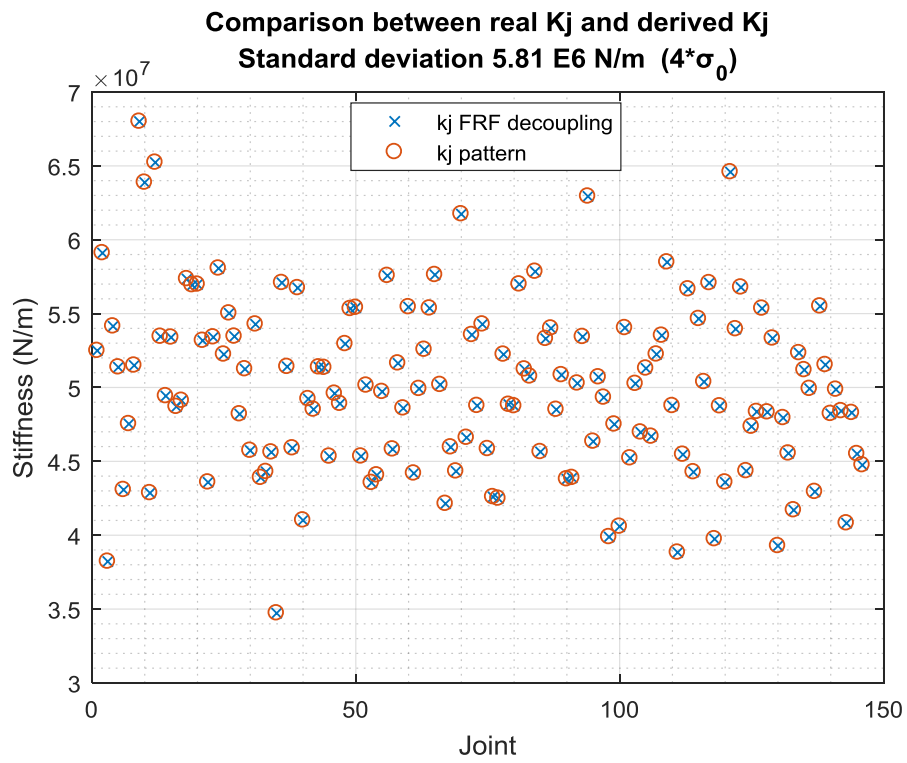


Figure 3.12a. Comparison between real  $k_j$  and derived  $k_j$ :  $a_p = 4$ .

# Chapter 4

## Friction-damped response analysis

In turbine bladed disk applications, the need to damp the vibration of the blades in resonance conditions has become more and more demanding in order to reach very high performances in the rotational speed of the turbine. As a matter of fact, the structural damping alone is not able to ensure low amplitude vibrations. Then, new constructional solutions have been studied in order to add damping to the structure. One of the possible solutions is to provide a sliding friction between the parts of the system so to induce a damping effect in working conditions. The dependence of the friction force on the motion of the structure itself makes the system non-linear. Then, a reduction of the number of degrees of freedom involved is needed in order to solve easily the non-linear system of equations. Here, the reduction of the problem is made by exploiting the property of cyclic symmetry which allows to write a system with few non-linear equations. According to the design of the bladed disk, the dynamics of the system can be studied by following different approaches and models. The aim of this chapter is to analyze different models which describe how friction is provided within the system and to compute the forced response under the aforementioned conditions.

### 4.1 Bladed disk with blade-to-ground friction dampers

The most simple solution to be studied is to provide devices which behaves as *blade-to-ground dampers*. A blade-to-ground damper is a device which acts at the blade level and it induces sliding friction between the blade body and a fixed reference (ground). Before analyzing the model to be used to compute the forced response, a detailed study on the nature of the friction force has to be done. In order to study how the friction force enters the equations of motion it is useful to consider a single degree of freedom system where a blade-to-ground damper is introduced (figure 4.1).

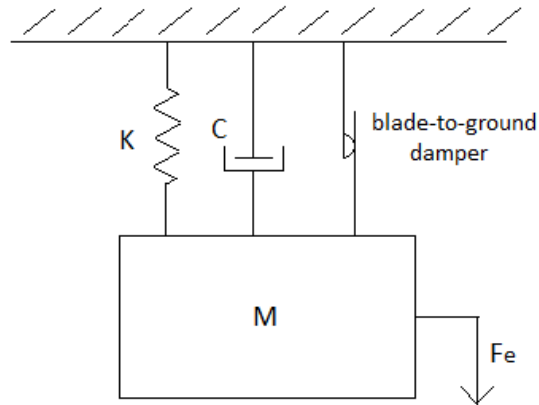


Figure 4.1. Single degree of freedom system with blade-to-ground damper.

The damper induces a friction force, expressed in the equation (4.1), which is proportional to the preload of the damper through a dynamic friction coefficient and it is opposite in the sign to the speed of the mass. By looking at the free body diagram of the mass in figure 4.2, the friction force has been already oriented in the opposite direction with respect to the speed  $\dot{x}$ . This allows to avoid the “minus” sign in the expression of the friction force.

$$F_{\mu} = \mu_d F_N \text{sign}(\dot{x}) \quad (4.1)$$

where

- $F_{\mu}$ , friction force.
- $\mu_d$ , dynamic friction coefficient.
- $F_N$ , preload.
- $\dot{x}$ , speed.

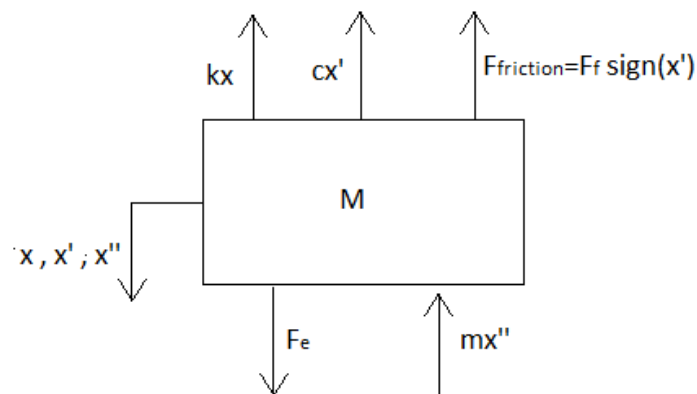


Figure 4.2. Free body diagram of the sdof system with blade-to-ground damper.

The friction force  $F_\mu$  can be written in a different way by transforming the “sign” function, as it is showed in the equation (4.2). By considering a generic variable  $y$ , the function  $\frac{y}{|y|}$  can be expanded in Fourier series (4.3). The Fourier series can be developed in order to obtain a series of cosine functions, that represent the useful form for the following discussion, and substituted into the expression of the friction force (4.2) obtaining the expression (4.4).

$$F_\mu = \mu_d F_N \frac{\dot{x}}{|\dot{x}|} \quad (4.2)$$

$$\mathcal{F}\left(\frac{y}{|y|}\right) = \sum_{k=1,3,\dots}^{\infty} \left( \frac{2}{k\pi} i e^{-i(k\omega t)} - \frac{2}{k\pi} i e^{i(k\omega t)} \right) \quad (4.3)$$

$$F_\mu = \frac{4}{\pi} \mu_d F_N \sum_{k=1,3,\dots}^{\infty} \frac{(-1)^k}{k} \cos(k\omega t - \beta_k) = F_f \sum_{k=1,3,\dots}^{\infty} \frac{(-1)^k}{k} \cos(k\omega t - \beta_k) \quad (4.4)$$

where

- $\omega$  , excitation frequency.
- $t$  , time variable.
- $k$  , number of the harmonic.
- $\beta_k$  , phase of the k-th harmonic with respect to the external harmonic force  $F_e$ .
- $F_f = \frac{4}{\pi} \mu_d F_N$  , amplitude of the friction force.

The external harmonic force  $F_e$  is reported in the equation (4.5) as a cosine function with excitation frequency  $\omega$  and amplitude  $F_0$ .

$$F_e = F_0 \cos(\omega t) \quad (4.5)$$

Once the expressions of the forces acting on the system have been defined, it is possible to substitute them into the equation of motion (4.6) , derived from the free body diagram of the mass (figure 4.2).

$$m\ddot{x} + c\dot{x} + kx = F_e - F_\mu = F_0 \cos(\omega t) - F_\mu \quad (4.6)$$

The equation of motion is non-linear because of the friction force, then the solution of such a differential equation cannot be found by following the usual linear approach. Among the various methods, here the *Harmonic Balance Method* (HBM) is adopted to solve the equation. Then, it is needed to express the response  $x$  in a harmonic form so to be able to apply HBM. Since the external force  $F_e$  and the friction force  $F_\mu$  are forcing functions constituted by odd cosine harmonics, as a consequence the response can be assumed to be of the type expressed in the equation (4.7).

$$x(t) = \sum_{k=1,3,..}^{\infty} u_k (\cos(k\omega t - \gamma_k)) \quad (4.7)$$

where :

- $u_k$  , amplitude of the k-th harmonic.
- $\gamma_k$  , phase of the k-th harmonic with respect to the external force  $F_e$ .

It is now possible to develop the expression of the response (4.7) so to derive the sine and cosine harmonics for the HBM application. Here for simplicity, only the first and the third harmonics are developed (4.9), but further harmonics can be also considered in the equation. The same thing is done for the friction force (4.8). Then, the speed  $\dot{x}$  and the acceleration  $\ddot{x}$  are derived by taking the first and the second derivative of (4.8), obtaining respectively the equations (4.10) and (4.11).

$$F_\mu = -\frac{4}{\pi} \mu_d F_N [\cos(\beta_1) \cos(\omega t) + \sin(\beta_1) \sin(\omega t) + \cos(\beta_3) \cos(3\omega t) + \sin(\beta_3) \sin(3\omega t)] \quad (4.8)$$

$$x(t) = u_1 [\cos(\omega t) \cos(\gamma_1) + \sin(\omega t) \sin(\gamma_1)] + u_3 [\cos(3\omega t) \cos(\gamma_3) + \sin(3\omega t) \sin(\gamma_3)] \quad (4.9)$$

$$\dot{x}(t) = -\omega u_1 [\sin(\omega t) \cos(\gamma_1) - \cos(\omega t) \sin(\gamma_1)] - 3\omega u_3 [\sin(3\omega t) \cos(\gamma_3) - \cos(3\omega t) \sin(\gamma_3)] \quad (4.10)$$

$$\ddot{x}(t) = -\omega^2 u_1 [\cos(\omega t) \cos(\gamma_1) + \sin(\omega t) \sin(\gamma_1)] - (3\omega)^2 [\cos(3\omega t) \cos(\gamma_3) + \sin(3\omega t) \sin(\gamma_3)] \quad (4.11)$$

Finally, the equations (4.8), (4.9), (4.10) and (4.11) are substituted into the equation of motion (4.6) and the HBM can be applied. Two equations per each harmonic  $k$  can be obtained from the application of HBM, which balance the sine and the cosine terms. They are the equations (4.12) and (4.13).

- $k=1$ , balance of  $\sin(\omega t)$  :

$$[ (k - \omega^2 m) \sin(\gamma_1) - c\omega \cos(\gamma_1) ] u_1 = F_f \sin(\beta_1) \quad (4.12a)$$

- $k=1$ , balance of  $\cos(\omega t)$ :

$$[ c\omega \sin(\gamma_1) + (k - \omega^2 m) \cos(\gamma_1) ] u_1 = F_0 + F_f \cos(\beta_1) \quad (4.12b)$$

-  $k=3$ , balance of  $\sin(3\omega t)$  :

$$[ (k - 9\omega^2 m) \sin(\gamma_3) - 3\omega c \cos(\gamma_3) ] u_3 = \frac{1}{3} F_f \sin(\beta_3) \quad (4.13a)$$

-  $k=3$ , balance of  $\cos(3\omega t)$  :

$$[ 3\omega c \sin(\gamma_3) + (k - 9\omega^2 m) \cos(\gamma_3) ] u_3 = \frac{1}{3} F_f \cos(\beta_3) \quad (4.13b)$$

The non-linear equations still contain the two phases  $\beta_k$  and  $\gamma_k$  which are uncorrelated at this stage. Then, a relation between them has to be found in order to solve the non-linear system of equations. By referring to the expressions of the friction force (4.1) and (4.4) , respectively the general expression of  $F_\mu$  and its expanded form in Fourier series, the relation between the two phases can be established by developing the expression of  $\dot{x}$  (4.14), taking the first derivative of (4.7).

$$\dot{x}(t) = \sum_{k=1,3,\dots}^{\infty} -k\omega u_k (\sin(k\omega t - \gamma_k)) \quad (4.14)$$

Since  $F_\mu$ , which is expressed by cosine functions, must have the same sign of  $\dot{x}(t)$  (4.14) it has to be phased by an angle equal to  $\frac{\pi}{2}$  . Then, the final relation that links the phases  $\beta_k$  and  $\gamma_k$  is given by the equation (4.15). By substituting this relation (4.15) into the systems of equation (4.12) and (4.13) a new set of equations, per each harmonic, is obtained. Equations (4.16) and (4.17) refers respectively to the first and the third harmonic.

$$\beta_k = \gamma_k + \frac{\pi}{2} \quad (4.15)$$

$k=1$  :

$$[ (k - \omega^2 m) \sin(\gamma_1) - c\omega \cos(\gamma_1) ] u_1 = F_f \cos(\gamma_1) \quad (4.16a)$$

$$[ c\omega \sin(\gamma_1) + (k - \omega^2 m) \cos(\gamma_1) ] u_1 = F_0 - F_f \sin(\gamma_1) \quad (4.16b)$$

$k=3$  :

$$[ (k - 9\omega^2 m) \sin(\gamma_3) - 3\omega c \cos(\gamma_3) ] u_3 = \frac{1}{3} F_f \cos(\gamma_3) \quad (4.17a)$$

$$[ 3\omega c \sin(\gamma_3) + (k - 9\omega^2 m) \cos(\gamma_3) ] u_3 = -\frac{1}{3} F_f \sin(\gamma_3) \quad (4.17b)$$

Further manipulations of the systems of equations can be done in order to express the solution  $x(t)$  in terms of sine and cosine components instead of using the amplitude and the phase (4.7). This is done in order to handle the solution  $x(t)$  in a easier way, after the computation. The equivalent expression is the following (4.18).

$$x(t) = \sum_{k=1,3}^{\infty} [s_k \sin(k\omega t) + c_k \cos(k\omega t)] \quad (4.18)$$

$$s_k = u_k \sin(\gamma_k) \quad (4.18a)$$

$$c_k = u_k \cos(\gamma_k) \quad (4.18b)$$

By performing the change of variables, the transformed systems of equations (4.19) and (4.20) are ready to be solved.

$k=1$  :

$$(k - \omega^2 m) s_1 - c\omega c_1 = f_{s_1} = F_f \frac{c_1}{\sqrt{c_1^2 + s_1^2}} \quad (4.19a)$$

$$c\omega s_1 + (k - \omega^2 m) c_1 = f_{c_1} = F_0 - F_f \frac{s_1}{\sqrt{c_1^2 + s_1^2}} \quad (4.19b)$$

$k=3$  :

$$(k - 9\omega^2 m) s_3 - 3c\omega c_3 = f_{s_3} = \frac{1}{3} F_f \frac{c_3}{\sqrt{c_3^2 + s_3^2}} \quad (4.20a)$$

$$3c\omega s_3 + (k - 9\omega^2 m) c_3 = f_{c_3} = -\frac{1}{3} F_f \frac{s_3}{\sqrt{c_3^2 + s_3^2}} \quad (4.20b)$$

The non-linear system of equation, for the  $k$ -th harmonic, can be summarized in the following matrix form (4.21), where  $A_k$  is the matrix of the coefficients of the system and it is known,  $v_k$  is the vector of the solutions and  $b_k$  is the forcing vector which is a function of the solutions of the system  $v_k$ .

$$A_k v_k = b_k(v_k) \quad (4.21)$$

$$A_k = \begin{bmatrix} k - (\kappa\omega)^2 m & -c(\kappa\omega) \\ c(\kappa\omega) & k - (\kappa\omega)^2 m \end{bmatrix} \quad (4.21a)$$

$$v_k = (s_k^x, c_k^x)^T \quad (4.21b)$$

$$b_k = (f_{s_k}(s_k, c_k), f_{c_k}(s_k, c_k))^T \quad (4.21c)$$

From the theory on Fourier series, it is known that the response  $x(t)$  can be written in the frequency domain through the combination of the sine and the cosine components of the equation (4.18). Then, the frequency response  $X_k(\omega)$  is given in the equation (4.22). Actually, the computation of the response per each harmonics should consider also the negative harmonics  $-k$ . Since  $X_{-k}(\omega)$  is equal to the complex conjugate of  $X_k(\omega)$ , (4.23), (this is a very well known result in the Fourier series theory) , it is common use to take twice the amplitude of  $X_k(\omega)$  for  $\omega > 0$  (4.24), in order to include also the negative harmonics.

$$X_k(\omega) = \frac{c_k - i s_k}{2} \quad (4.22)$$

$$X_{-k}(\omega) = \frac{c_k + i s_k}{2} \quad (4.23)$$

$$|X_k(\omega)| = |c_k - i s_k| \quad (4.24)$$

Once the equations of motion have been studied for a single degree of freedom system, the next operation is to apply this equations to the case of study. In particular to the model of the sector of the bladed disk, under the condition of cyclic symmetry. As it is mentioned at the beginning of this paragraph, a *blade-to-ground damper* is introduced in the system and it acts on the blade degree of freedom. A representation of the model with the incorporated friction damper is reported in figure 4.3. The equations that govern the motion of such a system are the same of those analyzed in Chapter 1, where the cyclic symmetry property has been studied. The difference is in the forcing vector, where a friction force of the type studied before is added to the external harmonic force acting on the blade. The equation (4.25) describes the motion of the system, once an *inter-blade phase angle*  $\mu$  (so the *EO*) has been set.

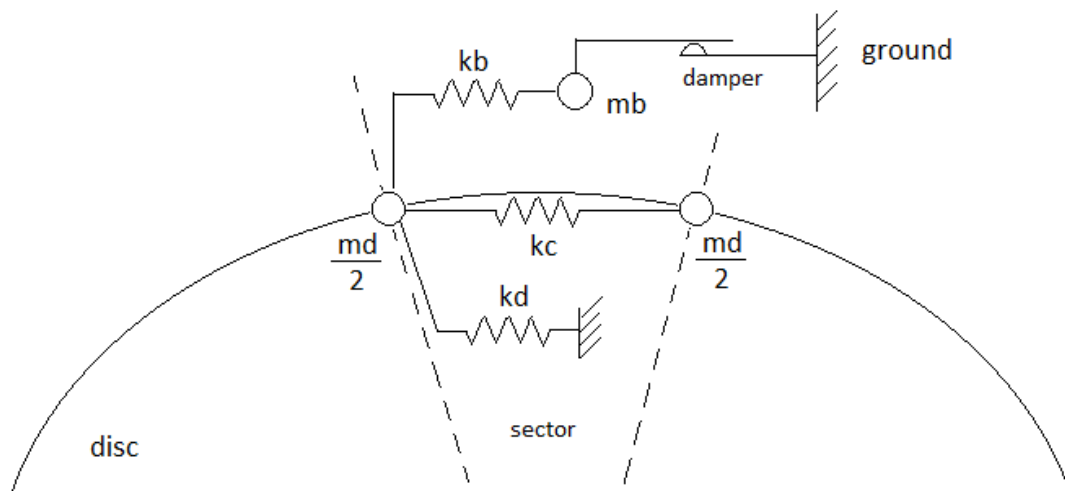


Figure 4.3. model of the sector with *blade-to-ground damper*.

$$M_\mu \ddot{x}_\mu + C_\mu \dot{x}_\mu + K_\mu x_\mu = F = \{ 0, Fe - F_\mu \}^T \quad (4.25)$$

where

- $\{x_\mu\} = \{x_{d,L}, x_B\}^T$ .
- $M_\mu, C_\mu, K_\mu$  are functions of the phase  $\mu$ .

Since the actual system has two degrees of freedom, this leads to a system with four non linear equations, per each harmonic, with four unknowns which are respectively the sine and cosine components of the displacement coordinate of the disk  $x_{d,L}$  and the sine and cosine components of the displacement coordinate of the blade  $x_B$ . The system of equations is analogue to that derived in the single degree of freedom system and it can be written in the following matrix form (4.26).

$$\begin{bmatrix} K_\mu - (k\omega)^2 M_\mu & -(k\omega)C_\mu \\ (k\omega)C_\mu & K_\mu - (k\omega)^2 M_\mu \end{bmatrix} \{S_{k,dL}, S_{k,B}, C_{k,dL}, C_{k,B}\}^T = \{f_{S_{k,dL}}, f_{S_{k,B}}, f_{C_{k,dL}}, f_{C_{k,B}}\}^T \quad (4.26)$$

If  $k = 1$  :

$$\{f_{S_{1,dL}}, f_{S_{1,B}}, f_{C_{1,dL}}, f_{C_{1,B}}\}^T = \left\{ 0, F_f \frac{c_{1,B}}{\sqrt{c_{1,B}^2 + s_{1,B}^2}}, 0, F_0 - F_f \frac{s_{1,B}}{\sqrt{c_{1,B}^2 + s_{1,B}^2}} \right\}^T \quad (4.26a)$$

If  $k > 1$  :

$$\{f_{S_{k,dL}}, f_{S_{k,B}}, f_{C_{k,dL}}, f_{C_{k,B}}\}^T = \left\{ 0, \frac{1}{k} F_f \frac{c_{k,B}}{\sqrt{c_{k,B}^2 + s_{k,B}^2}}, 0, -\frac{1}{k} F_f \frac{s_{k,B}}{\sqrt{c_{k,B}^2 + s_{k,B}^2}} \right\}^T \quad (4.26b)$$

By solving the system of non linear equations it is possible to evaluate the forced response of the blade. The computation has been performed by considering different Engine Orders and by exploring the response of the blade at different preload conditions in the blade-to-ground damper, per each *EO* considered. For simplicity, here only the response computed by solving the system of equations for the first harmonic is reported (it represents also the main contribute to the response, with respect to the other harmonics). In figure 4.4 and 4.5 the forced responses of the blade, considering two different Engine Orders ( respectively *EO*=10 and *EO*=50 ), are plotted for different value of friction force magnitude  $F_f$  (different preload condition). In particular, by considering the normalized friction force with respect to the external force amplitude  $F_0$ , expressed by the ratio  $r = \frac{F_f}{F_0}$ . The plots of the forced response are showed together with the forced response under *no-friction* condition, the magnification factor and the percentage reduction plotted against normalized friction force  $r$  ( $r$  going from  $10^{-3}$  to 0.6 ), in order to quantify the effect of the damper in terms of reduction of the response amplitude in resonance conditions. From figure 4.4 and 4.5 one can easily note that the forced response is not influenced by the *EO*, in fact the reduction in response amplitude is the same for the two situations with different *EO*. The maximum amplitude reduces proportionally as the friction force increases.

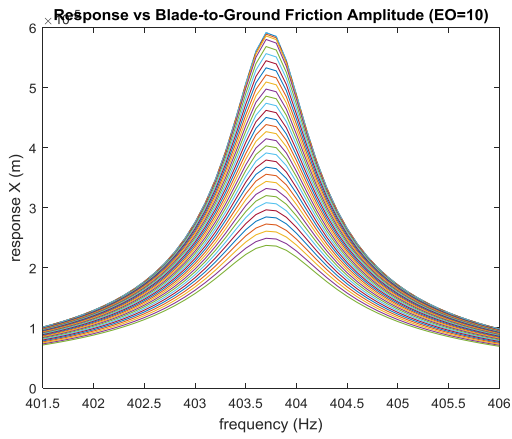


Figure 4.4a. Response for different  $r$  (EO=10)

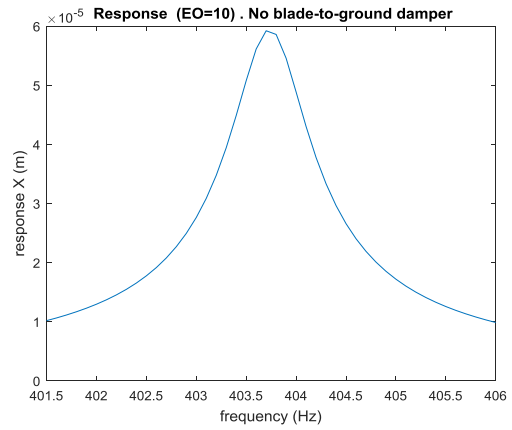


Figure 4.4b. Response without friction damper(EO=10)

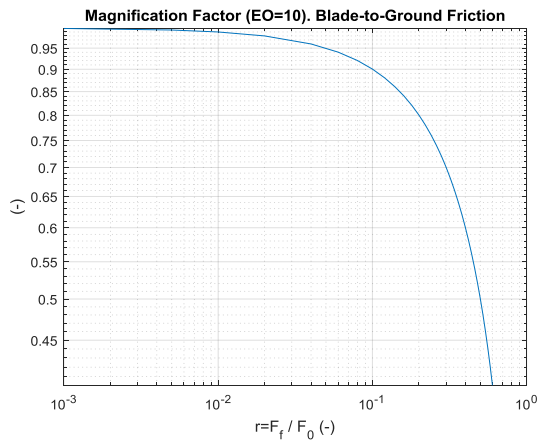


Figure 4.4c. Magnification Factor against  $r$  (EO=10)

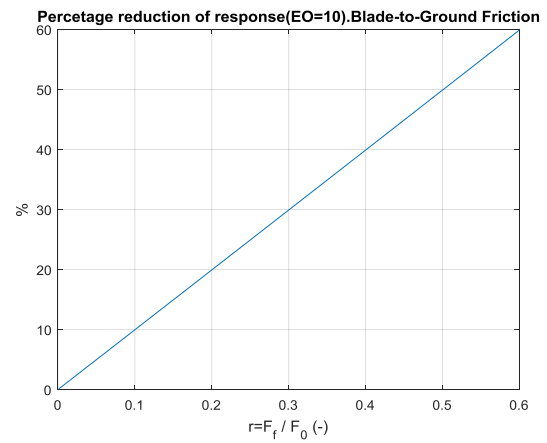


Figure 4.4d. % amplitude reduction against  $r$  (EO=10)

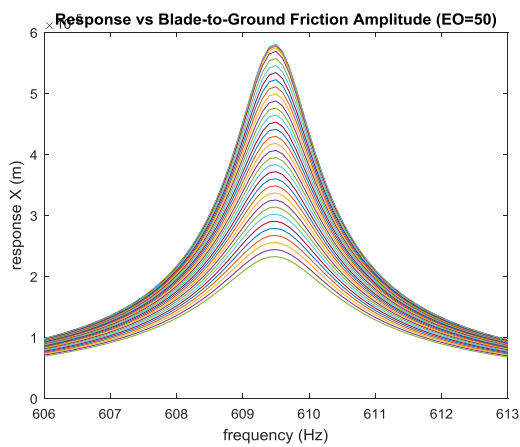


Figure 4.5a. Response for different  $r$  (EO=50)

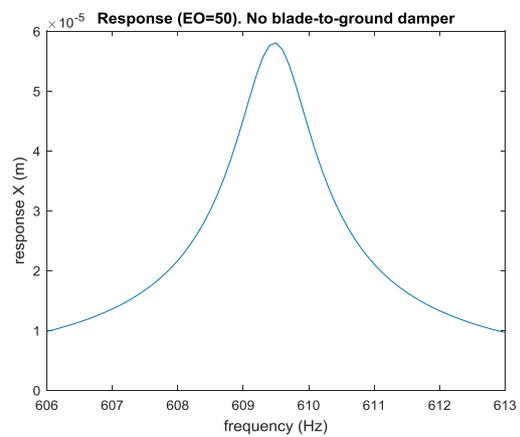


Figure 4.5b. Response without friction damper(EO=50)

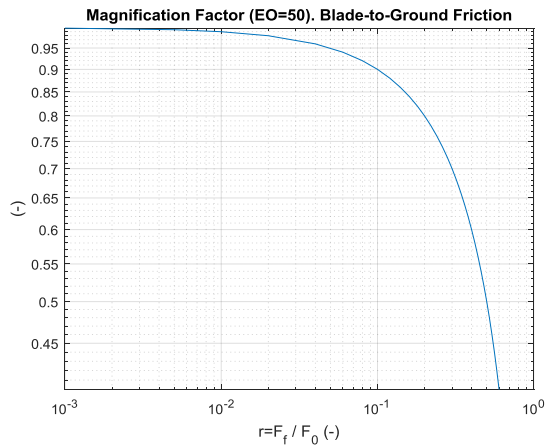


Figure 4.5c. Magnification Factor against  $r$  (EO=50)

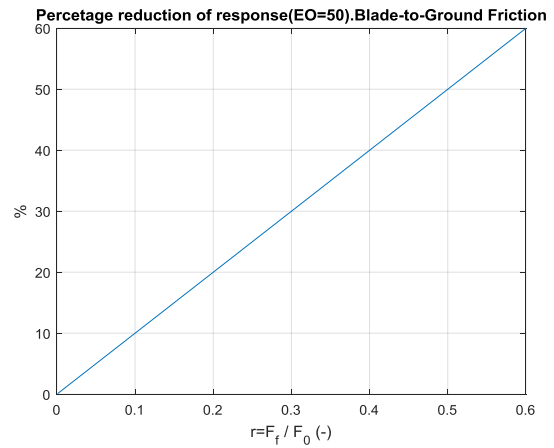


Figure 4.5d. % amplitude reduction against  $r$  (EO=50)

## 4.2 Bladed disk with joint friction

The incorporation of blade-to-ground friction dampers into the model of a bladed disk cannot explain well the dynamics of the system in some circumstances where a friction force is induced among the parts which constitute the whole structure. In fact, friction forces can be generated in the joints connecting the blades to the disk body. In this situation the friction force is dependent both on the blade motion and on the disk motion. Then, the equations of motion of the system have to be modified in order to take into account the combined contribution of the blade and the disk. A new modeling of the sector is required, where a *joint friction damper* is introduced between the blade dof and the disk dof. Such a model is represented in figure 4.6.

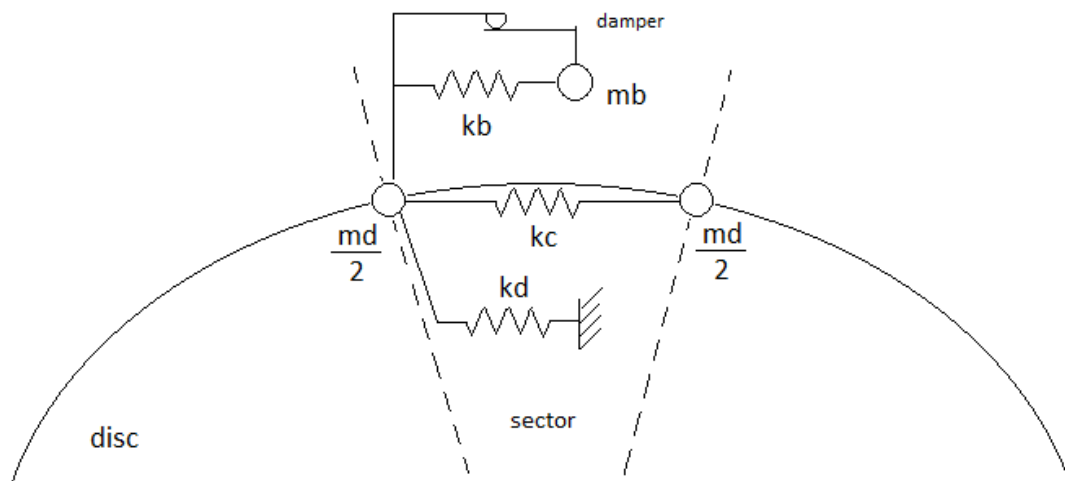


Figure 4.6. Model of the sector with joint friction damper.

As a consequence, the expression of the friction force  $F_\mu$  has to be redefined. More in detail, the friction force is expressed in the equation (4.27). The only difference with respect to the blade-to-ground situation is the argument of the “sign” function which is now the difference between the speed of the blade dof  $\dot{x}_B$  and the speed of the disk dof  $\dot{x}_{d,L}$  (again, the “minus” sign is omitted in the expression of  $F_\mu$  because the force is taken directly in the opposite direction with respect to the speed of the blade, as showed in figure 4.7).

$$F_\mu = \mu_d F_N \text{sign}(\Delta\dot{x}) \quad (4.27)$$

where  $\Delta\dot{x} = \dot{x}_B - \dot{x}_{d,L}$  is the difference function.

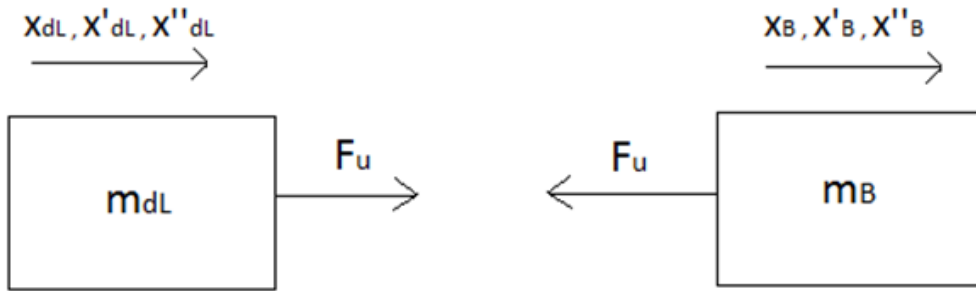


Figure 4.7. Friction force  $F_\mu$  between the blade and the disk degrees of freedom

Regardless of the argument of the “sign” function inside the expression of the friction force, the latter can be expanded in Fourier series. So, in the equation (4.28) is recalled the Fourier expansion of  $F_\mu$  that has been derived in the previous paragraph.

$$F_\mu = \frac{4}{\pi} \mu_d F_N \sum_{k=1,3,\dots}^{\infty} \frac{(-1)^k}{k} \cos(k\omega t - \beta_k) \quad (4.28)$$

where  $\beta_k$  is again the phase of the  $k$ -th harmonic with respect to the external harmonic force  $F_e$  and it is not defined at this stage. As for the study of the response in presence of blade-to-ground dampers, here the aim is to apply HBM with the same procedure used in the previous paragraph. Then, the equations of motion, on the left hand side, are exactly equal to the ones used before (4.26). In order to find a relation which links the phase  $\beta_k$  (4.28) to the unknowns of the system (the sine and cosine components of the two coordinates  $x_{d,L}$  and  $x_B$ ), a development of the difference function  $\Delta\dot{x}$ , which imposes the sign to the friction force  $F_\mu$  (4.27), is needed. By referring to the general expression of the displacement coordinates in the time domain  $x_{d,L}(t)$  and  $x_B(t)$ , respectively equations (4.29) and (4.30), the difference function  $\Delta\dot{x}$  is developed by taking the first the derivative of the two displacement coordinates and by subtracting them (4.31). Here, for simplicity, only the first harmonic ( $k=1$ ) is developed.

$$x_{d,L}(t) = \sum_{k=1,3,..}^{\infty} [ u_{d,k} \cos(k\omega t - \gamma_{d,k}) ] \quad (4.29)$$

$$x_B(t) = \sum_{k=1,3,..}^{\infty} [ u_{B,k} \cos(k\omega t - \gamma_{B,k}) ] \quad (4.30)$$

where

- $u_k$  amplitude of the  $k$ -th harmonic of the displacement  $x$ .
- $\gamma_k$ , phase of the  $k$ -th harmonic of the displacement  $x$  with respect to the force  $F_e$ .

$$\Delta \dot{x} = \dot{x}_B - \dot{x}_{d,L} = (s_{1,B} - s_{1,d}) \omega \cos(\omega t) + (c_{1,d} - c_{1,B}) \omega \sin(\omega t) \quad (4.31)$$

where

- $s_{1,d} = u_{1,d} \sin(\gamma_{1,d})$ .
- $s_{1,B} = u_{1,B} \sin(\gamma_{1,B})$ .
- $c_{1,d} = u_{1,d} \cos(\gamma_{1,d})$ .
- $c_{1,B} = u_{1,B} \cos(\gamma_{1,B})$ .

By exploiting the properties of trigonometry, the difference function (4.31) can be written with a cosine function of amplitude  $A$  and phase  $\varphi_1$  (4.32).

$$\Delta \dot{x} = A \cos(\omega t - \varphi_1) \quad (4.32)$$

$$A = \sqrt{(s_{1,B} - s_{1,d})^2 + (c_{1,d} - c_{1,B})^2} \quad (4.32a)$$

$$\varphi_1 = \text{atan}\left(\frac{c_{1,d} - c_{1,B}}{s_{1,B} - s_{1,d}}\right) \quad (4.32b)$$

So, a new expression of the friction force is derived from the development of the difference function  $\Delta \dot{x}$  (4.33). By considering for simplicity only the first harmonic of the Fourier expansion of the friction force (4.34), it is easy to find a relation between the two equivalent expressions.

$$F_\mu = \mu_d F_N \text{sign}(\Delta \dot{x}) = \mu_d F_N \text{sign}[A \cos(\omega t - \varphi_1)] \quad (4.33)$$

$$F_\mu = \frac{4}{\pi} \mu_d F_N (-1) \cos(\omega t - \beta_1) \quad (4.34)$$

Expression (4.33) is represented by a “positive” cosine function while the expression (4.34) is represented by a “negative” cosine function. In order to have a coherence between the two expressions it is necessary to transform (4.33) into a “negative” cosine function by phasing it of an angle of  $\pi$ , obtaining the expression (4.35). Since  $F_\mu$  is proportional to the sign of the

difference function, it is enough to match the phase of the expanded form (4.34) and the phase of the argument of the “sign” function in the equation (4.35), giving the relation reported in the equation (4.36). This relation links the friction force to the displacement coordinate components representing the unknowns of the non linear system of equations (4.37), which is derived again by the application of the equations (4.12) and (4.13) to the 2-dofs system in exam.

$$F_\mu = \mu_d F_N \text{sign}[-A \cos(\omega t - \varphi_1 + \pi)] \quad (4.35)$$

$$\beta_1 = \varphi_1 - \pi = \text{atan}\left(\frac{c_{1,d} - c_{1,B}}{s_{1,B} - s_{1,d}}\right) - \pi \quad (4.36)$$

$$\begin{bmatrix} K_\mu - (k\omega)^2 M_\mu & -(k\omega)C_\mu \\ (k\omega)C_\mu & K_\mu - (k\omega)^2 M_\mu \end{bmatrix} \{s_{k,dL}, s_{k,B}, c_{k,dL}, c_{k,B}\}^T = \{f_{s_{k,dL}}, f_{s_{k,B}}, f_{c_{k,dL}}, f_{c_{k,B}}\}^T \quad (4.37)$$

If  $k = 1$  :

$$\{f_{s_{1,dL}}, f_{s_{1,B}}, f_{c_{1,dL}}, f_{c_{1,B}}\}^T = \{0, F_f \sin(\beta_1), 0, F_0 + F_f \cos(\beta_1)\}^T \quad (4.37a)$$

If  $k > 1$  :

$$\{f_{s_{k,dL}}, f_{s_{k,B}}, f_{c_{k,dL}}, f_{c_{k,B}}\}^T = \left\{0, \frac{1}{k} F_f \sin(\beta_k), 0, \frac{1}{k} F_f \cos(\beta_k)\right\}^T \quad (4.37b)$$

where  $F_f = \frac{4}{\pi} \mu_d F_N$ .

As for the study in the previous paragraph, the computation of the forced response has been performed by assuming different Engine Orders and by varying the magnitude of the friction force. The response is now dependent on the EO. For a certain value of the normalized friction force  $r$ , the reduction of the maximum amplitude of the response in resonance condition, with respect to the case of *no-friction*, increases as the EO increases. The maximum reduction in amplitude is obtained for EO values near to  $\frac{N}{2}$ . In the case of study,  $N$  is equal to 146 (which is the number of blades in the bladed disk). As a matter of fact, for EO equal to 70 the maximum reduction in amplitude is obtained. It is interested to note that for EO near to  $\frac{N}{2}$ , the forced response coincides with that obtained from the study of the system with blade-to-ground damper. Here, the forced responses related to different EO values are reported in the following figures.

EO = 2 :

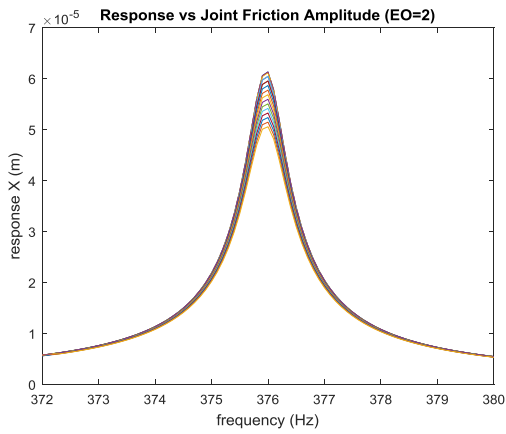


Figure 4.8a. Response for different  $r$  (EO=2)

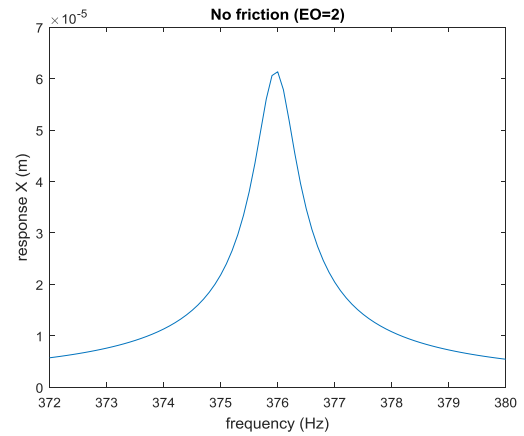


Figure 4.8b. Response without friction damper (EO=2)

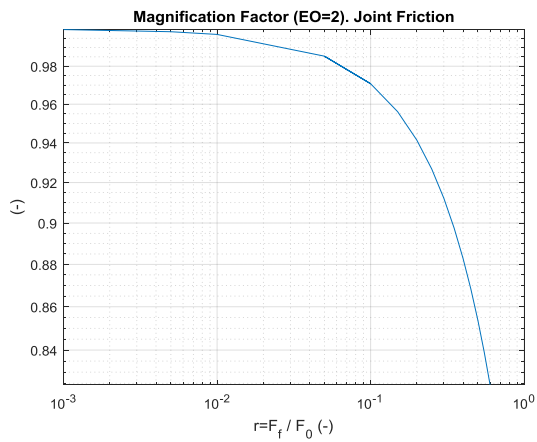


Figure 4.8c. Magnification Factor against  $r$  (EO=2)

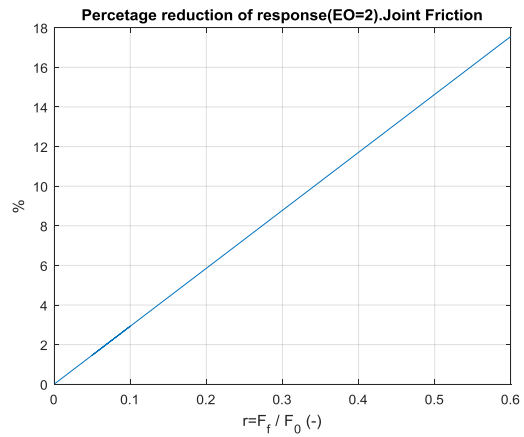


Figure 4.8d. % amplitude reduction against  $r$  (EO=2)

EO = 5 :

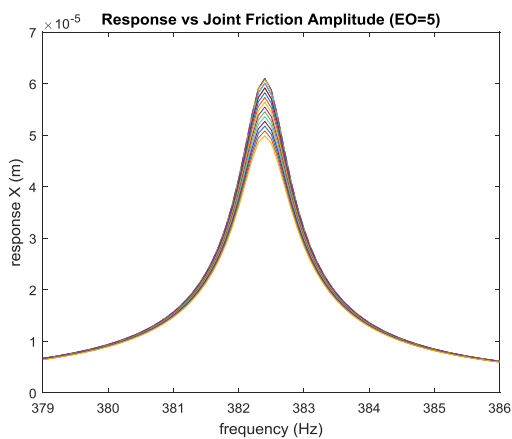


Figure 4.9a. Response for different  $r$  (EO=5)

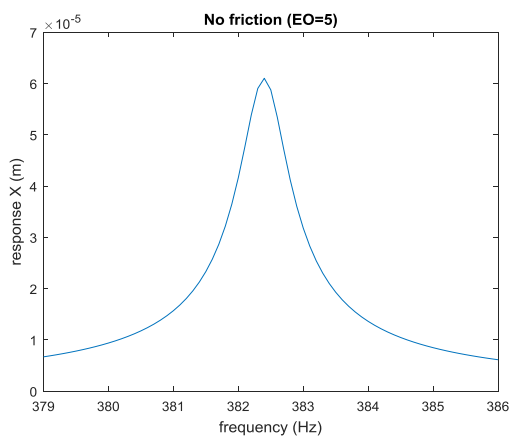
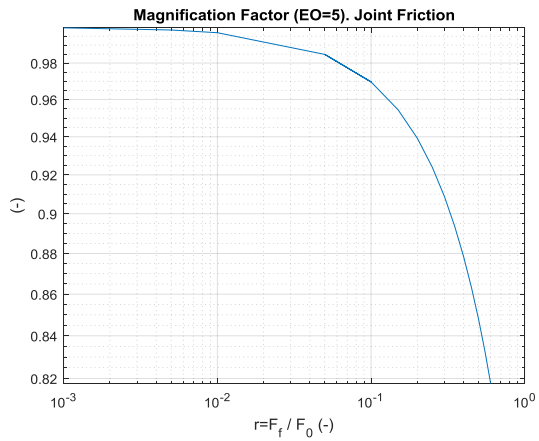


Figure 4.9b. Response without friction damper (EO=5)



4.9c. Magnification Factor against  $r$  (EO=5)

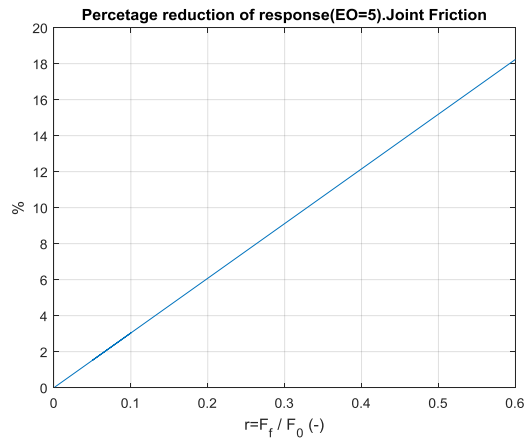


Figure 4.9d. % amplitude reduction against  $r$  (EO=5)

EO = 10 :

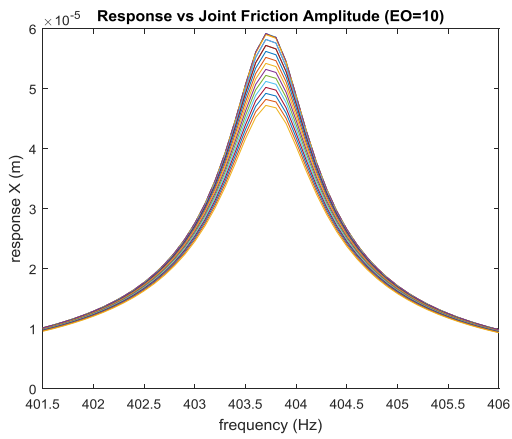


Figure 4.10a. Response for different  $r$  (EO=10)

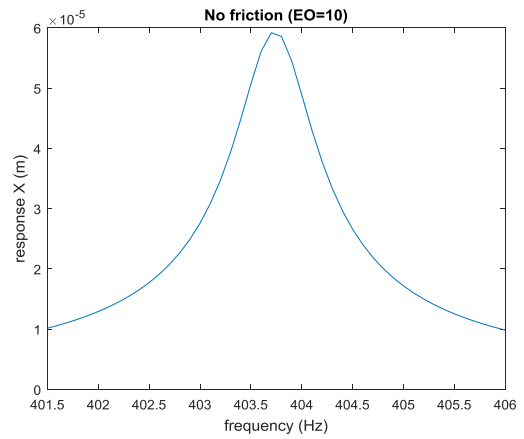
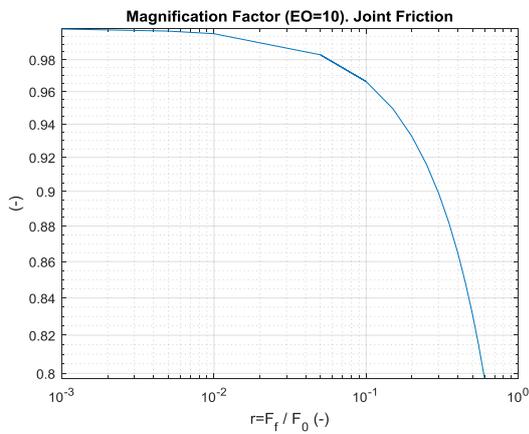


Figure 4.10b. Response without friction damper (EO=10)



4.10c. Magnification Factor against  $r$  (EO=10)

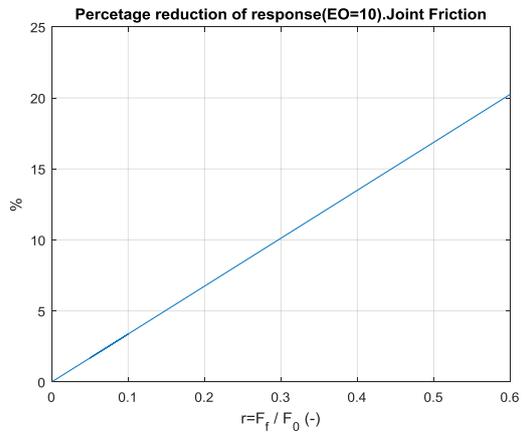


Figure 4.10d. % amplitude reduction against  $r$  (EO=10)

EO = 20 :

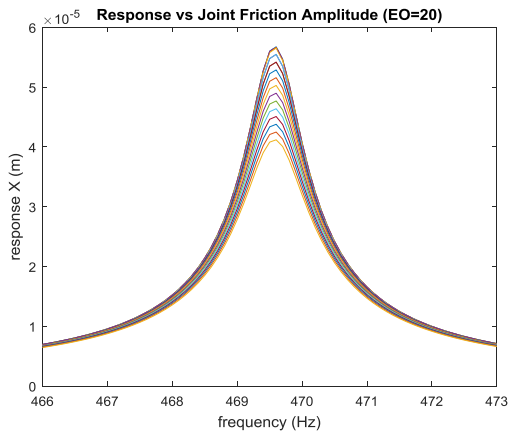


Figure 4.11a. Response for different  $r$  (EO=20)

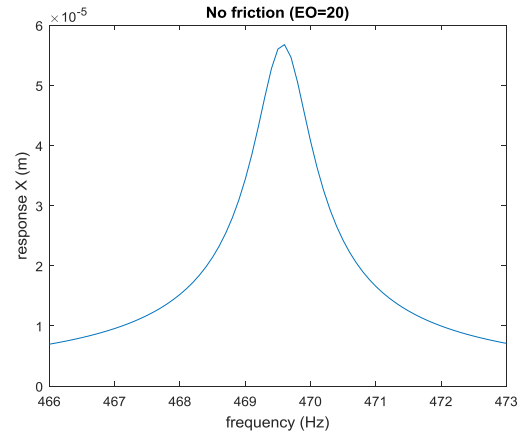
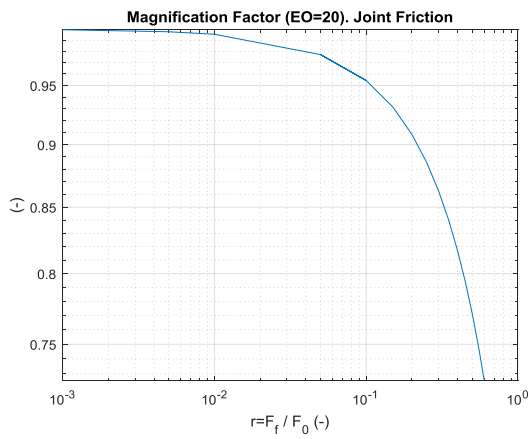


Figure 4.11b. Response without friction damper (EO=20)



4.11c. Magnification Factor against  $r$  (EO=20)

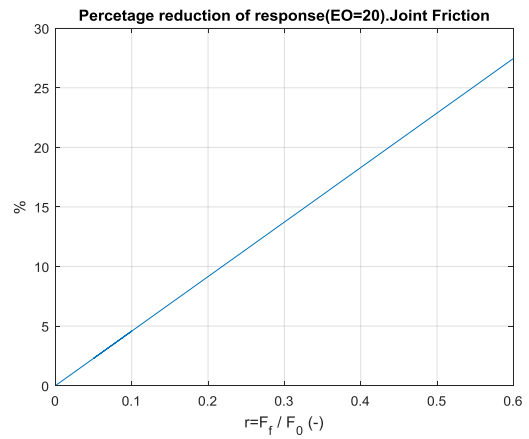


Figure 4.11d. % amplitude reduction against  $r$  (EO=20)

EO = 30 :

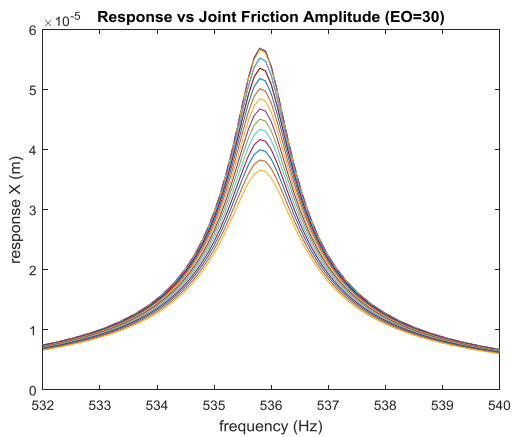


Figure 4.12a. Response for different  $r$  (EO=30)

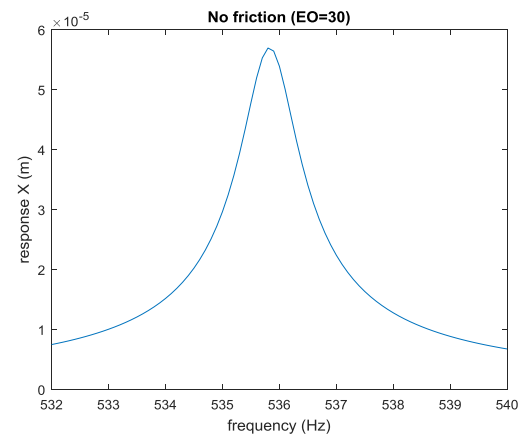
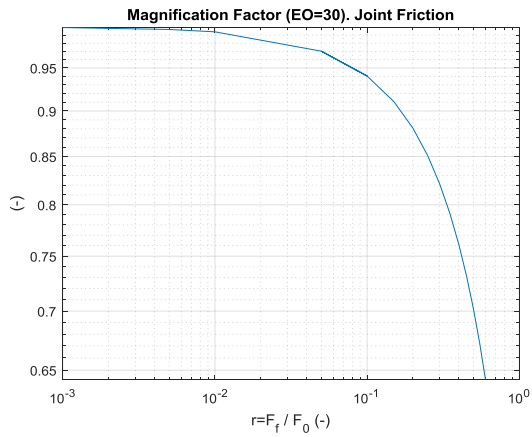


Figure 4.12b. Response without friction damper (EO=30)



4.12c. Magnification Factor against  $r$  (EO=30)

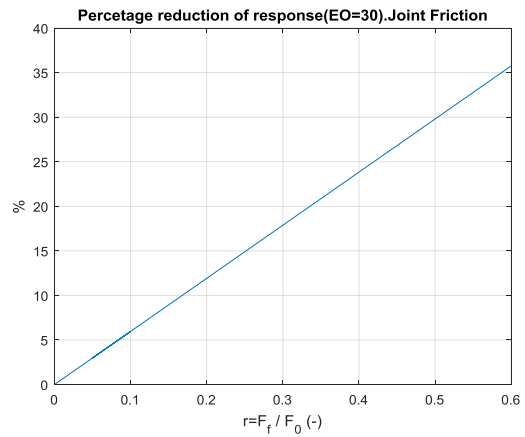


Figure 4.12d. % amplitude reduction against  $r$  (EO=30)

EO = 40 :

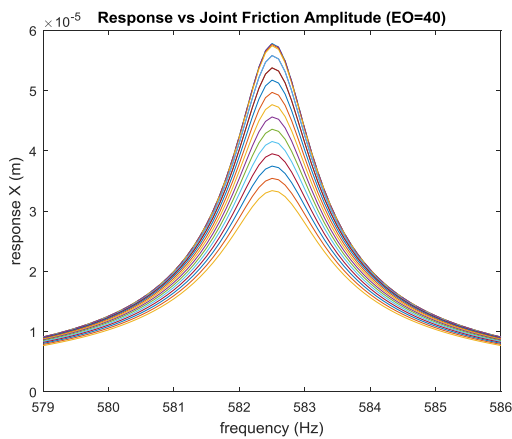


Figure 4.13a. Response for different  $r$  (EO=40)

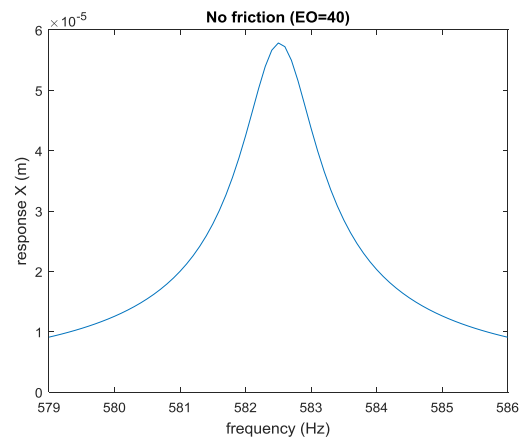
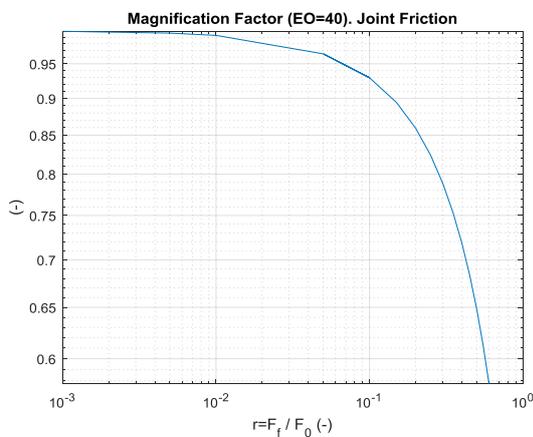


Figure 4.13b. Response without friction damper (EO=40)



4.13c. Magnification Factor against  $r$  (EO=40)

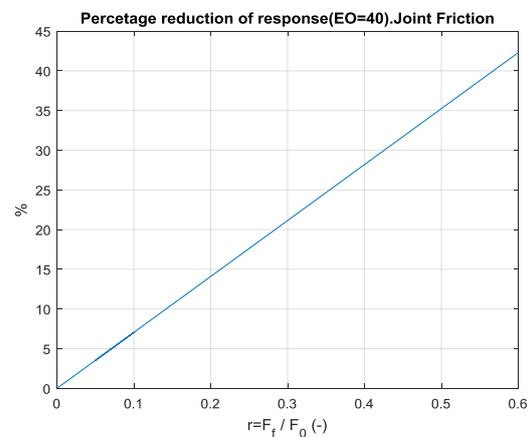


Figure 4.13d. % amplitude reduction against  $r$  (EO=40)

EO = 50 :

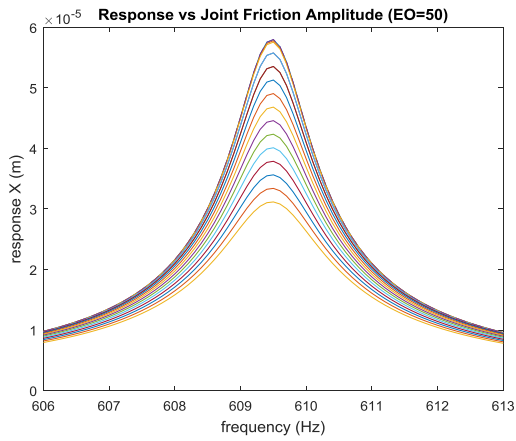


Figure 4.14a. Response for different  $r$  (EO=50)

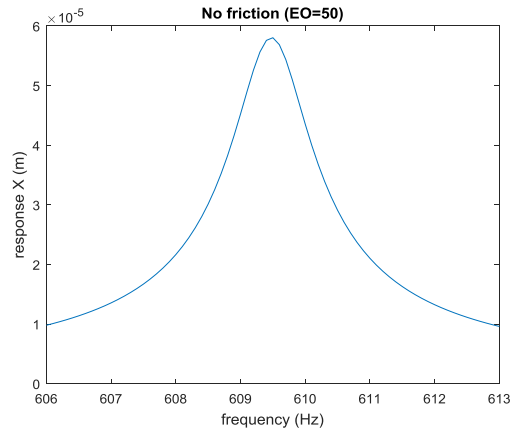
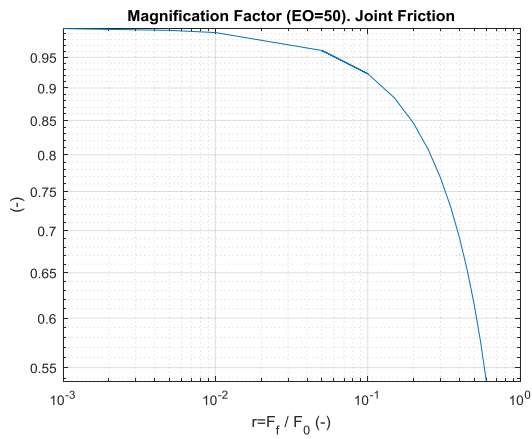


Figure 4.14b. Response without friction damper (EO=50)



4.14c. Magnification Factor against  $r$  (EO=50)

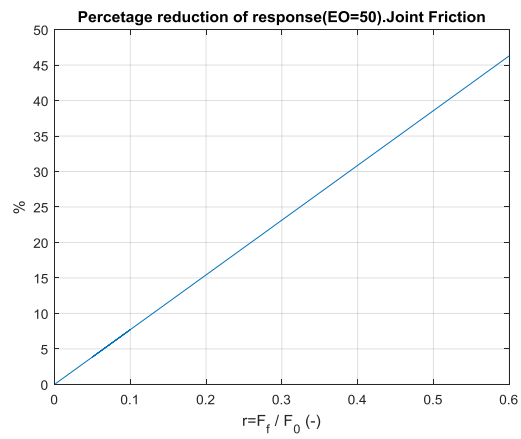
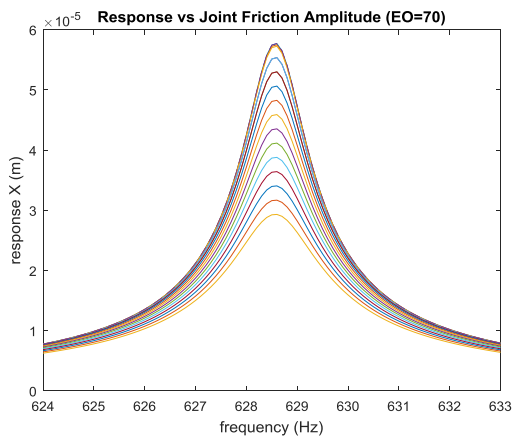


Figure 4.14d. % amplitude reduction against  $r$  (EO=50)

EO = 70 :



4.15a. Response for different  $r$  (EO=70)

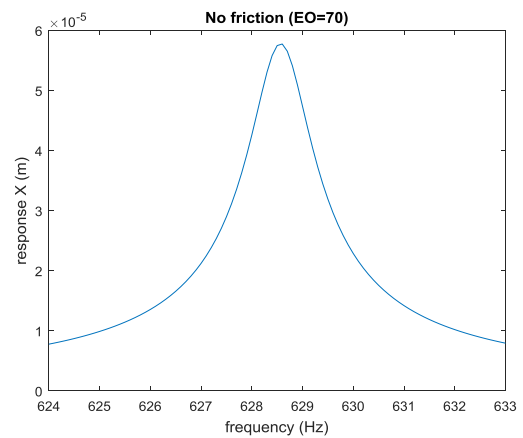
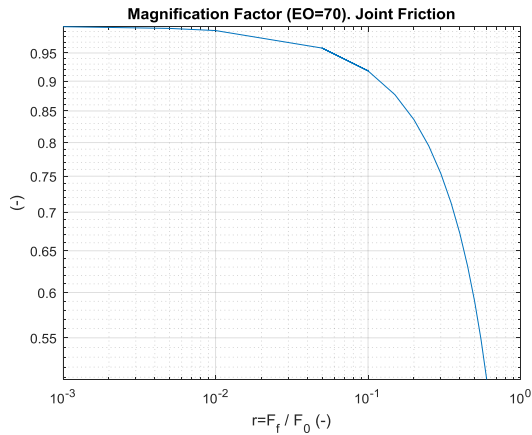


Figure 4.15b. Response without friction damper (EO=70)



4.15c. Magnification Factor against  $r$  (EO=70)

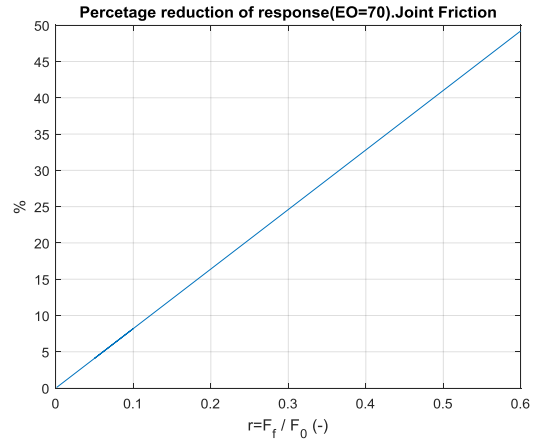


Figure 4.15d. % amplitude reduction against  $r$  (EO=70)

### 4.3 Bladed disk with blade-to-blade friction

Another situation in which friction can take place during the motion of a bladed disk is represented by the shrouds of the blades, if the latter are provided with such a configuration. In order to study how the system behaves under this condition, a new model of the sector has to be defined. In fact, it has to include at least two blades. Then, the reference model of the sector is the one reported in figure 4.16. In particular, the sector is made of two halves of two adjacent blades, in order to satisfy the condition of cyclic symmetry of the structure.

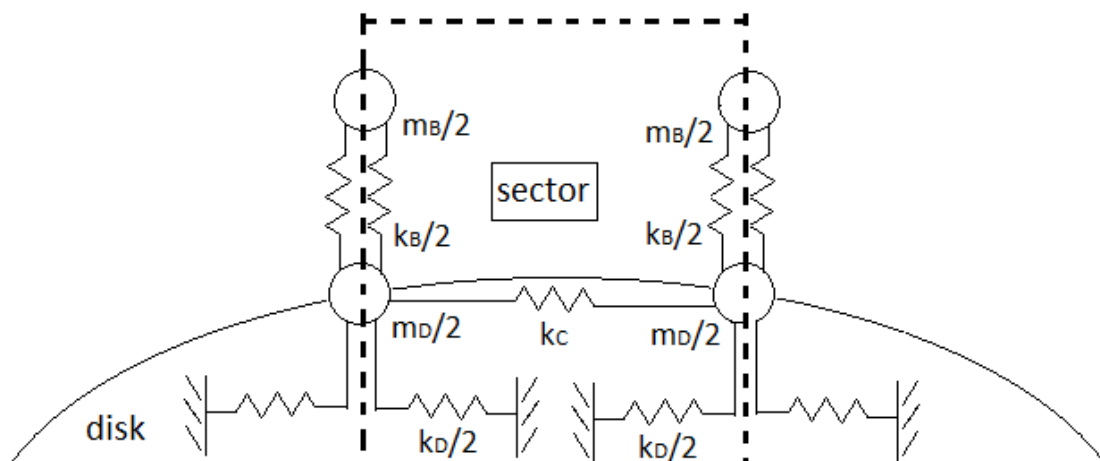


Figure 4.16. Model of the sector for the shroud friction study.

The lumped parameters model of the sector has four degrees of freedom  $x_{d1}$ ,  $x_{d2}$ ,  $x_{b1}$  and  $x_{b2}$ , respectively the disk degrees of freedom at the left and right boundaries of the sector and the blades degrees of freedom at the left and the right boundaries of the sector (4.27). The mass, damping and stiffness matrices, which describe the model, have been derived in the Appendix 3, and they are  $M_s$ ,  $C_s$  and  $K_s$  (A-3.3). The equation of motion of the sector is written in (4.28).

$$\{x\} = \{x_{d1}, x_{d2}, x_{b1}, x_{b2}\}^T \quad (4.27)$$

$$M_s \ddot{x} + C_s \dot{x} + K_s x = 0 \quad (4.28)$$

In order to evaluate the forced response of the system to an external harmonic force acting on the blades, under the condition of sliding friction between the blades, it is necessary to introduce into the model a *blade-to-blade damper* so to simulate the effect of the friction at the shrouds of the blades (figure 4.17). As for the case of blade-to-ground damper and joint damper, the aim of the study is to compute the forced response by means of the Harmonic Balance Method.

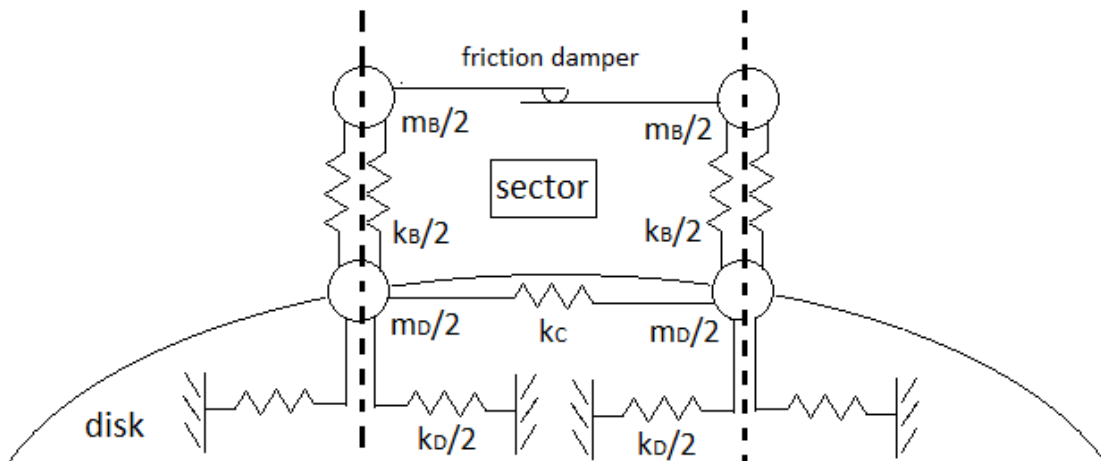


Figure 4.17. Sector model with incorporated *blade-to-blade damper*.

The friction force  $F_\mu$  which is established between the blades is proportional to the sign of the difference in speed of the blades masses (4.29). Thanks to the cyclic symmetry of the disk, the speed of one of the two blades masses can be expressed as a function of the speed of the other (4.30).

$$F_\mu = \mu_d F_N \text{sign}(x_{b1} - x_{b2}) = \mu_d F_N \text{sign}[(1 - e^{i\mu}) \dot{x}_{b1}] \quad (4.29)$$

$$x_{b2} = e^{i\mu} x_{b1} \quad (4.30)$$

By considering a generic variable  $y$ , the function describing the friction force can be expanded in Fourier series (4.31).

$$\mathcal{F}(\text{sign}[(1 - e^{i\mu})y]) = \sum_{k=1,3,\dots}^{\infty} \frac{2}{k\pi} \left[ -e^{i(k\omega t + \frac{k\mu}{2})} + e^{-i(k\omega t - \frac{k\mu}{2})} \right] \quad (4.31)$$

The Fourier expansion (4.31) can be applied to the friction force function. By developing this expression, it is possible to write the friction force with a cosine function (4.32), where  $\beta_k$  is the phase of the  $k$ -th harmonic with respect to the external harmonic force  $F_e$  (4.33).

$$F_\mu = -i \frac{4}{\pi} \mu_d F_N \sum_{k=1,3,\dots}^{\infty} \left[ e^{i \frac{k\mu}{2}} \frac{(-1)^k}{k} \cos(k\omega t - \beta_k) \right] \quad (4.32)$$

$$F_e = F_0 \cos(\omega t) \quad (4.33)$$

The expression of the friction force (4.32) is analogue to the case of *blade-to-ground damper*. In fact, it is possible to write, per each harmonic  $k$ , the contribution of friction in time domain, as follows:

$$F_\mu^k = -i \frac{4}{\pi} \mu_d F_N e^{i \frac{k\mu}{2}} \frac{(-1)^k}{k} \cos(k\omega t - \beta_k) = F_f(\mu) \left[ \frac{(-1)^k}{k} \cos(k\omega t - \beta_k) \right] \quad (4.34)$$

$$\text{where } F_f(\mu) = -i \frac{4}{\pi} \mu_d F_N e^{i \frac{k\mu}{2}}.$$

The equation (4.34) is equivalent to equation (4.4) in paragraph 4.1, which describes the friction force in the study of a single degree of freedom system with *blade-to-ground damper*, with the exception of  $F_f(\mu)$  that is a function of the inter-blade phase angle. This allows to apply the HBM in the same way of the *blade-to-ground* case. If the response  $x$  is defined, in the general form, with a cosine function having a phase  $\gamma_k$  with respect to the external force (4.35), the relation between the phase  $\gamma_k$  and the phase  $\beta_k$  is still (4.36). The non linear equations of motion which derive from HBM are the same of the *blade-to-ground* case (4.16) with the exception of the  $F_f(\mu)$  which has a different expression. In the equation (4.37) is reported only the system of non-linear equation for the first harmonic.

$$x(t) = \sum_{k=1,3,\dots}^{\infty} u_k(\cos(k\omega t - \gamma_k)) \quad (4.35)$$

$$\beta_k = \gamma_k + \frac{\pi}{2} \quad (4.36)$$

$k=1$  :

$$[ (k - \omega^2 m) \sin(\gamma_1) - c\omega \cos(\gamma_1) ] u_1 = F_f(\mu) \cos(\gamma_1) \quad (4.37a)$$

$$[ c\omega \sin(\gamma_1) + (k - \omega^2 m) \cos(\gamma_1) ] u_1 = F_0 - F_f(\mu) \sin(\gamma_1) \quad (4.37b)$$

Since the friction force can be written entirely as a function of the speed of left hand side blade, the equation of motion can be modified through a proper transformation matrix  $[T]$ , whose construction has been explained in Appendix 3 (A-3.6). This transformation introduces the inter-blade phase angle  $\mu$  into the equation, by reducing the degrees of freedom of the model from four to two. In particular, the new set of coordinate  $\{x'\}$  contains the disk dof and the blade dof on the left boundary of the sector, since the other dofs are directly derived from the latter. The new equation of motion is the one showed in equation (4.38) and the mass, damping and stiffness matrices are function of the inter-blade phase.

$$M'_s(\mu) \ddot{x}' + C'_s(\mu) \dot{x}' + K'_s(\mu) x' = F = \{ 0, Fe - F_\mu \}^T \quad (4.38)$$

where  $\{x'\} = \{x_{d1}, x_{b1}\}^T$ .

The forcing vector  $\{F\}$  contains the forces applied to the degrees of freedom of the reduced model. In particular the non zero term of the vector is the second one, related to the blade dof, and it contains the external force and the friction force. Now it is possible to introduce the expressions of the friction force and the external force into the forcing vector and apply the HBM to the system in exam. The system contains four non-linear equations with four unknowns, per each harmonic, and its form is the same of that derived in the *blade-to-ground* case with the exception of  $F_f(\mu)$  (4.39).

$$\begin{bmatrix} K_\mu - (k\omega)^2 M_\mu & -(k\omega)C_\mu \\ (k\omega)C_\mu & K_\mu - (k\omega)^2 M_\mu \end{bmatrix} \{s_{k,dL}, s_{k,B}, c_{k,dL}, c_{k,B}\}^T = \{f_{s_{k,dL}}, f_{s_{k,B}}, f_{c_{k,dL}}, f_{c_{k,B}}\}^T \quad (4.39)$$

If  $k = 1$  :

$$\{f_{s_{1,dL}}, f_{s_{1,B}}, f_{c_{1,dL}}, f_{c_{1,B}}\}^T = \left\{ 0, F_f(\mu) \frac{c_{1,B}}{\sqrt{c_{1,B}^2 + s_{1,B}^2}}, 0, F_0 - F_f(\mu) \frac{s_{1,B}}{\sqrt{c_{1,B}^2 + s_{1,B}^2}} \right\}^T \quad (4.39a)$$

If  $k > 1$  :

$$\{f_{s_{k,dL}}, f_{s_{k,B}}, f_{c_{k,dL}}, f_{c_{k,B}}\}^T = \left\{ 0, \frac{1}{k} F_f(\mu) \frac{c_{k,B}}{\sqrt{c_{k,B}^2 + s_{k,B}^2}}, 0, -\frac{1}{k} F_f(\mu) \frac{s_{k,B}}{\sqrt{c_{k,B}^2 + s_{k,B}^2}} \right\}^T \quad (4.39b)$$

By solving the non-linear system, the response amplitude of the blade, per each harmonic, is directly derived by the component sine and cosine  $s_{k,B}$ ,  $c_{k,B}$  which solve the non-linear system. Again, here are reported the responses computed for the first harmonic only, by setting different values of EO and different preload conditions, as for the previous studies in paragraph 4.1 and 4.2. For low EO (2,5,10) the friction force induces a boost in the amplitude, so the friction force behaves as a dragging force and it increases the response. As the EO increases (20,30), the damping effect is visible for a certain range of preload. The reduction of the amplitude reaches a maximum and then start to decrease by increasing the preload in the damper. For high EO (40,50,70) what is obtained is a continuous decrease of the amplitude as the preload increases. In particular for EO equal to 70 (near  $\frac{N}{2}$ ) the situation is equivalent to the case of *blade-to-ground damper* where the reduction of the amplitude is proportional to the preload and it represents the limit case which leads to a maximum damping of the response in resonance conditions.

EO = 2 :

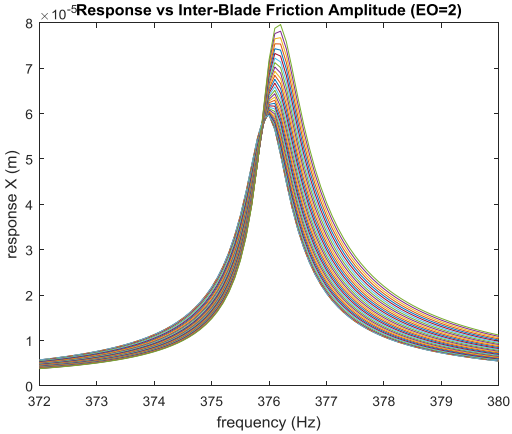


Figure 4.18a. Response for different  $r$  (EO=2)

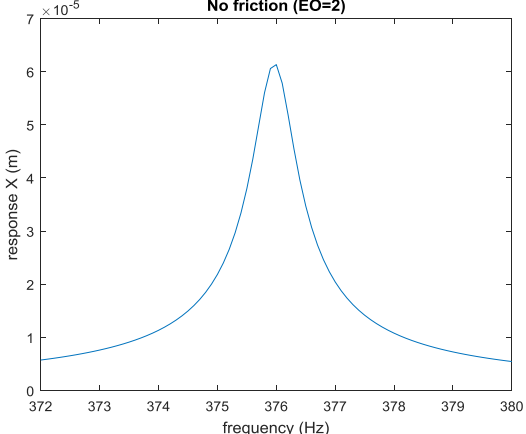
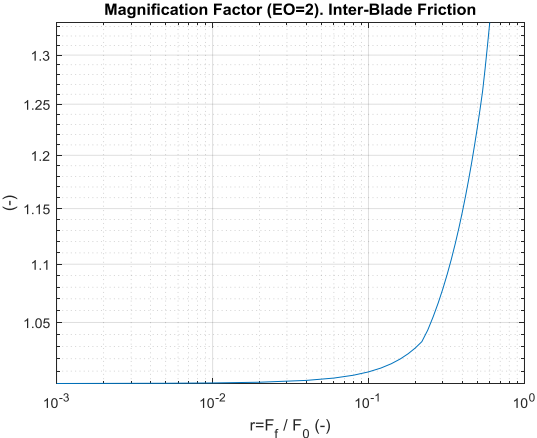


Figure 4.18b. Response without friction damper (EO=2)



4.18c. Magnification Factor against  $r$  (EO=2)

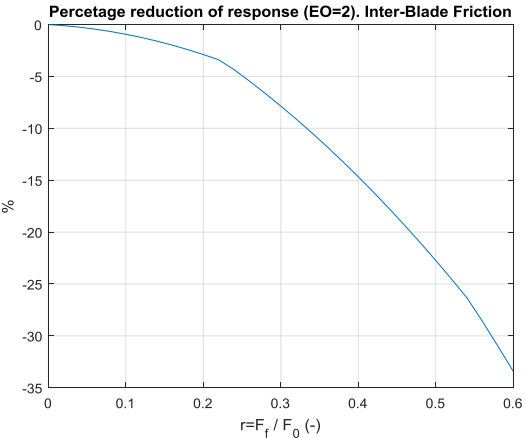


Figure 4.18d. % amplitude reduction against  $r$  (EO=2)

EO = 5 :

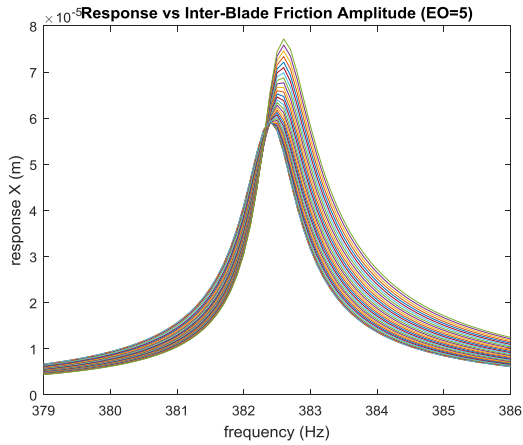


Figure 4.19a. Response for different  $r$  (EO=5)

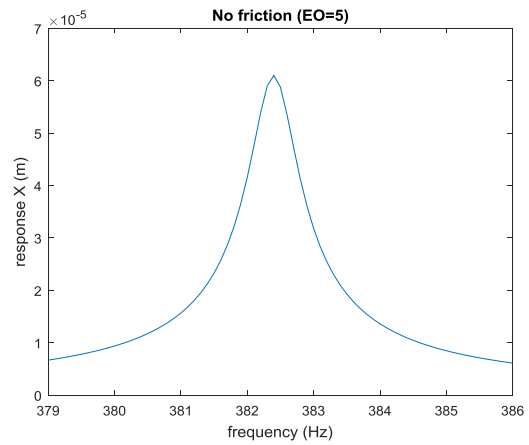
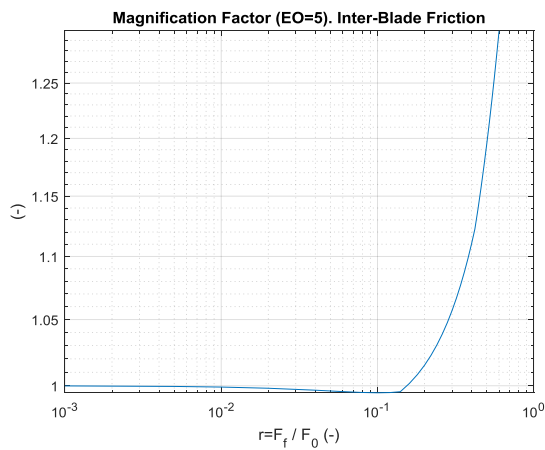


Figure 4.19b. Response without friction damper (EO=5)



4.19c. Magnification Factor against  $r$  (EO=5)

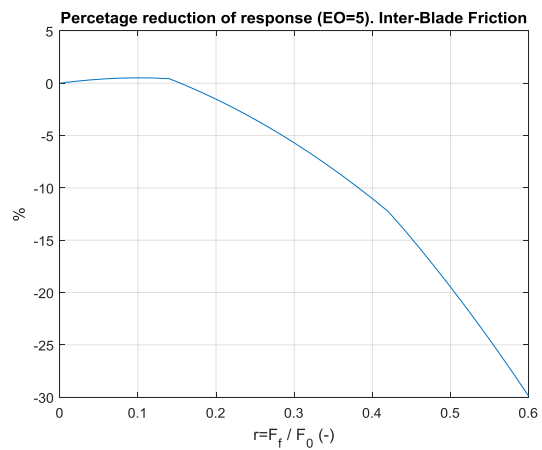


Figure 4.19d. % amplitude reduction against  $r$  (EO=5)

EO = 10 :

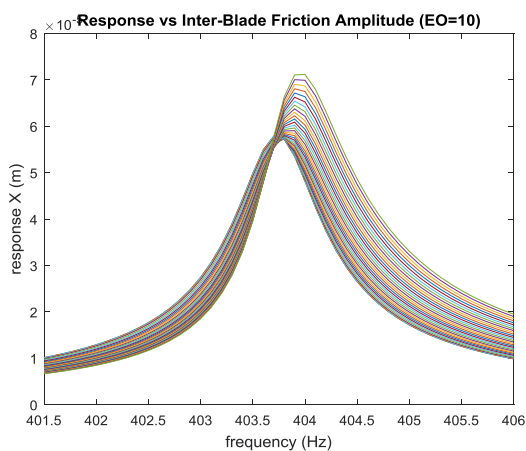


Figure 4.20a. Response for different  $r$  (EO=10)

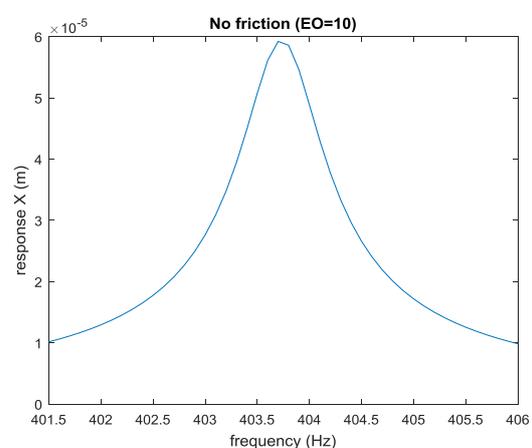
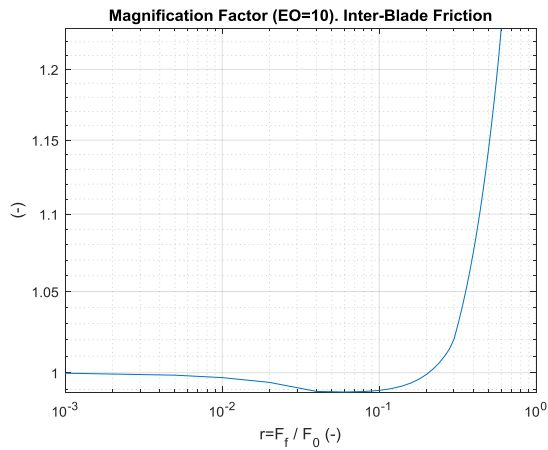


Figure 4.20b. Response without friction damper (EO=10)



4.20c. Magnification Factor against  $r$  (EO=10)

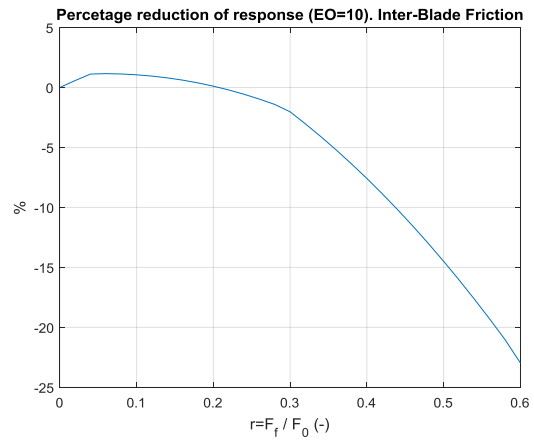


Figure 4.20d. % amplitude reduction against  $r$  (EO=10)

EO = 20 :

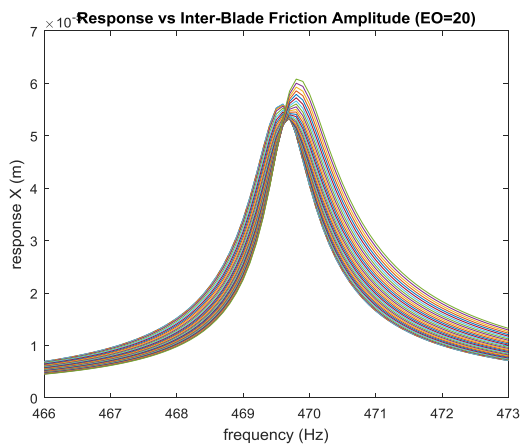


Figure 4.21a. Response for different  $r$  (EO=20)

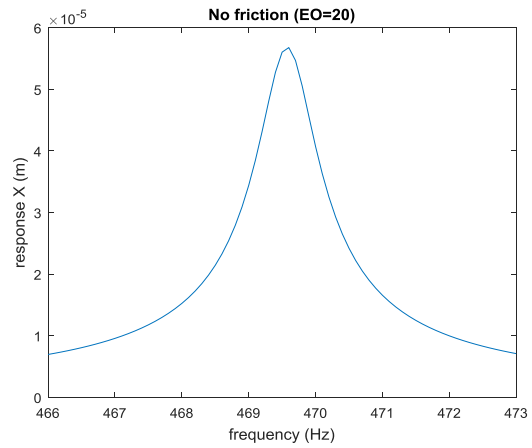
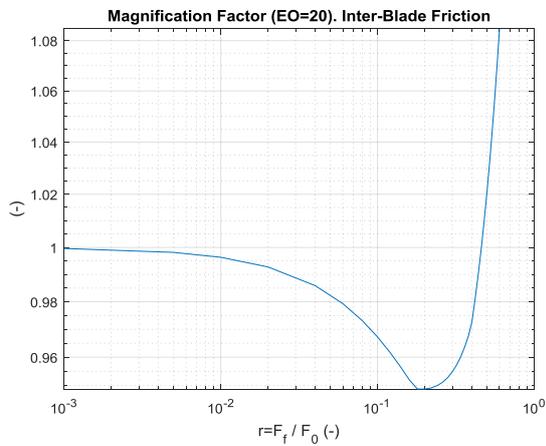


Figure 4.21b. Response without friction damper (EO=20)



4.21c. Magnification Factor against  $r$  (EO=20)

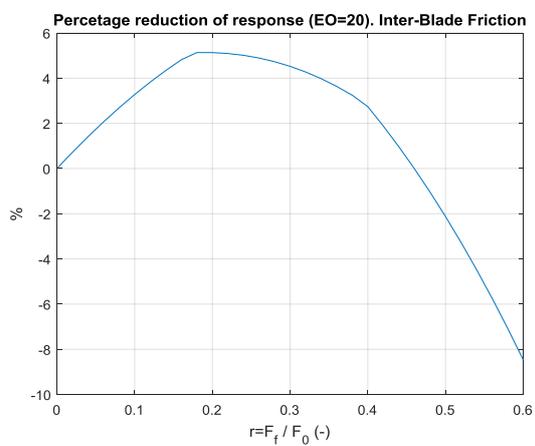


Figure 4.21d. % amplitude reduction against  $r$  (EO=20)

EO = 30 :

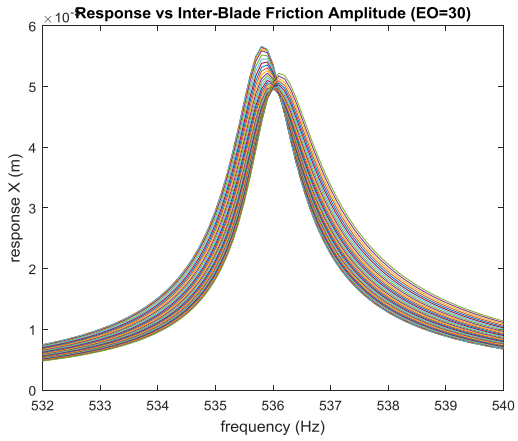


Figure 4.22a. Response for different  $r$  (EO=30)

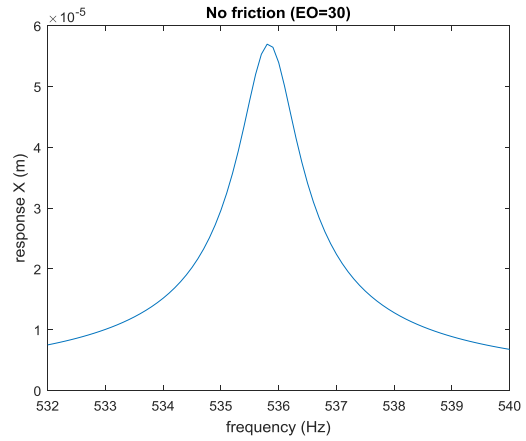
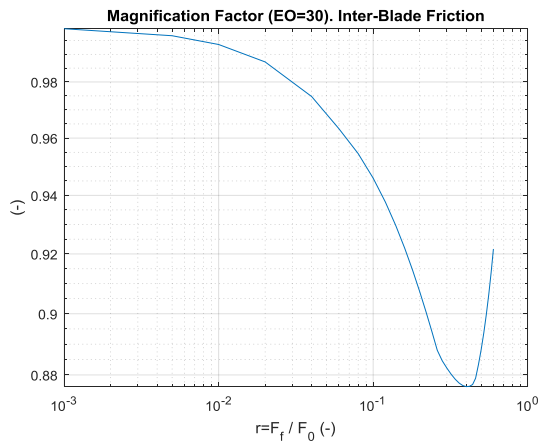


Figure 4.22b. Response without friction damper (EO=30)



4.22c. Magnification Factor against  $r$  (EO=30)

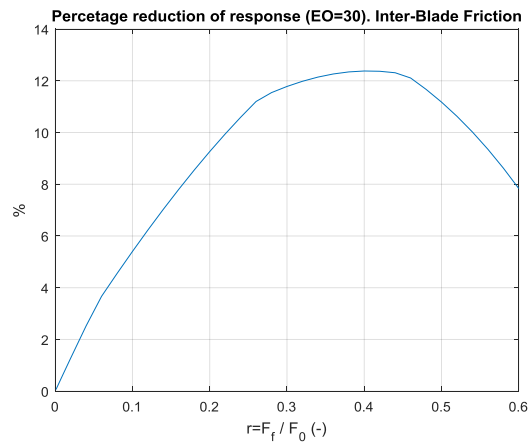


Figure 4.22d. % amplitude reduction against  $r$  (EO=30)

EO = 40 :

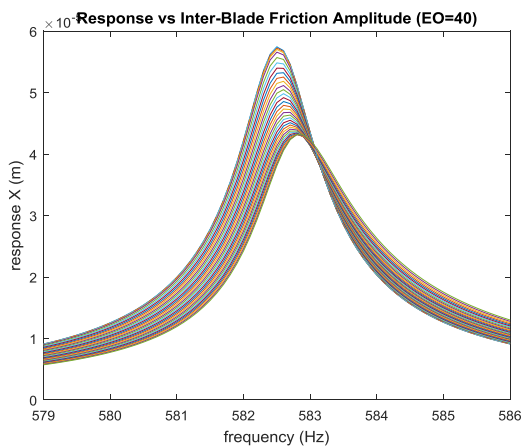


Figure 4.23a. Response for different  $r$  (EO=40)

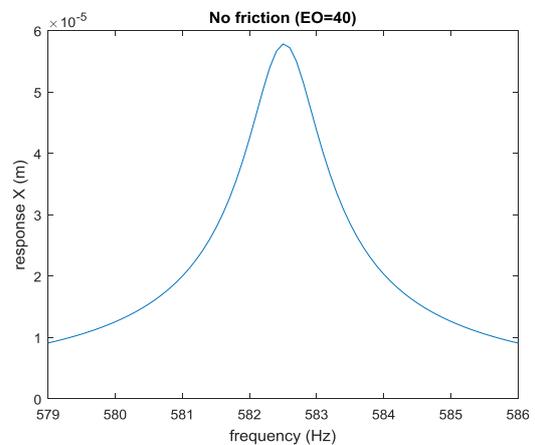
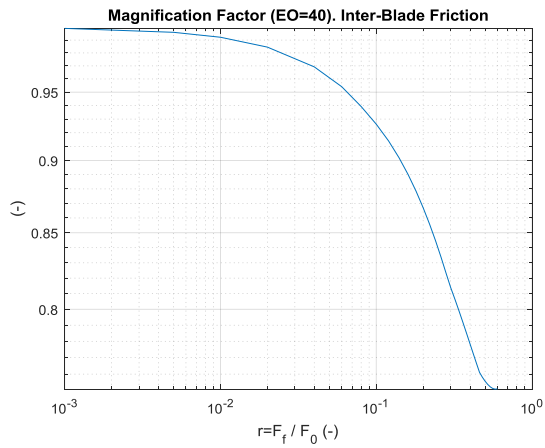


Figure 4.23b. Response without friction damper (EO=40)



4.23c. Magnification Factor against  $r$  (EO=40)

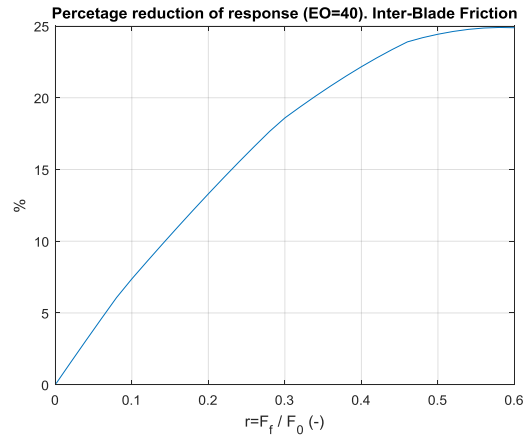


Figure 4.23d. % amplitude reduction against  $r$  (EO=40)

EO = 50 :

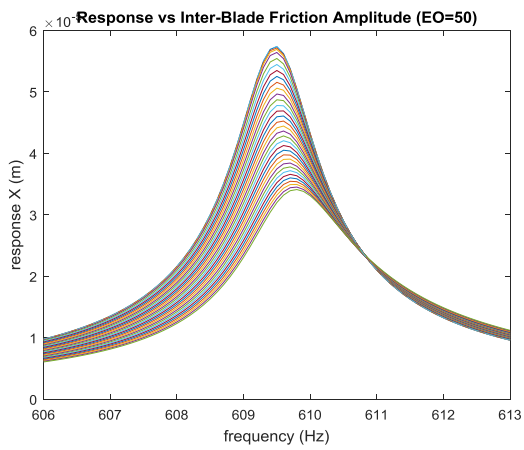


Figure 4.24a. Response for different  $r$  (EO=50)

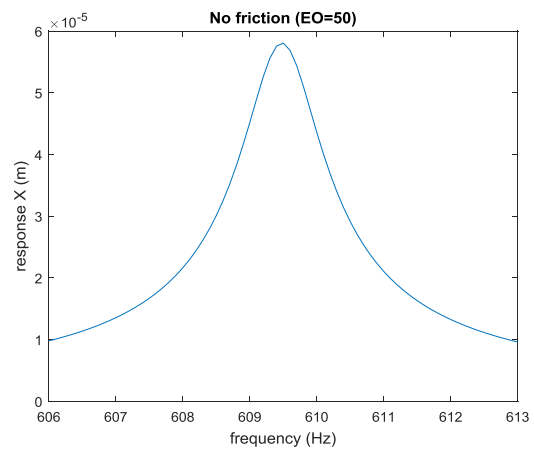
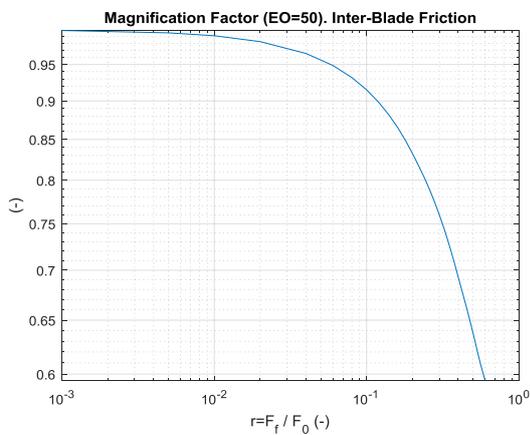


Figure 4.24b. Response without friction damper (EO=50)



4.24c. Magnification Factor against  $r$  (EO=50)

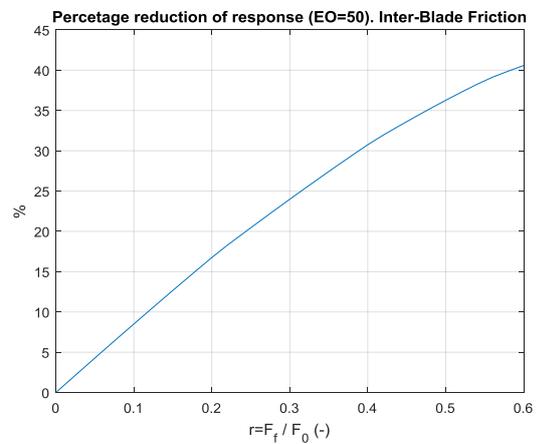


Figure 4.24d. % amplitude reduction against  $r$  (EO=50)

EO = 70 :

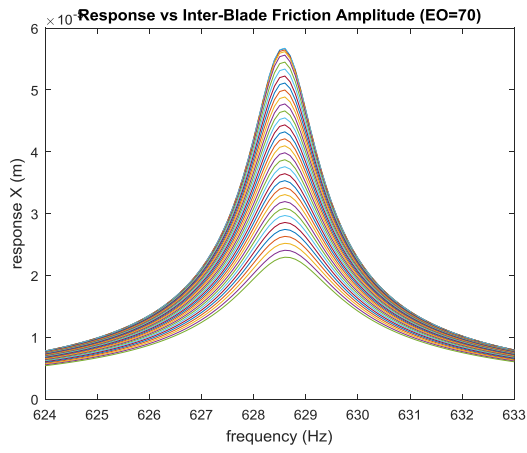


Figure 4.25a. Response for different  $r$  (EO=70)

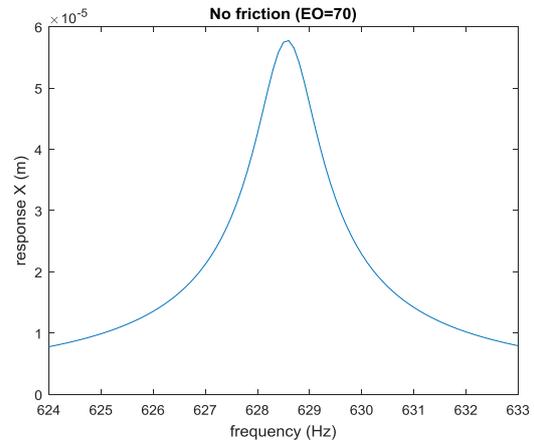
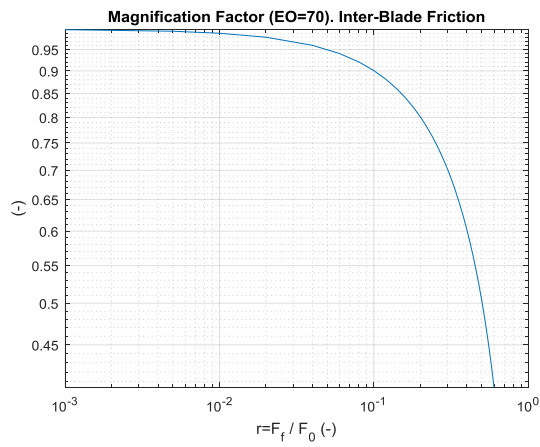


Figure 4.25b. Response without friction damper (EO=70)



4.25c. Magnification Factor against  $r$  (EO=70)

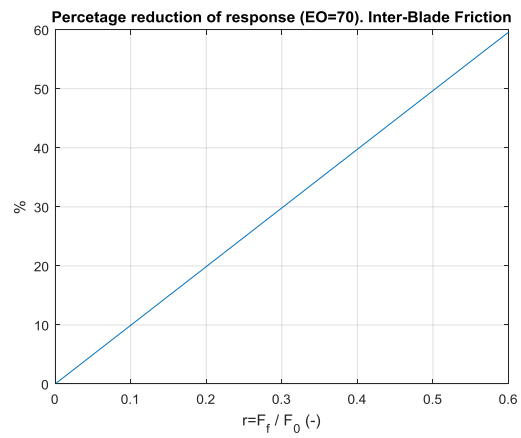


Figure 4.25d. % amplitude reduction against  $r$  (EO=70)

## Conclusions

The thesis allows to understand how mistuning affects the vibration of a bladed disk. The aim of the thesis was to find a method of study to acquire information about the mechanical characteristics of a bladed disk which is affected by mistuning. It was demonstrated that, through a dedicated testing on the structure, it is possible to investigate the mechanical properties of the system by means of the FRF Decoupling Method, which allows to get the equivalent stiffness and damping properties of the joints, connecting the blades to the disk, which represent a source of mistuning because of the uncertainties linked to the coupling. This reverse engineering approach allows the designer to avoid the modeling, then the dynamic study of such complicated parts represented by the joints. Fortunately, the joints represent a region where friction can occur. It is well known that friction can damp the response of the blades by reducing considerably the resonance amplitude and it is a benefit for the fatigue life of the components. For this reason, the last chapter of the thesis was dedicated to the study of the friction-damped response, trying to evaluate the damping effect of friction by means of equivalent friction dampers incorporated in the model. It was shown that the damping effect depends strongly on the preload conditions but also on the EO if a sliding friction is generated between moving parts of the system.

# Appendix

## 1 Modeling of the bladed disk

The structure was studied by using a lumped parameters method. The model is constituted by two mass elements  $m_d$  and  $m_b$ , respectively the mass of the disk sector and the mass of the blade, and three stiffness elements  $k_d$ ,  $k_c$  and  $k_b$  respectively the disk stiffness connecting two adjacent degrees of freedom, the disk stiffness connecting the degrees of freedom to the ground, and the stiffness associated to the blade. By referring to the graphical representation of the model in a circular configuration showed by the figure 3.1, in chapter 1, it is possible to see this system represented in a equivalent linear ( figure A-1.1 ) form so to be able to study the free body diagram for each degree of freedom and to write the equations of motion.

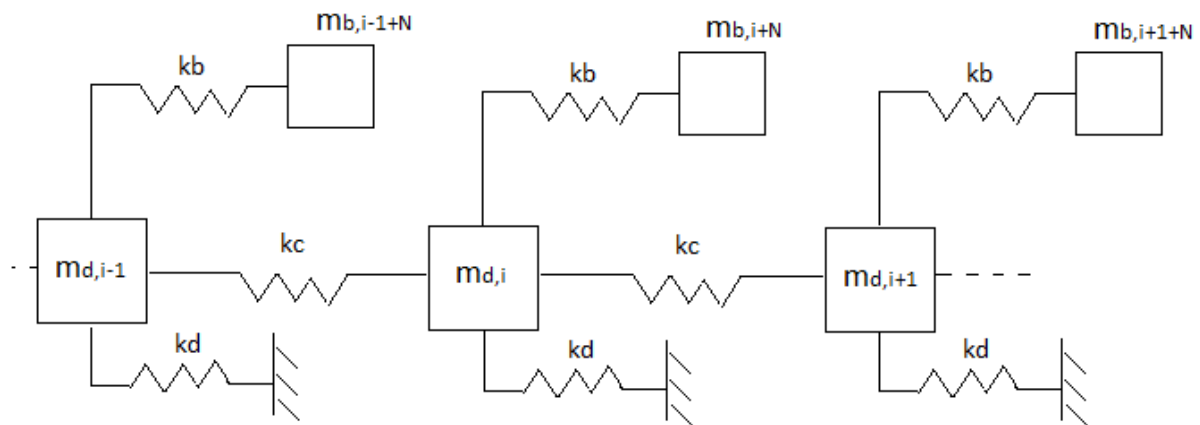


Figure A-1.1 Lumped parameters model

With such a configuration the subscript  $i$  is meant to assume values from 1 to  $N$ . The free body diagram of the  $i$ -th disk mass  $m_{d,i}$  is showed in figure A-1.2 and produces the first  $N$  equations of motion (A-1.1).

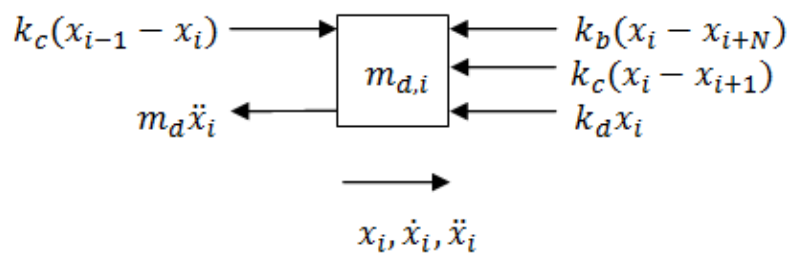


Figure A-1.2. Free body diagram of the  $m_{d,i}$ .

$$m_d \ddot{x}_i - k_c x_{i-1} + (k_d + 2k_c + k_b)x_i - k_c x_{i+1} - k_b x_{i+N} = 0; \text{ if } i \in [2, N-1] \quad (\text{A-1.1a})$$

$$m_d \ddot{x}_1 - k_c x_N + (k_d + 2k_c + k_b)x_1 - k_c x_2 - k_b x_{1+N} = 0; \text{ if } i = 1 \quad (\text{A-1.1b})$$

$$m_d \ddot{x}_N - k_c x_{N-1} + (k_d + 2k_c + k_b)x_N - k_c x_1 - k_b x_{2N} = 0; \text{ if } i = N \quad (\text{A-1.1c})$$

The other  $N$  equations of motion (A-1.2) refer to the degrees of freedom of the blades, whose free body diagram is reported in figure A-1.3. Now the subscript  $i$  is meant to range from  $N+1$  to  $2N$ .

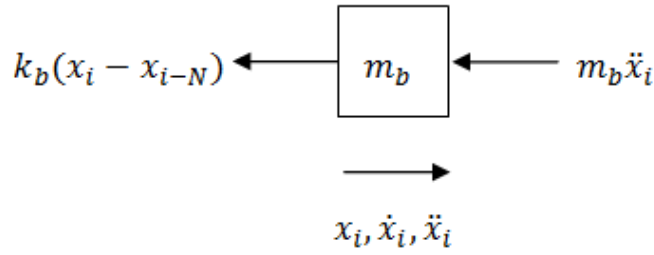


Figure A-1.3. Free body diagram of  $m_{b,i}$ .

$$m_b \ddot{x}_i - k_b x_{i-N} + k_b x_i = 0 \quad (\text{A-1.2})$$

The mass matrix  $[M]$  and the stiffness matrix  $[K]$  are derived from the equilibrium equations of each degree of freedom and they have dimension  $2N \times 2N$ :

$$[M] = \text{diag}(m_{d_1}, \dots, m_{d_N}, m_{b_1}, \dots, m_{b_N})$$

$$[K] = \begin{bmatrix} k_s & -k_c & 0 & \dots & 0 & -k_c & -k_b & \dots & 0 \\ -k_c & \ddots & \ddots & \ddots & \vdots & \ddots & \ddots & \ddots & 0 \\ 0 & \ddots & \ddots & \ddots & 0 & \dots & 0 & -k_c & -k_b \\ \vdots & & & kb & 0 & & & 0 & \\ & & & 0 & \ddots & & & \ddots & 0 \\ \text{sym} & & & \dots & & & & 0 & k_b \end{bmatrix}$$

with  $k_s = k_d + 2k_c + k_b$ .

## 2 Modeling of a disk sector

The analysis of the system by exploiting the cyclic symmetry property is conducted on a single sector of the bladed disk. The sector can be modeled with three degrees of freedom. The masses involved are  $m_{d,L}$ ,  $m_{d,R}$  which correspond both to the half of the mass  $m_d$ , used in the full system study, and the mass of the blade  $m_b$ . The stiffness elements  $k_d$ ,  $k_c$  and  $k_b$  are the same of those used in the full system study. The lumped parameters model of the sector is the one showed in figure A-2.1. Then, it is possible to derive the mass matrix and the stiffness matrix associated to the system, with the same procedure used for the full system study ( the free body diagrams for each degree of freedom are showed in figures A-2.2).

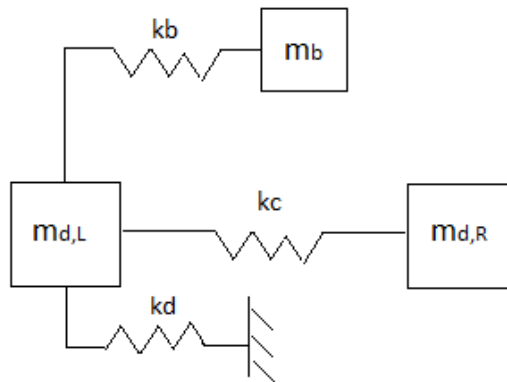


Figure A-2.1. Lumped parameters model of the sector.

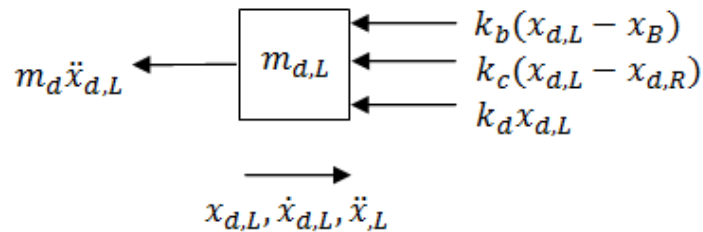


Figure A-2.2a. Free body diagram of the left hand side dof.

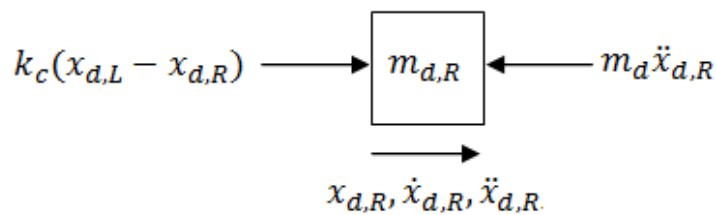


Figure A-2.2b. Free body diagram of the right hand side dof.

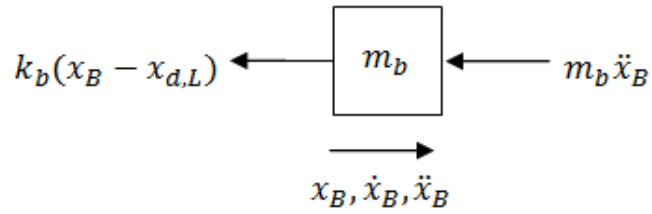


Figure A-2.2c. Free body diagram of the blade dof.

Being the displacement coordinates vector  $\{x_{d,L}, x_B, x_{d,R}\}^T$ , the mass matrix  $[M_s]$  and the stiffness matrix  $[K_s]$  are easily derived:

$$[M_s] = \begin{bmatrix} \frac{m_d}{2} & 0 & 0 \\ 0 & m_b & 0 \\ 0 & 0 & \frac{m_d}{2} \end{bmatrix}$$

$$[K_s] = \begin{bmatrix} k_d + k_c + k_b & -k_b & -k_c \\ -k_b & k_b & 0 \\ -k_c & 0 & k_c \end{bmatrix}$$

### 3 Modeling of a sector for blade-to-blade friction analysis

The study of the forced response of the system with the introduction of sliding friction between the shrouds of the blade, by exploiting the cyclic symmetry property, requires the definition of a new model of the sector. It has to include at least two blades in order to consider the friction force which is generated between them, during the motion. A possible choice, which includes the minimum number of degrees of freedom, is the one represented in figure A-3.1 (in the figure, the sector is constituted by all the mass and stiffness elements included within the thick dashed line). In order to satisfy the cyclic symmetry property, the sector is constituted by two halves of two adjacent blades and the portion of disk which is delimited between them. Since the sector is defined in such a way, the mass and stiffness elements, which constitute the lumped parameters model of the sector, correspond exactly to the half of the mass and stiffness elements defined for the *full-system* model, with the exception of the stiffness element which connects the two adjacent disk masses because it is entirely included within the sector.

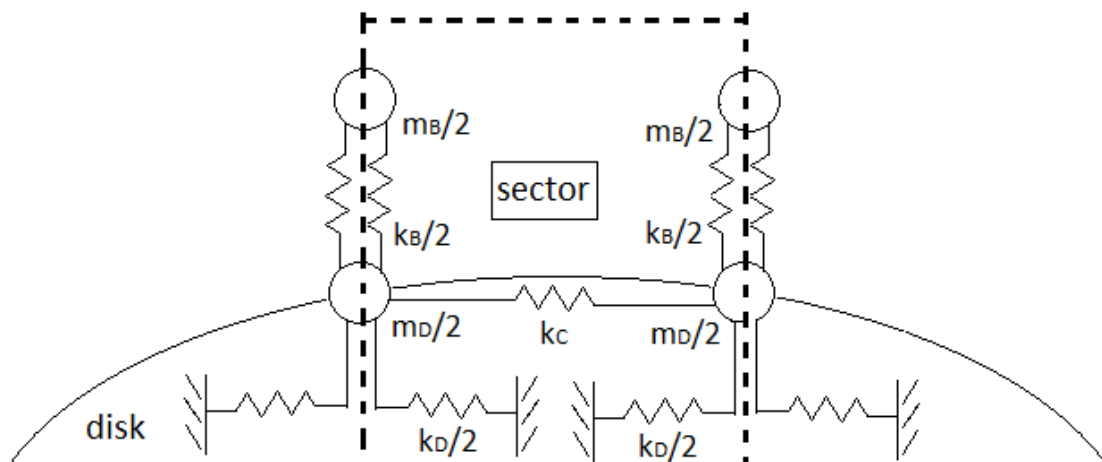


Figure A-3.1. Sector model for blade-to-blade friction analysis

If the mass and stiffness elements defined for the *full-system* study are  $m_D$ ,  $m_B$ ,  $k_D$ ,  $k_C$  and  $k_B$  (identified by a subscript with capital letter) the mass and stiffness elements of the new sector are  $m_d$ ,  $m_b$ ,  $k_d$ ,  $k_c$  and  $k_b$  (identified by a subscript with small letter) and they are defined as follows:

$$m_d = \frac{m_D}{2} ; m_b = \frac{m_B}{2} ; k_d = \frac{k_D}{2} ; k_c = k_C ; k_b = \frac{k_B}{2} .$$

It is now possible to study the free body diagrams of the masses of the sector and to write the equations of motion (A-3.1), in order to find the mass and stiffness matrices which describes the model. From figure A-3.2 the free body diagrams are derived ( figures A-3.3).

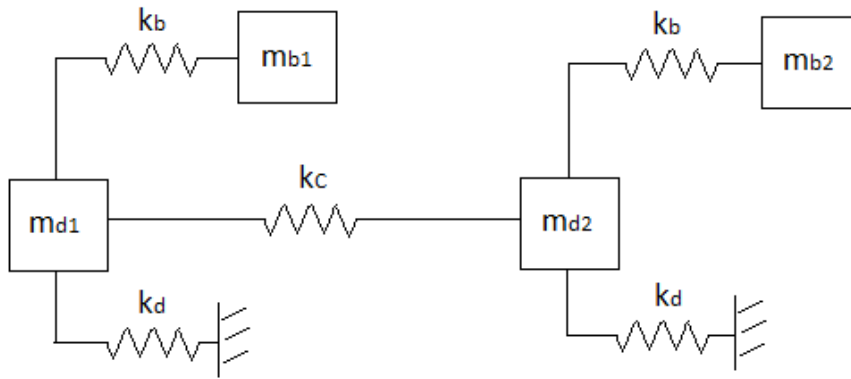


Figure A-3.2. Schematic representation of the sector model.

Free body diagram of  $m_{d1}$  :

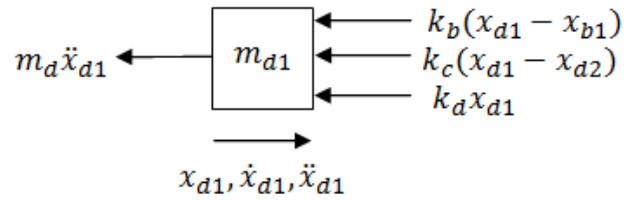


Figure A-3.3a. Free body diagram of mass  $m_{d1}$ .

$$m_d \ddot{x}_{d1} + (k_d + k_c + k_b) x_{d1} - k_c x_{d2} - k_b x_{b1} = 0 \quad (\text{A-3.1a})$$

Free body diagram of  $m_{d2}$  :

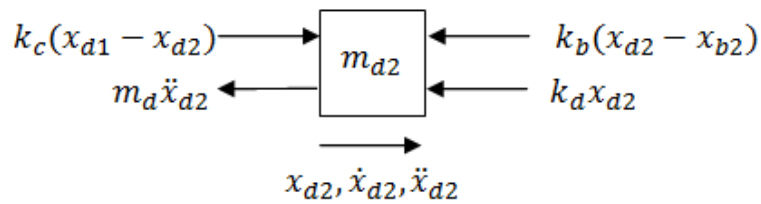


Figure A-3.3b. Free body diagram of mass  $m_{d2}$ .

$$m_d \ddot{x}_{d2} - k_c x_{d1} + (k_d + k_c + k_b) x_{d2} - k_b x_{b2} = 0 \quad (\text{A-3.1b})$$

Free body diagram of  $m_{b1}$  :

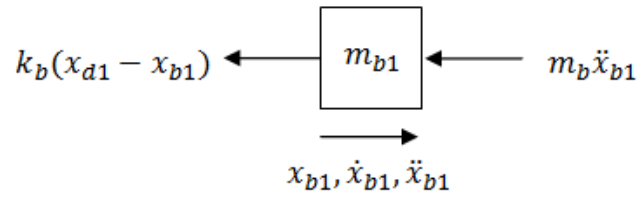


Figure A-3.3c. Free body diagram of mass  $m_{b1}$ .

$$m_b \ddot{x}_{b1} - k_b x_{d1} + k_b x_{b1} = 0 \quad (\text{A-3.1c})$$

Free body diagram of  $m_{b2}$  :

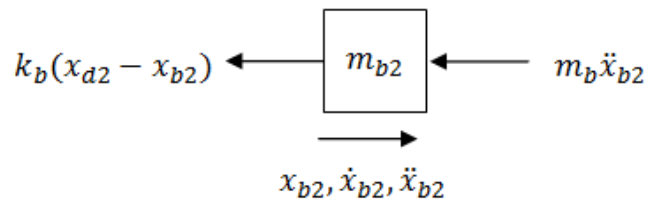


Figure A-3.3d. Free body diagram of mass  $m_{b2}$ .

$$m_b \ddot{x}_{b2} - k_b x_{d2} + k_b x_{b2} = 0 \quad (\text{A-3.1d})$$

The mass and stiffness matrices are directly defined from the free body diagrams (A-3.3), once a vector of coordinates  $\{x\}$  has been set (A-3.2).

$$\{x\} = \{x_{d1}, x_{d2}, x_{b1}, x_{b2}\}^T \quad (\text{A-3.2})$$

$$M_s = \begin{bmatrix} m_d & 0 & 0 & 0 \\ 0 & m_d & 0 & 0 \\ 0 & 0 & m_b & 0 \\ 0 & 0 & 0 & m_b \end{bmatrix} \quad (\text{A-3.3a})$$

$$K_s = \begin{bmatrix} k_d + k_c + k_b & -k_c & -k_b & 0 \\ -k_c & k_d + k_c + k_b & 0 & -k_b \\ -k_b & 0 & k_b & 0 \\ 0 & -k_b & 0 & k_b \end{bmatrix} \quad (\text{A-3.3b})$$

The damping matrix  $[C_s]$  can be obtained by means of the modal matrix, once a modal damping ratio has been associated to each mode shape. Once all the matrices have been built, the equation of motion of the system can be written in the classical matrix form (A-3.4).

$$M_s \ddot{x} + C_s \dot{x} + K_s x = 0 \quad (\text{A-3.4})$$

The cyclic symmetry property is introduced in the model through a proper transformation matrix, as in the case of the linear system study. Here, two nodes of the model belong to the left boundary of the sector. The other two nodes belong to the right boundary of the sector. So, a relation can be established between the coordinates of the left hand side of the sector and those of the right hand side. The transformation matrix allows to reduce the degrees of freedom of the model from four to two,  $\{x'\}$  (A-3.6). In particular the coordinates  $x_{d2}$  and  $x_{b2}$  can be written as functions of the coordinates  $x_{d1}$  and  $x_{b1}$  respectively (A-3.5), by means of the inter-blade phase angle which brings the information of the EO.

$$x_{d2} = e^{i\mu} x_{d1} \quad (\text{A-3.5a})$$

$$x_{b2} = e^{i\mu} x_{b1} \quad (\text{A-3.5b})$$

$$\{x\} = [T]\{x'\} = \begin{bmatrix} 1 & 0 \\ e^{i\mu} & 0 \\ 0 & 1 \\ 0 & e^{i\mu} \end{bmatrix} \begin{Bmatrix} x_{d1} \\ x_{b1} \end{Bmatrix} \quad (\text{A-3.6})$$

By substituting (A-3.6) into the equation of motion (A-3.4) and pre-multiplying both left and right hand side of the equation by the transpose of the transformation matrix, the new equation of motion of the reduced system can be written as follows (A-3.7). Now, the matrices  $M'_s(\mu)$ ,  $C'_s(\mu)$  and  $K'_s(\mu)$  depends on the EO.

$$M'_s(\mu) \ddot{x}' + C'_s(\mu) \dot{x}' + K'_s(\mu) x' = 0 \quad (\text{A-3.7})$$

## 4 Modeling of the bladed disk with joints incorporation

The lumped parameters model of the bladed disk used in the paragraph 3.4 is constituted by  $3N$  degrees of freedom  $\{x\}$  (A-4.1). They are ordered in the coordinates vector so to have the first  $N$  dofs connected to the disk, the second  $N$  dofs connected to the interfaces of the blades with the joints and the third  $N$  dofs describing the motion of the blades where the excitation force is applied. By looking at figure A-4.1 it is possible to derive the free body diagrams of the masses of the system, then to build the mass, stiffness and damping matrices.

$$\{x\} = \left\{ \{x_{disk}\}_{N \times 1}, \{x_{blade\ root}\}_{N \times 1}, \{x_{blade\ tip}\}_{N \times 1} \right\}^T \quad (A-4.1)$$

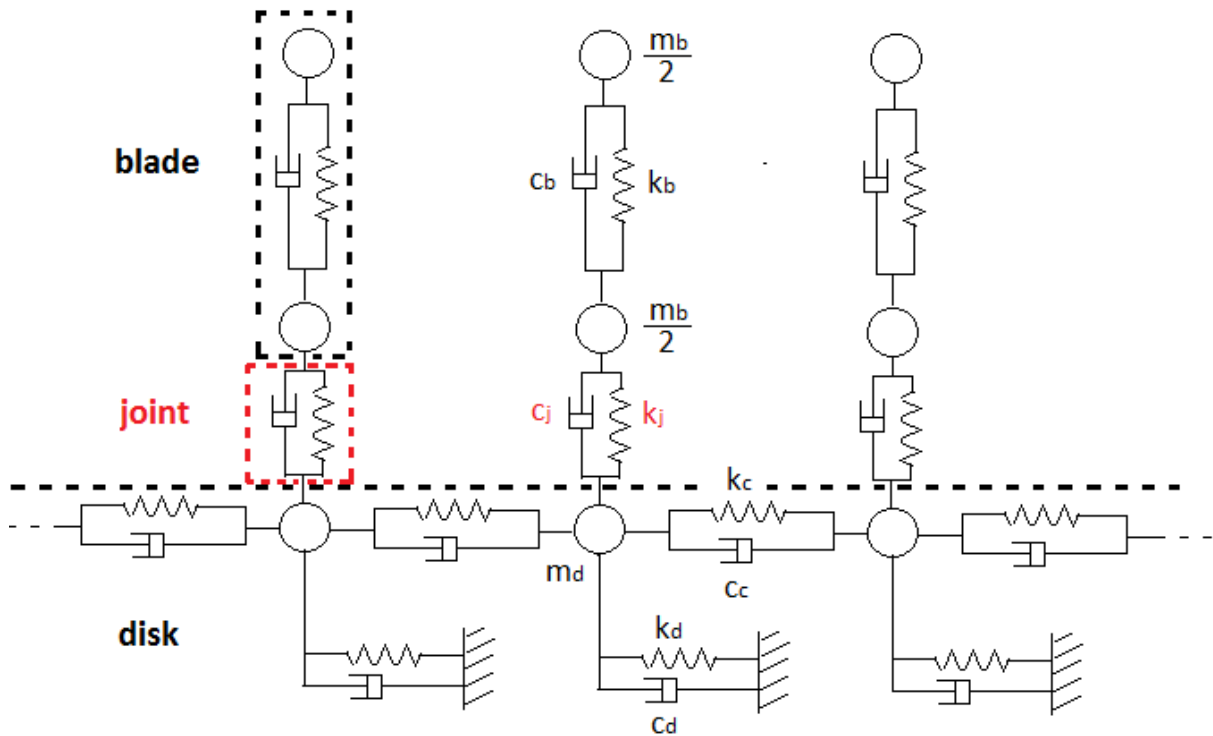


Figure A-4.1. Model of the bladed disk with joints incorporation.

Free body diagram of  $m_{d,i}$ ,  $i = 1, \dots, N$ :

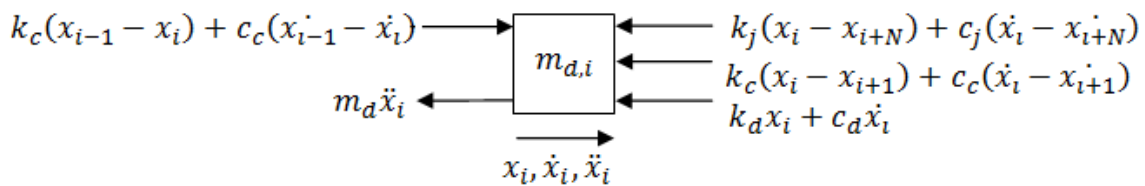


Figure A-4.2a. Free body diagram of  $m_{d,i}$ .

Free body diagram of  $\frac{m_{b,i}}{2}$  (blade root),  $i = N+1, \dots, 2N$  :

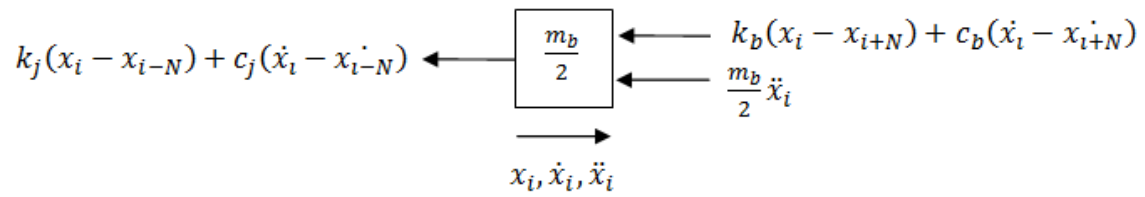


Figure A-4.2b. Free body diagram of  $\frac{m_{b,i}}{2}$  at the roots of the blades.

Free body diagram of  $\frac{m_{b,i}}{2}$  (blade tip),  $i = 2N+1, \dots, 3N$  :

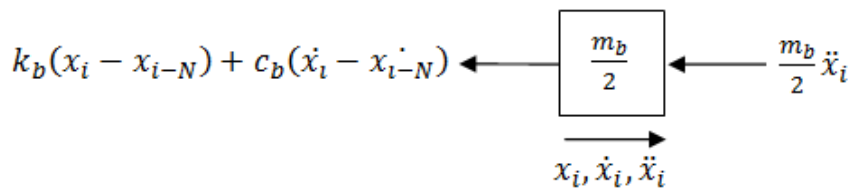


Figure A-4.2c. Free body diagram of  $\frac{m_{b,i}}{2}$  at the tips of the blades.

## References

- [1] Tobias, S.A. and Arnold, R.N., 1957, "The Influence of Dynamical Imperfections on the Vibration of Rotating Disks", Proceedings of the Institution of Mechanical Engineers.
- [2] Whitehead, D.S., 1966, "Effect of Mistuning on the Vibration of Turbomachine Blades Induced by Wakes", Journal of Mechanical Engineering Science.
- [3] Ewins, D.J., 1969, "The Effect of Detuning Upon the Forced Vibration of Bladed Disks", Journal of Sound and Vibration.
- 50
- [4] Crawley, E.F. and Hall, K.C., 1983, "Optimization and Mechanism of Mistuning in Cascades", ASME Journal of Engineering for Gas Turbines and Power.
- [5] Kielb, R.E. and Kaza, K.R.V., 1984, "Effects of Structural Coupling on Mistuned Cascade Flutter and Response", ASME Journal of Engineering for Gas Turbines and Power.
- [6] Imregun, M. and Ewins, D.J., 1984, "Aeroelastic Vibration Analysis of Tuned and Mistuned Bladed Systems", Proceedings of the 2nd Symposium on Unsteady Aerodynamics of Turbomachines and Propellers, Cambridge, UK.
- [7] Petrov, E.P., Sanliturk, K.Y. and Ewins, D.J., 2002, "A New Method for Dynamic Analysis of Mistuned Bladed Disks Based on the Exact Relationship Between Tuned and Mistuned Systems", ASME Journal of Engineering for Gas Turbines and Power.
- [8] Yang, M.-T. and Griffin, J.H., 2001, "A Reduced Order Model of Mistuning Using a Subset of Nominal System Modes", ASME, Journal of Engineering for Gas Turbines and Power.
- [9] Feiner, D.M. and Griffin, J.H., 2002, "A Fundamental Model of Mistuning for a Single Family of Modes", Proceedings of the ASME TURBO EXPO 2002, 2002-GT-30425
- [10] Griffin, J.H., 1990, "A Review of Friction Damping of Turbine Blade Vibration", International Journal of Turbo and Jet Engines.
- [11] Wang, W., 1992, "Dynamic Analysis of Flexible Bladed Disk-Shaft Rotor Systems", PhD Thesis, Carleton University Ottawa
- [12] Petrov, E.P., and Ewins, D.J., 2006, "Advanced Modelling of Underplatform Friction Dampers for Analysis of Bladed Disc Vibration", Proceedings of the ASME TURBO EXPO 2006, GT2006- 90146
- [13] J.X. Yuan, X.M. Wu, Identification of the joint structural parameters of machine tool by DDS and FEM, Trans. Am. Soc. Mech. Eng. 107 (1985).
- [14] T.R. Kim, S.M. Wu, K.F. Eman, Identification of joint parameters for a taper joint, Trans. Am. Soc. Mech. Eng. 111 (1989).
- [15] J. Wang, P. Sas, A method for identifying parameters of mechanical joints, J. Appl. Mech. 57 (1990).
- [16] A.S. Nobari, Identification of the Dynamic Characteristics of Structural Joints (Ph.D. thesis), Department of Mechanical Engineering, Imperial College of Science, Technology and Medicine, University of London, 1991.
- [17] Y. Ren, C.F. Beards, Identification of effective linear joints using coupling and joint identification techniques, J. Vib. Acoust. 120 (1998).